Toward Far Infrared Quantum Well Lasers

by

Ilya Lyubomirsky

Submitted to the Department of Electrical Engineering and Computer Science
in partial fulfillment of the requirements for the degree of

Doctor of Philosophy

at the

MASSACHUSETTS INSTITUTE OF TECHNOLOGY

February 1999

Author .....
Department of Electrical Engineering and Computer Science
November 19, 1998

Certified by .....
Qing Hu
Associate Professor of Electrical Engineering and Computer Science
Thesis Supervisor

Accepted by .....
Arthur C. Smith
Chairman, Departmental Committee on Graduate Students

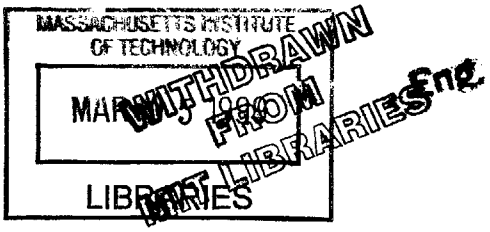

Toward Far Infrared Quantum Well Lasers

by

Ilya Lyubomirsky

Submitted to the Department of Electrical Engineering and Computer Science
on November 19, 1998, in partial fulfillment of the
requirements for the degree of
Doctor of Philosophy

Abstract

The far infrared frequency range $30 - 300\,\mu m$ remains one of the least developed spectral regions of light. A cheap and efficient far infrared semiconductor laser would enable new technologies in spectroscopy, pollution monitoring and chemical agent detection. Unfortunately, the frequency range of conventional semiconductor diode lasers is limited by the band gap. This limitation of natural semiconductor crystals can be overcome by using artificially grown quantum well structures. Quantum wells behave like giant atoms whose energy levels and wavefunctions can be designed by band gap engineering.

This thesis investigates the possibility of using optically excited intersubband transitions in quantum wells to realize a far infrared laser. A major difficulty of scaling the wavelength of quantum well lasers to the far infrared is the extremely unfavorable scaling of emission efficiency $\propto \lambda^{-4}$. The far infrared emission efficiency is so weak that previous emission experiments were dominated by black body radiation. In response to this challenge, we proposed and analyzed a novel four energy level scheme in a triple coupled quantum well design. The four level design improved the gain and emission efficiency by an order of magnitude over previous three level designs. This innovation paved the way for a successful experiment to measure far infrared intersubband emission.

An optics laboratory was built to perform absorption and emission spectroscopy on optically pumped far infrared quantum well lasers. Two multiple quantum well samples were grown using the AlGaAs-GaAs material system to test and compare the conventional three level design and the new four level design. Absorption spectroscopy measurements confirmed the designed energy levels and dipole moments for both samples. Spontaneous emission measurements showed an order of magnitude improvement in emission power of the four level design compared to the three level design. The emission spectra were resolved using a Nicolet Fourier transform infrared spectrometer. The intersubband emission peak of the three level design was very weak and the spectrum was dominated by black body radiation. A clear improvement was seen in the emission spectrum of the four level design. The experiments on the four level design demonstrated the first conclusive measurement of optically pumped far

infrared intersubband emission from quantum wells.

The emission experiments revealed an important problem in optically pumped far infrared quantum wells lasers. The emission power of both samples was an order of magnitude weaker than predicted by theory. This discrepancy was identified as being due to heating effects. Heating of the electron gas can result in the opening of a parasitic LO phonon scattering channel for electrons in the upper laser level. A new five level design scheme using quadruple coupled quantum wells was proposed and analyzed to improve high temperature performance by enhancing the scattering rate from the lower laser level. The five level scheme should extend the operating temperature range of far infrared quantum well lasers beyond 100 K.

Thesis Supervisor: Qing Hu
Title: Associate Professor of Electrical Engineering and Computer Science

Acknowledgments

First of all, I would like to thank my advisor, Prof. Qing Hu, for giving his steadfast dedication, guidance and support to a very challenging Ph.D. thesis project. Qing's determination to overcome any obstacle, no matter how difficult, is a source of inspiration to every student in our group.

This research has benefited from many useful discussions with current and former group members including, Dr. Bin Xu, Ben Williams, Dr. Gert de Lange, Dr. Simon Verghese, Farhan Rana, Brian Riely, Yanko Shereitov, Noah Zamdmer, Erik Duerr, Arif Rahman and Konstantinos Konistis. Dr. Bin Xu deserves special thanks for helping to develop the far infrared emission measurement setup that we both shared. Ben Williams was kind enough to proofread a rough draft of this thesis. The quantum well samples were grown by Prof. Michael R. Melloch at Purdue University, and by Prof. Ben Streetman and Chad Hansing at the University of Texas. The experimental part of this thesis would have been impossible without their collaboration.

I owe a special thanks to the Fannie and John Hertz Foundation for five years of support. Dr. Lowell L. Wood of Lawrence Livermore National Laboratory gave me inspiration and encouragement at the beginning of my graduate studies. Prof. Eric P. Ippen served on my Oral Exam Committee, Area Exam Committee and as reader for this thesis. I thank him for this and for his advice and encouragement throughout my tenure at MIT. I would also like to thank Prof. Clifton G. Fonstad for serving as the second thesis reader.

Finally, I must thank my family for constant emotional support during many difficult times. My wife Shirly has been a blessing. I thank her for believing in me and for giving me our beautiful daughter Maya. This thesis is dedicated to my family.

Contents

1 Introduction **17**

1.1 Why Far Infrared? 17

1.2 Intersubband Transitions in Quantum Wells 19

1.3 Mid Infrared Quantum Well Lasers 22

1.4 Toward Far Infrared Quantum Well Lasers 25

2 Intersubband Transitions in Quantum Wells **29**

2.1 Electron States in Quantum Wells 29

2.2 Radiative Intersubband Transitions 33

2.2.1 Stimulated Emission and Gain 35

2.2.2 Spontaneous Emission 37

2.3 Phonon Intersubband Scattering 38

2.4 Rate Equation Analysis 43

2.4.1 Three Level System 43

2.4.2 Four Level System 45

2.4.3 Five Level System 49

3 Quantum Well Laser Design **51**

3.1 Introduction 51

3.2 Three Level Scheme 52

3.3 Four Level Scheme 54

3.4 Gain and Loss 59
3.5 Concluding Remarks 63

4 High Temperature Laser Design **65**
4.1 Introduction 65
4.2 Phonon Scattering at High Temperatures 67
4.3 Scaling the Emission Frequency 70
4.4 Five Level Design for Enhancing $\frac{1}{\tau_{12}}$ 73
4.5 Concluding Remarks 74

5 Spontaneous Emission Experiments **79**
5.1 Introduction 79
5.2 Absorbance Experiment Setup 80
5.3 Emission Experiment Setup 83
5.4 Three Level Design 87
5.5 Four Level Design 91
5.6 Concluding Remarks 95

6 Conclusions and Future Work **99**
6.1 Conclusions 99
6.2 Future Work 101
6.2.1 Fabrication 101
6.2.2 Pumping Schemes 101
6.2.3 Material Systems 104

A Far Infrared Nonlinear Optics in Quantum Wells **107**

List of Figures

1-1 Quantum well in real space and reciprocal lattice space. The potential well caused by the $Al_xGa_{1-x}As - GaAs - Al_xGa_{1-x}As$ heterostructure in the growth direction gives rise to bound states localized in the quantum well. These bound states are represented as subbands in k space since the electrons are still free to move in the plane of the quantum well. 20

1-2 Quantum well schematic of an electrically pumped mid infrared intersubband laser. A voltage bias aligns the bands for electric pumping of the upper laser level E_3. Population inversion is assured by designing a faster phonon scattering rate emptying the lower laser level E_2 than from the upper laser level. 23

1-3 Quantum well schematic of an optically pumped mid infrared intersubband laser. Electrons are optically pumped from the ground state E_1 to the upper laser level E_3. Population inversion is assured by designing for a faster phonon scattering rate emptying the lower laser level E_2 than from the upper laser level. 24

2-1 The calculated energy levels and wavefunctions for Sirtori's asymmetric double quantum well structure. 32

2-2 The emission process of a photon (or phonon) in electronic intersubband transitions between subbands E_i and E_f. 34

2-3 For a photon with $\hbar\omega \sim E_i - E_f$, the ensemble of electrons in subband E_i looks like a collection of two level atoms with cross section σ_{if}. . . 35

2-4 The geometrical relationship in reciprocal lattice space required for conservation of momentum. The total phonon scattering rate from state (E_i, k_i) is obtained by summing the scattering rate to all final electron states (E_f, k_f). This involves an integration over θ. 41

2-5 The three level system. Electrons are pumped from the ground state E_1 to E_3. Population inversion is created between subbands E_3 and E_2 by engineering a faster phonon scattering rate $\frac{1}{\tau_{12}}$ than $\frac{1}{\tau_{23}}$. The phonon scattering rate $\frac{1}{\tau_{13}}$ also plays an important role in determining the magnitude of gain and emission efficiency. 43

2-6 The four level system. Electrons are pumped from the ground state E_1 to E_4, followed by a fast relaxation to subband E_3. Population inversion is created between subbands E_3 and E_2 by engineering a faster phonon scattering rate $\frac{1}{\tau_{12}}$ than $\frac{1}{\tau_{23}}$ and $\frac{1}{\tau_{24}}$. The phonon scattering rate $\frac{1}{\tau_{13}}$ also plays an important role in determining the magnitude of gain and emission efficiency. 46

2-7 The five level system. Electrons are pumped from the ground state E_1 to E_5, followed by a fast relaxation to subband E_4 and E_3. Population inversion is created between subbands E_3 and E_2 by engineering a faster phonon scattering rate $\frac{1}{\tau_{12}}$ than $\frac{1}{\tau_{23}}$, $\frac{1}{\tau_{24}}$ and $\frac{1}{\tau_{25}}$. The phonon scattering rate $\frac{1}{\tau_{13}}$ also plays an important role in determining the magnitude of gain and emission efficiency. 48

3-1 Double coupled quantum well structure for the three level design with a sheet electron density of $3 \times 10^{11}\, cm^{-2}$. The calculated transition energies are $\Delta E_{13} = 120.3\, meV$, $\Delta E_{12} = 95.5\, meV$ and $\Delta E_{23} = 24.8\, meV$. The calculated dipole matrix elements are $Z_{12} = 20.4\,\text{Å}$, $Z_{23} = 45.9\,\text{Å}$ and $Z_{13} = 9.6\,\text{Å}$. 53

3-2 Triple coupled quantum well structure for the four level design with a sheet electron density of $3 \times 10^{11}\,cm^{-2}$. The calculated transition energies are $\Delta E_{14} = 119.8\,meV$, $\Delta E_{13} = 83.8\,meV$, $\Delta E_{12} = 58.2\,meV$ and $\Delta E_{23} = 25.6\,meV$. The calculated dipole matrix elements are $Z_{12} = 9.5\,\text{Å}$, $Z_{23} = 34.4\,\text{Å}$, $Z_{13} = 6.6\,\text{Å}$, $Z_{14} = 18.9\,\text{Å}$, $Z_{34} = 22.9\,\text{Å}$ and $Z_{24} = 10.6\,\text{Å}$. 55

3-3 Comparison of emission efficiency for the three level and four level designs as a function of electron density in the ground state of the quantum wells. The peak in emission efficiency of the four level design is due to the optimal alignment of $E_4 - E_3 \sim 36\,meV$ at $\rho_1 \sim 3 \times 10^{11}\,cm^{-2}$. 57

3-4 Comparison of population inversion for the three level and four level designs as a function of electron density in the ground state of the quantum wells. A pump intensity of $3.2\,kW\,cm^{-2}$ is assumed, corresponding to 1 Watt of pump power focused to a $200\,\mu m$ diameter spot. The peak in population inversion of the four level design is due to the optimal alignment of $E_4 - E_3 \sim 36\,meV$ at $\rho_1 \sim 3 \times 10^{11}\,cm^{-2}$. . . . 58

3-5 Optically pumped far infrared quantum well laser waveguide structure. The rectangular slab waveguide is covered by metal on the bottom surface and a grating on the top surface. The grating is used to couple the CO_2 pump laser to intersubband transitions in the quantum wells. 60

3-6 Comparison of gain for the three level and four level designs as a function of electron density in the ground state of the quantum wells. The gain is calculated using the population inversion of Figure 3-4. We assume a 6 meV linewidth for the $E_3 \rightarrow E_2$ transition. 62

4-1 A schematic diagram showing the phonon scattering paths and electron distributions in the four level design at high temperatures. 68

4-2 Calculation of emission efficiency for the four level design as a function of temperature and ΔE_{23}. Emission efficiency is not improved by scaling the emission frequency to lower energies. The reason lies in the unfavorable scaling of emission efficiency with frequency $\propto (\Delta E_{23})^4$. . 71

4-3 Calculation of gain for the four level design as a function of temperature and ΔE_{23}. The temperature dependence of gain is definitely improved by scaling to lower emission frequencies. The peak gain only drops as $\propto \Delta E_{23}$ in contrast to emission efficiency. 72

4-4 Quadruple coupled quantum well structure for the five level design. The electron density in the ground state is $\rho_1 = 3 \times 10^{11}\, cm^{-2}$. The calculated transition energies are $\Delta E_{15} = 130.4\, meV$, $\Delta E_{14} = 94.3\, meV$, $\Delta E_{13} = 57.0\, meV$, $\Delta E_{12} = 36.5\, meV$ and $\Delta E_{32} = 20.5\, meV$. The calculated dipole matrix elements are $Z_{12} = 15.6\,$Å, $Z_{23} = 39.2\,$Å, $Z_{13} = 5.8\,$Å, $Z_{14} = 5.9\,$Å, $Z_{34} = 37.6\,$Å, $Z_{24} = 14.0\,$Å, $Z_{15} = 17.0\,$Å, $Z_{25} = 9.0\,$Å, $Z_{35} = 6.1\,$Å and $Z_{45} = 30.0\,$Å. 73

4-5 Comparison of gain for the four level and five level designs as a function of temperature. $\Delta E_{23} \sim 20\, meV$ and $\rho_1 = 3 \times 10^{11}\, cm^{-2}$ for both designs. The superior temperature dependence of the five level design comes from an enhanced LO phonon scattering rate for emptying the lower laser level. 75

4-6 Comparison of emission efficiency for the four level and five level designs as a function of temperature. $\Delta E_{23} \sim 20\, meV$ and $\rho_1 = 3 \times 10^{11}\, cm^{-2}$ for both designs. The emission efficiency of the five level design is not affected by enhancing the LO phonon scattering rate from the lower laser level. 76

5-1 Experimental setup for mid-infrared absorbance measurements. . . . 81

5-2 Experimental setup for far infrared emission measurements. 84

5-3 Far infrared absorption of quartz (in red) and sapphire (in green). The quartz data is for ordinary wave, applicable to Z-cut crystal. The sapphire data is an average of ordinary and extraordinary waves, applicable to random oriented crystal. 85

5-4 Step quantum well structure for the three level design. The structure is delta doped in the barriers to produce an electron density of $3 \times 10^{11} cm^{-2}$. The calculated transition energies are $\Delta E_{13} = 136.1\, meV$, $\Delta E_{12} = 114.0\, meV$ and $\Delta E_{23} = 22.1\, meV$. The calculated dipole matrix elements are $Z_{12} = 19.1$ Å, $Z_{23} = 45.3$ Å and $Z_{13} = 7.2$ Å. . . . 87

5-5 Absorption measurement for the three level design. The measured transition energies are $\Delta E_{13} = 130.2\, meV$, $\Delta E_{12} = 108.0\, meV$ and $\Delta E_{23} = 22.2\, meV$. The measured dipole matrix elements are $Z_{12} =$ 20.5 Åand $Z_{13} = 4.6$ Å. 89

5-6 Far infrared emission measurement for the three level design. The peak at 22 meV is attributed to $E_3 \rightarrow E_2$ intersubband spontaneous emission. The absorption band at 33-35 meV is due to TO phonon absorption in the Quartz window at 33.5 meV and the GaAs substrate at 34 meV. 90

5-7 Triple coupled quantum well structure for the four level design. The calculated transition energies are $\Delta E_{14} = 119.5\, meV$, $\Delta E_{13} = 82.7\, meV$, $\Delta E_{12} = 51.9\, meV$ and $\Delta E_{23} = 30.8\, meV$. The calculated dipole matrix elements are $Z_{12} = 11.8$ Å, $Z_{23} = 38.0$ Å, $Z_{13} = 9.4$ Å, $Z_{14} =$ 18.1 Å, $Z_{34} = 31.6$ Å and $Z_{24} = 9.6$ Å. 92

5-8 Absorption measurement for the four level design. Only the $E_1 \rightarrow E_4$ transition is in the mid infrared range of the MCT detector. The measured transition energy and dipole matrix element are $\Delta E_{14} =$ $119.8\, meV$ and $Z_{14} = 15.6$ Årespectively. 93

5-9 Far infrared emission measurement for the four level design. The red curve shows the emission spectrum when the CO_2 laser is tuned to resonance with the pump transition $E_4 - E_1$. The emission peak at 30.8 meV is due to $E_3 \rightarrow E_2$ intersubband spontaneous emission. The dip at 35 meV is due to TO phonon absorption in the GaAs substrate. The green curve shows what happens when the pump laser is tuned off resonance. 94

5-10 Black body emission for 200 mW of pump power polarized in the plane of the quantum well layers. Note the absence of a peak at 30.8 meV. 96

6-1 The ideal four level design. Both $E_4 - E_3$ and $E_2 - E_1$ transition energies are set to the LO phonon energy giving the optimum conditions for population inversion. A QCL laser operating at $\hbar\omega \sim 90 - 100\, meV$ is necessary to pump electrons from E_1 to E_4. 102

6-2 Cross band pumping scheme using a diode laser. 103

A-1 Absorption measurement for Sirtori's asymmetric double quantum well sample. 109

A-2 Measured far infrared difference frequency signal versus pump power. The sample is cooled to 4.2 K. The red diamonds show the far infrared difference frequency generated as a function of pump power when the signal power is kept constants at 100 mW. The red curve is a linear fit to this data. The blue squares show what happens to the trend when the signal power is kept equal to the pump power. The blue curve is a quadratic fit to this data. 111

A-3 Measured far infrared difference frequency signal versus pump and signal polarization angle. The pump and idler laser power is set at 50 mW. The sample is cooled to 4.2 K. The solid curve is a $Sin^4\phi$ fit to the data. 112

List of Tables

2.1 *Comparison of calculation results.* 32

6.1 *Summary of experimental results.* 100

6.2 *Material properties.* 105

Chapter 1

Introduction

1.1 Why Far Infrared?

The far infrared frequency range is roughly defined as $30 - 300\,\mu m$ or 4-40 meV. It is also often referred to by the term terahertz (THz) in engineering literature since 4-40 meV corresponds to 1-10 THz. The far infrared spectrum lies between two very well developed frequency ranges. The near to mid infrared $1 - 30\,\mu m$ frequency range is covered well by semiconductor diode laser technology. Diode lasers are ideal sources because they are cheap, compact and very efficient. However, the semiconductor band gap places a limitation on emission frequency. The longest wavelength diode lasers $\lambda \sim 30\,\mu m$ are based on the narrow gap lead salt semiconductor [1]. On the other end of the spectrum, semiconductor transistors can be used to make oscillators up to several hundred gigahertz (GHz) [2]. The fundamental high speed limit of transistors is set by the mobility of electrons in semiconductors. Although both transistor and diode laser technologies are constantly making inroads to extend their respective frequency ranges, there are fundamental physical constraints on how far these technologies can be pushed.

Molecular gas lasers are currently the only practical laser sources for the far infrared [3]. Molecular gas lasers are optically pumped by a CO_2 laser at $10\,\mu m$ to

excite electrons from a rotation level J in the ground vibration state to a rotation level J' in a higher vibration state. Laser emission occurs between rotation levels J' and $J'-1$ [4]. Molecular gas lasers are capable of generating milliwatts of continuous wave output power. However, these lasers are very large, consume much power, and can only be tuned by changing the gas species. Free electron lasers are tunable and generate high power in the far infrared but are even bigger and more expensive than molecular gas lasers [5].

Considerable research has been done to develop difference frequency mixers and optical parametric oscillators as sources for the far infrared [6]. The idea is to beat two CO_2 lasers with slightly different frequencies ω_p and ω_i in a nonlinear medium to generate the difference frequency $\omega_p - \omega_i$. When a resonant cavity is provided for the wave with frequency $\omega_p - \omega_i$, the resulting optical feedback can lead to oscillation. This principle can be used to make tunable coherent sources called optical parametric oscillators in the far infrared. However, the weak nonlinear susceptibility $\chi^{(2)}$ of most natural crystals makes it difficult to realize an efficient source with useful output power.

The ideal source would be similar to a semiconductor diode laser. However, since interband transition energies of semiconductors are limited by the bandgap, some perturbation must be applied to the crystal lattice to create new transitions in the far infrared. One interesting idea involves using strong crossed electric and magnetic fields to induce far infrared transitions between the heavy and light hole bands. This idea has been successfuly applied in p-type Germanium to make the only existing far infrared semiconductor laser [7]. The p-type Germanium far infrared laser is field tunable and can produce high peak power in pulse mode. The requirements of strong electric ($\sim$ 1 kV/cm) and magnetic ($\sim$ 1 Tesla) fields along with cryogenic operation are its major disadvantages. The p-type Germanium laser is currently a subject of active research and may hold good prospects for the future.

The quest for realizing a cheap, compact and efficient far infrared source continues.

A tunable coherent far infrared source would find many applications in spectroscopy, such as pollution monitoring, gas analysis, chemical agent detection and semiconductor wafer characterization [1, 8, 9]. One can also argue that once a good source is available human ingenuity will invariably find applications for it. Indeed, who ever thought in the 1960's that semiconductor diode lasers would find widespread application in compact disk players and fiber optic communication systems. The development of new laser sources is also important from a purely scientific point of view to prove that it can be done. This thesis is devoted to exploring the possibility of using optically excited intersubband transitions in quantum wells to realize a far infrared laser.

1.2 Intersubband Transitions in Quantum Wells

The idea of growing heterostructures to create quantum wells for applications in optoelectronics was first proposed by Esaki and Tsu in 1970 [10]. Advances in molecular beam epitaxy growth of atomically thin single crystal GaAs layers made this idea a practical reality [11]. Quantum wells are made by growing layers of different band gap semiconductors in a sandwich like heterostructure. Since the band gap of AlGaAs is larger than that of GaAs, band gap differences in the layers result in a potential well. The potential well height is determined by the Al alloy concentration of the barrier material.

Electrons are bound in the quantum well just like in an atom. The quantum well heterostructure breaks the perfect periodicity of the crystal lattice in the growth dimension. This perturbation is similar to a defect or an impurity atom in that new electron energy states are created localized in the quantum well. As shown in Figure 1-1, the conduction band is quantized into subbands. Electron transition energies between the subbands depend on the well width just as the spectra of natural atoms depend on their size or atomic number in the periodic table. For the single quantum

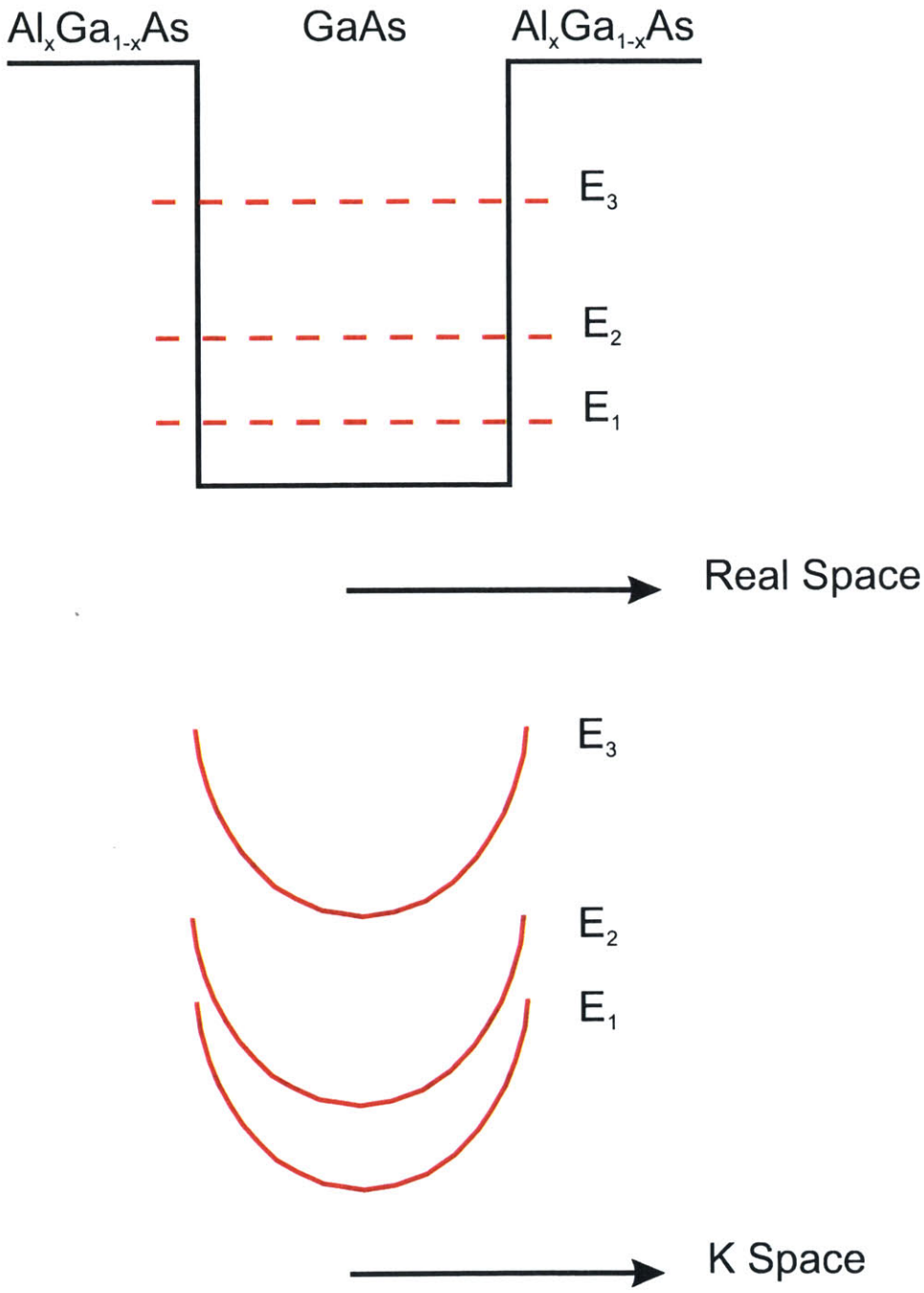

Figure 1-1: Quantum well in real space and reciprocal lattice space. The potential well caused by the $Al_xGa_{1-x}As - GaAs - Al_xGa_{1-x}As$ heterostructure in the growth direction gives rise to bound states localized in the quantum well. These bound states are represented as subbands in k space since the electrons are still free to move in the plane of the quantum well.

well of Figure 1-1, electron energies are approximated by the well known formula

$$E_n = \frac{\hbar^2}{2m^*}(\frac{n\pi}{L})^2, \tag{1.1}$$

where m^* is the electron effective mass in GaAs, L is the well width and $\hbar$ is Planck's constant. Thus, we can chose L so that electrons making transitions between E_m and E_n will emit photons in the far infrared.

The electron wavefunctions are also amenable to design by tailoring the quantum well potential. The potential profile can be manufactured to practically any shape by varying the Al alloy concentration during crystal growth. This gives the designer flexibility to engineer many physical properties of quantum wells such as intersubband absorption, stimulated emission, index of refraction, and phonon scattering. For example, it will be shown in Chapter 2 that the optical properties of electrons bound in quantum wells (or in atoms) depend on dipole matrix elements defined as

$$Z_{nm} = \int dz \psi_m^*(z) z \psi_n(z), \tag{1.2}$$

where z is in the quantum well growth direction. By proper design of the wavefunctions ψ_m and ψ_n, dipole matrix elements corresponding to particular transitions can be enhanced or suppressed. This is a powerful tool because intersubband absorption, index of refraction, and laser gain of a particular transition $E_n \rightarrow E_m$ are all proportional to Z_{nm}^2 [12, 13, 14]. The interaction of phonons with electrons bound in a quantum well also depends on overlap integrals similar to the one for dipole moment [15]. Thus, the properties of phonons can also be altered by proper engineering of the wavefunctions.

A major advantage of using quantum wells over atoms is that the dipole matrix elements of quantum wells are much larger. Dipole matrix elements are roughly the size of the atom (that is $Z_{nm} \sim L$). Since typical quantum wells are 10-100 times larger than a Hydrogen atom, so are the dipole matrix elements [16, 17]. Thus,

quantum wells appear to photons like giant atoms. This means that quantities like laser gain and nonlinear optical susceptibility will be much larger in quantum wells. Even more interesting from an engineering point of view is our ability to tune the energy levels and to some extent the dipole moments by applying a voltage bias [18, 19]. The Stark shift from an applied electric field can shift the energy levels and alter the potential profile. This provides an excellent mechanism for tuning the emission frequency of quantum well lasers. Indeed, quantum wells offer a rich amount of physics that can be applied to devise new optoelectronic devices [20, 21].

1.3 Mid Infrared Quantum Well Lasers

Lasers based on intersubband transitions in quantum wells were first proposed by Kazarinov and Suris [22]. An electrically pumped version of such a laser, called the Quantum Cascade Laser, was recently demonstrated by Faist et. al. [23]. The Quantum Cascade Laser operates by using a voltage bias to create a potential staircase in the conduction band with a quantum well forming each step. Electrons are injected from the contacts to cascade down the staircase. At each step, the electrons emit photons in intersubband transitions from an excited state of the quantum well E_3 to a lower state E_2. Electrons quickly vacate E_2 via longitudinal optical (LO) phonon emission to the ground state E_1, which is also the excited state of the next step. Figure 1-2 shows a schematic of a mid infrared electrically pumped vertical transition quantum well laser. This type of design has been very successful in covering the mid infrared frequency range 4-12 μm [24, 25, 26, 27].

More recently, a mid infrared quantum well laser operating at 15.5 μm was realized by Gauthier-Lafaye et. al. using optical pumping [28]. A schematic diagram of the optically pumped mid infrared intersubband laser is shown in Figure 1-3. This laser also uses a simple three level scheme where electrons are optically pumped from the ground state E_1 to the excited state E_3. A population inversion is ensured by

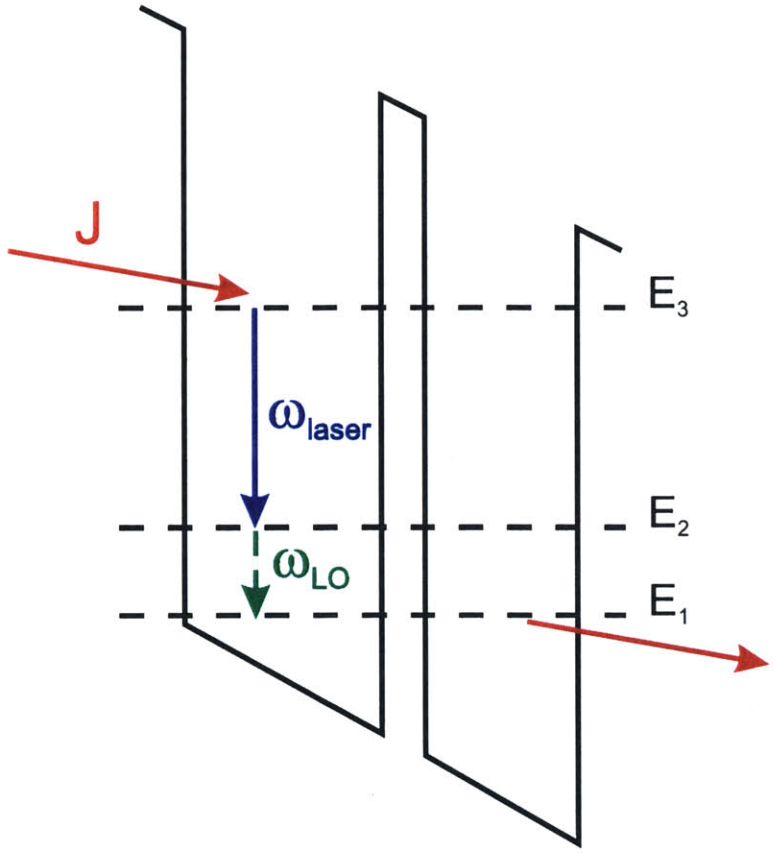

Figure 1-2: Quantum well schematic of an electrically pumped mid infrared intersubband laser. A voltage bias aligns the bands for electric pumping of the upper laser level E_3. Population inversion is assured by designing a faster phonon scattering rate emptying the lower laser level E_2 than from the upper laser level.

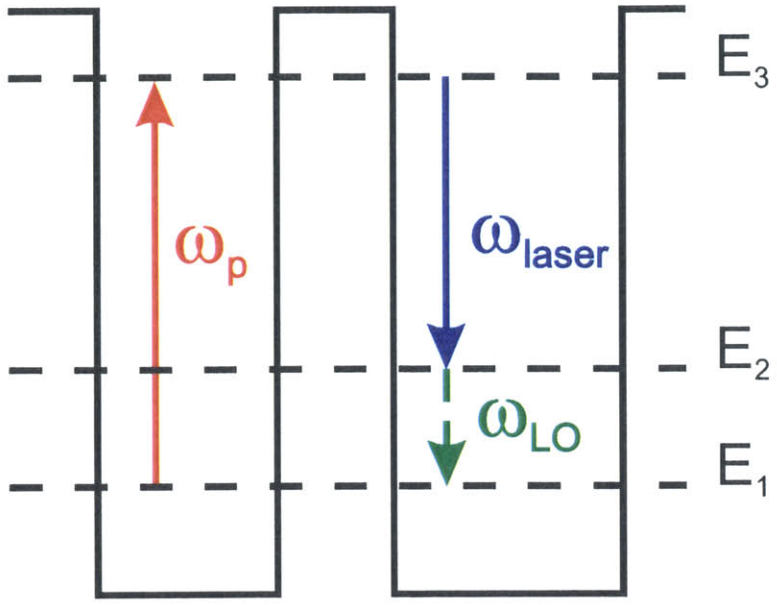

Figure 1-3: Quantum well schematic of an optically pumped mid infrared intersubband laser. Electrons are optically pumped from the ground state E_1 to the upper laser level E_3. Population inversion is assured by designing for a faster phonon scattering rate emptying the lower laser level E_2 than from the upper laser level.

designing the intersubband spacing $E_2 - E_1 \sim \hbar\omega_{LO}$ for LO phonon resonance to quickly depopulate E_2.

For longer wavelength lasers, optical pumping has the advantage of higher selectivity in populating energy levels while avoiding the free carrier losses associated with contact regions. The electrically pumped scheme is also more difficult to design since both electric and photonic transport must work properly [29]. The voltage is a free parameter in the optically pumped scheme and can be used to tune the emission frequency. On the other hand, electrical pumping is much cheaper and more efficient. Our research group has pursued both pumping schemes in search of a far infrared quantum well laser. The Ph.D. theses of Jurgen Smet [30] and Bin Xu [31] have been devoted to developing an electrically pumped far infrared quantum well laser. The optically pumped scheme is the subject of this thesis.

1.4 Toward Far Infrared Quantum Well Lasers

The idea for this work began with a suggestion by Prof. Qing Hu to consider using the giant nonlinear optical susceptibity $\chi^{(2)}$ of quantum wells to make an optical parametric oscillator (OPO) in the far infrared [32]. An analysis of OPOs based on quantum wells revealed that these devices must operate in the regime of high gain and high loss [33]. This region of parameter space has some interesting properties like oscillation without phasematching [34]. However, the high loss also means that exceedingly high threshold pump powers would be necessary. As we began to realize that OPOs based on quantum wells are not practical, the idea of a laser crystallized. Indeed, since the gain of a laser depends on $\chi^{(1)}$, a much stronger process than $\chi^{(2)}$, one can expect that the threshold pump power necessary to reach oscillation in a laser is much smaller. Calculation quickly verified our intuition and we embarked on the path toward far infrared quantum well lasers. Having already gained experience working with CO_2 lasers during the OPO project and considering the advantages of optical versus electronic pumping, the fate of my Ph.D. thesis project was sealed. This thesis describes my theoretical and experimental work toward optically pumped far infrared quantum well laser.

The successful mid infrared quantum well laser served as an inspiration in the beginning of this project. Indeed, one can envision scaling the mid infrared quantum well laser designs to the far infrared by simply changing the well widths in Figure 1-3. As we shall see in later chapters, this logical approach was doomed to failure. The difficulties of scaling a mid infrared quantum well laser to the far infrared are somewhat analogous to the differences between semiconductor diode lasers operating at $\sim$ 800 nm for reading compact disks versus semiconductor diode lasers operating at $\sim$ 1550 nm for fiber optic communications. The emission efficiency of the longer wavelengths semiconductor diode lasers is an order of magnitude lower due to increased Auger scattering [35]. Similarly, when one tries to scale intersubband quantum well lasers from mid infrared wavelengths to the far infrared, the emission

efficiency drops by many orders of magnitude. It becomes extremely difficult even to measure spontaneous emission.

Initial measurements using a scaled version of the simple three energy level scheme in a step quantum well yielded poor experimental results. The emission power was very weak ($\sim$ 1 pW) and it was difficult to clearly resolve the spectrum. It became evident that three level systems lack enough flexibility to optimize the gain and emission efficiency. This lack of flexibility in three level designs comes from the necessity to couple the CO_2 pump laser to the same transition $E_1 \rightarrow E_3$ that couples the LO phonon scattering responsible for limiting the gain and emission efficiency.

It was necessary to abandon old ways of thinking to create new design ideas. We realized that the real power of quantum wells as artificial atoms lies in more complex designs involving higher energy level schemes [36]. We proposed and analyzed a four level scheme using triple coupled quantum wells that effectively decoupled the pumping rate from the LO phonon scattering rate appearing in the gain and emission efficiency. Thus, these two important rates could be optimized independently, improving the gain and emission efficiency by an order of magnitude over previous three level designs. Optically pumped intersubband far infrared emission experiments verified the superior qualities of the four level system. The four level design exhibited an order of magnitude stronger emission power. The stronger emission made possible the first clear measurement of a far infrared spontaneous emission spectrum from optically pumped quantum wells [37].

The emission measurements also revealed an important problem. The measured emission power from both three and four level designs was an order of magnitude weaker than expected. This discrepancy was identified as being due to heating effects. Heating of the electron gas can result in the opening of a parasitic LO phonon scattering channel for electrons in the upper laser level. A new five level design scheme using quadruple coupled quantum wells was proposed and analyzed to improve high temperature performance by enhancing the scattering rate from the lower laser level.

The five level scheme extends the temperature range of optically pumped far infrared quantum well lasers beyond 100 K.

Chapter 2

Intersubband Transitions in Quantum Wells

2.1 Electron States in Quantum Wells

In this chapter we develop the analytical tools necessary to analyze lasers based on intersubband transitions. We start with a brief description of electron states in quantum wells. Block's Theorem asserts that the wavefunction of an electron in the conduction band of a semiconductor must be of the form [38]

$$\Psi(r) = \frac{1}{\sqrt{V}} F(r) U(r), \tag{2.1}$$

where U(r) contains the periodicity of the crystal lattice and F(r) is a slowly varying envelope function. In a perfect crystal lattice, the envelope function is a plane wave

$$F(r) = \frac{e^{i\mathbf{k}\cdot\mathbf{r}}}{\sqrt{V}}, \tag{2.2}$$

meaning that electrons can move freely through the crystal. Imperfections such as impurities, defects, and interfaces, introduce perturbations that break the perfect periodicity of the crystal. Electrons can be bound in the local potential well created

by such disruptions in the crystal lattice.

Artificially grown quantum well heterostrucures also introduce new energy states where electrons are bound like in an impurity atom. The electron wavefunction is still described by a Block state, with the caveat that the envelope function is spatially localized in the quantum well

$$F_n(r) = \frac{e^{i\mathbf{k}_{||}\cdot\mathbf{r}}}{\sqrt{A}}\psi_n(z). \tag{2.3}$$

The envelope wavefuction $\psi_n(z)$ is the bound state induced by the quantum well heterostructure in the z direction. The plane wave $e^{i\mathbf{k}_{||}\cdot\mathbf{r}}$ reflects the fact that electrons are still free to move in the xy-plane of the quantum well.

The Effective Mass Theorem allows us to calculate the energy levels and envelope wavefunctions in a quantum well from a simple one dimensional Schrödinger equation

$$(-\frac{\hbar^2}{2m^*}\frac{d^2}{dz^2} + V(z))\psi_n(z) = E_n\psi_n(z) \tag{2.4}$$

where m^* is the effective mass, V(z) is the potential profile of the quantum well heterostructure, and E_n is the bound state energy. Including the kinetic energy of motion in the xy-plane, the total energy of an electron in state $(E_n, k_{||})$ is

$$E = E_n + \frac{\hbar^2 k_{||}^2}{2m^*}. \tag{2.5}$$

The effect of the quantum well potential is to quantize the conduction band electron states into subbands. The wavefunctions corresponding to these electron states are localized in the quantum well. This provides the physical basis for treating quantum wells as artificial atoms. Thus, many useful concepts in atomic physics, like emission and absorption cross section, can also be applied to quantum wells. This analogy between atoms and quantum wells will be developed further in the derivation of laser gain.

It will be shown in later chapters that the optimum quantum well design for far infrared lasers requires complex energy level schemes in triple and quadruple coupled quantum well structures. A numerical solution of Schrödinger's equation is necessary to solve for the energy levels and wavefunctions in these complex quantum well structures. The numerical approach we use involves transforming the wave equation into a matrix equation [39]. The eigenvalues and eigenstates of the matrix equation correspond to the bound state energy levels and wavefunctions of Schrödinger's equation. The matrix equation is solved by standard numerical algebraic methods. The second order effects on electron energy levels and wavefunctions due to band nonparabolicity are included using a perturbation technique [40, 41]. Once the electron energy levels and wavefunctions are known, Fermi-Dirac distribution functions are used to calculated the electron density in the quantum wells. The electron density feeds into the Poisson equation. Solution of the Poisson equation gives a correction to the electron potential energy which is fed back into the Schrödinger equation solver. Thus, the Schrödinger and Poisson equations are solved self consistently by an iteration procedure.

Before using the numerical simulation code in design, it is important to test its accuracy against published data for a known quantum well structure. We tested our code by comparing its numerical calculation results with experimental and theoretical data published by Sirtori et. al. for an asymmetric double quantum well structure [42]. Sirtori's structure is similar to our quantum well designs it terms of the quantum well thicknesses, comparable doping levels, and the use of AlGaAs-GaAs material system. Figure 2-1 shows our calculation of the energy levels and square of the wavefunctions for Sirtori's structure. The double coupled quantum well structure is composed of 61 and 70 Å thick GaAs wells separated by a thin 20 Å $Al_{0.33}Ga_{0.67}As$ barrier. A ground state sheet electron density of $4 \times 10^{11}\, cm^{-2}$ is assumed. This structure was designed for far infrared difference frequency mixing experiments. Dr. Carlo Sirtori kindly provided us with a piece of his sample wafer to test our far

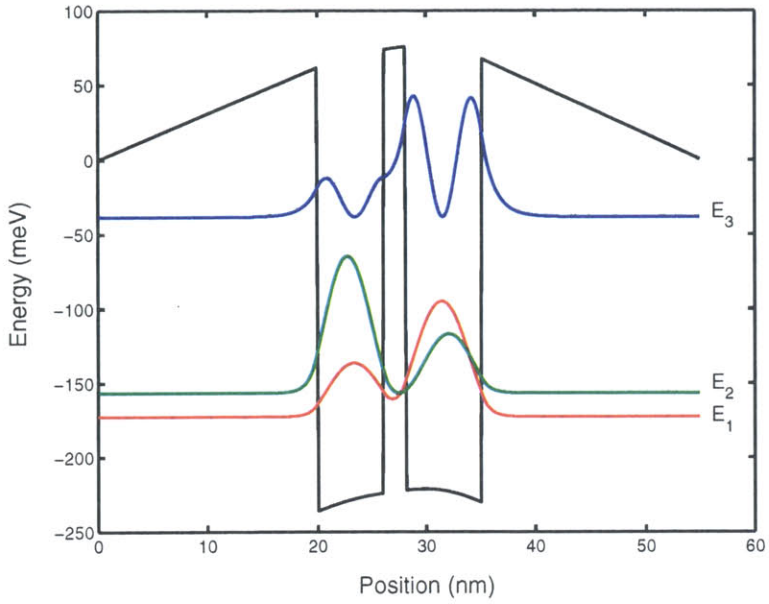

Figure 2-1: The calculated energy levels and wavefunctions for Sirtori's asymmetric double quantum well structure.

Table 2.1: *Comparison of calculation results.*

	$E_2 - E_1$ (meV)	$E_3 - E_1$ (meV)	Z_{12} (Å)	Z_{13} (Å)
MIT (Author)	16.0	134.3	39.6	8.0
Bell Labs (Sirtori)	14.1	136.0	40.0	8.0

infrared experimental system (see Apendix A) and theoretical simulation code.

Table 2.1 shows a comparison of our calculation results for the energy levels and dipole matrix elements against Sirtori's published results using the Bell Labs simulation code. The calculated energy levels agree to within a few meV. The calculated dipole matrix elements show excellent agreement, indicating very similar results for the wavefunctions. The close correspondence between our calculation results and the extensively tested Bell Labs simulation code verifies the accuracy of our numerical approach for solving Schrödinger's equation. This provides confidence that our calculated energy levels and wavefunctions give an accurate representation of electron states in quantum wells.

2.2 Radiative Intersubband Transitions

Electrons bound in a quantum well can be induced to undergo transitions by absorbing or emitting photons. The interaction Hamiltonian for this process is given by the dipole interaction [43]

$$H = -e\mathbf{E}(\mathbf{r}, t) \cdot \mathbf{r}. \tag{2.6}$$

The electric field must be quantized in order to accurately describe the interaction between photons and electrons. According to the rules of quantum mechanics, each mode of the electromagnetic field is quantized as a harmonic oscillator by replacing the field amplitude by an operator. A photon is then defined as one quantum of excitation in a particular mode.

The operator for a single plane wave mode with frequency ω and wavevector κ is given by [43]

$$\mathbf{E}(\mathbf{r}, \mathbf{t}) = -i\sqrt{\frac{\hbar\omega}{2V\epsilon}}[a^{\dagger}e^{-i\kappa\cdot\mathbf{r}+i\omega t} - ae^{i\kappa\cdot\mathbf{r}-i\omega t}], \tag{2.7}$$

where we assume that the field is polarized in the z direction corresponding to the growth direction of the quantum well. Only modes in this polarization direction can couple to intersubband transitions [44]. The operators $a^{\dagger}$ and a are analogous to the creation and destruction operators of a quantized harmonic oscillator [45]. They are defined by the commutation rule $[a,a^{\dagger}]=1$.

In a photon emission process only the term containing the photon creation operator $a^{\dagger}$ contributes to the interaction. The initial electron state is assumed to be in subband E_i with in plane wavevector k_i and the initial state of the electromagnetic field is assumed to be in a photon number state n_{ph}, abbreviated by (E_i, k_i, n_{ph}). The final state is assumed to be in state $(E_f, k_f, n_{ph} + 1)$. The electron-photon (or phonon) scattering process is depicted schematically in Figure 2-2. The dipole inter-

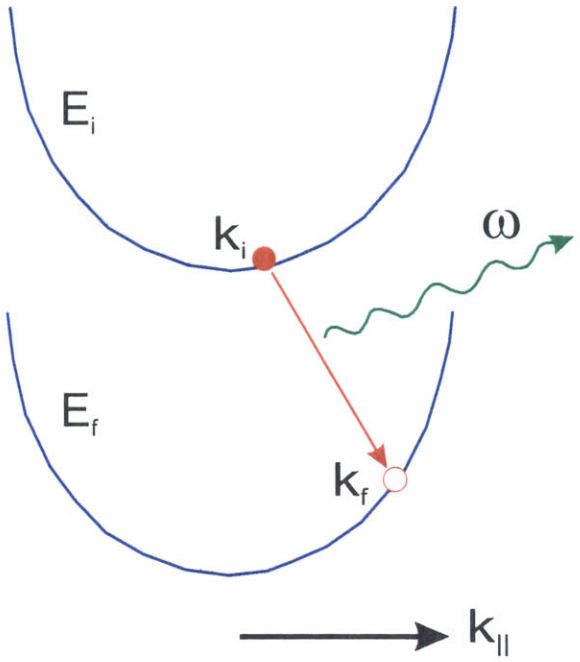

Figure 2-2: The emission process of a photon (or phonon) in electronic intersubband transitions between subbands E_i and E_f.

action Hamiltonian matrix element, abbreviated by H_{if}, is given by

$$H_{if} = ie\sqrt{\frac{\hbar\omega}{2V\epsilon}}Z_{if}e^{i\omega t}\sqrt{n_{ph}+1}. \tag{2.8}$$

Integration over r in the plane of the quantum well gives a vanishing result for H_{if} unless $k_i = k_f + \kappa$. This is a statement of momentum conservation. Since photons carry very little momentum, only vertical transitions $k_i = k_f$ are allowed. The vertical transition selection rule for electron-photon scattering is not universal and will be relaxed when we discuss electron-phonon scattering.

The strength of the dipole interaction is characterized by the dipole matrix element Z_{if} defined by

$$Z_{if} = \int dz\psi_f^*(z)z\psi_i(z). \tag{2.9}$$

The dipole matrix element is roughly the size of the quantum well. Thus, quantum wells look to photons like giant atoms with $Z \sim 10 - 100$ Å in comparison to a

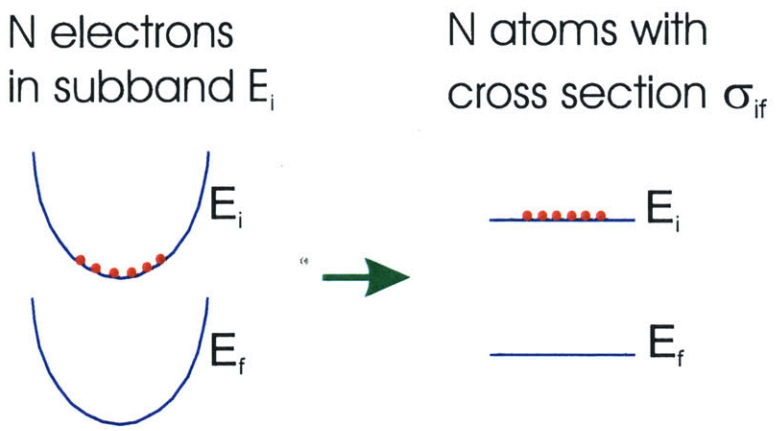

Figure 2-3: For a photon with $\hbar\omega \sim E_i - E_f$, the ensemble of electrons in subband E_i looks like a collection of two level atoms with cross section σ_{if}.

Hydrogen atom $Z \sim 1$ Å.

2.2.1 Stimulated Emission and Gain

The transition rate between states (E_i, k_i, n_{ph}) and $(E_f, k_f, n_{ph}+1)$ induced by the dipole interaction is calculated by Fermi's Golden Rule [46]

$$W_{i\to f} = \frac{2\pi}{\hbar}|H_{if}|^2\delta(E_i - E_f - \hbar\omega) = \frac{\pi e^2\omega Z_{if}^2(n_{ph}+1)}{V\epsilon}\delta(E_i - E_f - \hbar\omega), \qquad (2.10)$$

where the delta function enforces conservation of energy. This delta function can be replaced by a Lorentzian lineshape to include broadening effects due to finite lifetime and dephasing scattering. The term proportional to photon number n_{ph} is the stimulated emission rate. Including the broadening effects, the stimulated emission rate is given by

$$W_{i\to f}^{stim} = \frac{e^2\omega Z_{if}^2 n_{ph}}{V\epsilon}\frac{\frac{\Gamma}{2}}{(E_i - E_f - \hbar\omega)^2 + (\frac{\Gamma}{2})^2}, \qquad (2.11)$$

where Γ is the full width at half maximum (FWHM) or transition linewidth. The linewidth Γ is an important parameter, generally obtained from emission or absorption spectroscopy experiments.

We have calculated the transition rate for a single electron in some initial state

(E_i, k_i). For the calculation of gain, we must add up the stimulated emission rate of every electron undergoing stimulated transitions from subband E_i to subband E_f. Note however that the stimulated emission rate $W_{i\to j}^{stim}$ does not depend on k_i. Thus, ignoring the small effects of nonparabolicity, every electron on subband E_i gives the same contribution to the stimulated emission rate. As shown in Figure 2-3, we can think of all the electrons in subband E_i as a collection of atoms in the same state. This simplifying analogy allows us to borrow the concept of emission cross section from atomic physics [47]. The emission cross section is defined by

$$\sigma_{if} = \frac{\hbar\omega W_{i\to f}}{I}, \tag{2.12}$$

where

$$I = v_g \frac{\hbar\omega n_{ph}}{V} \tag{2.13}$$

is the photon energy flux. The group velocity v_g of a photon is simply the speed of light in the material. Thus, the emission cross section is given by

$$\sigma_{if} = \frac{e^2\omega Z_{if}^2}{c\epsilon_0 n} \frac{\frac{\Gamma}{2}}{(E_i - E_f - \hbar\omega)^2 + (\frac{\Gamma}{2})^2}. \tag{2.14}$$

The gain is obtained from the emission cross section by $g = \Delta n_{if}\sigma_{if}$, where Δn_{if} is the population inversion between the subbands. We often make calculations in terms of a two dimensional sheet electron density ρ. The population inversion is then written as $\Delta n_{if} = (\rho_i - \rho_f)/L$, where L is the quantum well width. Finally, since the laser mode is generally not perfectly confined in the multiple quantum well active region, we must multiply the single well gain by the confinement factor γ_{conf} [35]. The mode confinement factor will be defined more precisely in Chapter 3. Thus, the total gain is given by

$$g = \frac{e^2\omega Z_{if}^2(\rho_i - \rho_f)\gamma_{conf}}{c\epsilon_0 nL} \frac{\frac{\Gamma}{2}}{(E_i - E_f - \hbar\omega)^2 + (\frac{\Gamma}{2})^2}. \tag{2.15}$$

Subband nonparabolicity effects were ignored to simplify the derivation of gain. This simplification is justified for far infrared transitions in GaAs, where the nonparabolicity effect is very weak. A perturbation technique can be used to include nonparabolicity as a small correction to the energy levels and dipole matrix element in the gain expression [41]. In materials such as InGaAs, where nonparabolicity is much stronger, a more rigorous density matrix analysis must be used to derive the gain lineshape. Strong nonparabolicity effects lead to additional broadening and an asymmetrical gain lineshape [48].

2.2.2 Spontaneous Emission

The spontaneous emission rate plays an important role in the analysis of lasers because the emission efficiency below threshold depends on a ratio of spontaneous emission rate to nonradiative scattering rate. The spontaneous emission rate into a single mode (ω, κ) is obtained by taking $n_{ph} = 0$ in equation 2.10. The term "spontaneous" actually conceals the real physics behind this process. Spontaneous emission is really stimulated emission due to ever present vacuum fluctuations in the electromagnetic field [49]. The total spontaneous emission rate is calculated by summing the emission into every possible electromagnetic mode in the cavity that couples to intersubband transitions. The total spontaneous emission rate from subband E_i to E_f is thus calculated to be [30]

$$W_{i\to f}^{spon} = \frac{1}{\tau_{if}^{spon}} = \frac{e^2 n \omega^3 Z_{if}^2}{3\pi c^3 \epsilon_0 \hbar}. \tag{2.16}$$

In the calculation of $W_{i\to f}^{spon}$ we assumed a 3D density of states for the electromagnetic field. This assumption is justified in our emission experiments (see Chapter 5) where the waveguide dimensions are much larger than the emission wavelength.

One way to improve the emission efficiency is to use a microcavity designed to enhance the spontaneous emission rate. For example, if the vertical (z direction)

dimension t of the waveguide is made smaller than the wavelength, the spontaneous emission is more strongly coupled to modes with the correct polarization. The total spontaneous emission rate is then enhanced by a factor of $\frac{3}{4}\frac{\lambda}{t}$ [50, 31].

Changing to a material with smaller effective mass can also enhance the spontaneous emission rate. A semiconductor with smaller effective mass requires a larger well width to maintain the same intersubband energy separation. Thus, the dipole moments are enhanced by a factor of $\sim \sqrt{\frac{m^*_{GaAs}}{m^*_{InGaAs}}}$ when the well material is changed from GaAs to InGaAs. All of our quantum well designs were grown using GaAs because molecular beam epitaxy is more available for the AlGaAs-GaAs material system. However, since InGaAs has a smaller effective mass, the InAlAs-InGaAs material system may be a good choice for future work. The effective mass also plays a role in electron-phonon scattering as we shall see next.

2.3 Phonon Intersubband Scattering

The electron-phonon interaction is the most important nonradiative scattering mechanism in intersubband transitions. For a given pumping rate, the phonon scattering rates determine the subband populations, gain, and emission efficiency of quantum well lasers.

The lattice vibrations in a semiconductor crystal are quantized in a similar manner as the electromagnetic field. Each mode is treated as a quantized harmonic oscillator by replacing classical amplitudes by creation and destruction operators. A phonon is defined as one quantum of excitation in a particular mode. The electron-phonon interaction is the mechanism by which electrons can be induced to undergo intersubband transitions by absorbing or emitting phonons. The electron-phonon interaction Hamiltonian is given by [15]

$$H = \sum_{\mathbf{q}} \alpha(\mathbf{q})(e^{-i\mathbf{q}\cdot\mathbf{r}} b^{\dagger}_{\mathbf{q}} + e^{i\mathbf{q}\cdot\mathbf{r}} b_{\mathbf{q}}), \tag{2.17}$$

where $b_{\mathbf{q}}^{\dagger}$ and $b_{\mathbf{q}}$ are the creation and destruction operators for a phonon in mode $\mathbf{q}$, and $\alpha(\mathbf{q})$ is the interaction strength. The sum is over all possible phonon wavevectors $\mathbf{q}$ since we are interested in calculating the total scattering rate.

Lattice vibrations can be polarized transverse or longitudinal relative to the propagation direction. The dominant contribution to the electron-phonon interaction in GaAs comes from modes polarized in the longitudinal direction. The perturbation potential due to lattice deformation by long wavelength longitudinal acoustic vibrations is the most important interaction for small energies. The longitudinal acoustic (LA) phonon interaction strength is given by

$$|\alpha(\mathbf{q})|^2 = \frac{\hbar\omega D^2}{2\rho V c_s^2}, \tag{2.18}$$

where D is the deformation potential, ρ is the density, V is the crystal volume, and c_s is the longitudinal sound velocity. For polar semiconductors like GaAs, the Fröhlich interaction gives rise to longitudinal optical (LO) phonon scattering. LO phonons have a strong resonance at 36 meV in GaAs. Thus, in contrast to the linear dispersion relation of LA phonons $\omega = c_s q$, the dispersion relation of LO phonons is approximated as a constant $\omega = \omega_{LO}$. The Fröhlich interaction strength is given by

$$|\alpha(\mathbf{q})|^2 = \frac{\hbar\omega_{LO} e^2(\epsilon_s - \epsilon_\infty)}{2\epsilon_s\epsilon_\infty\epsilon_0 V q^2}, \tag{2.19}$$

where ϵ_∞ and ϵ_s are the high frequency and static dielectric constants. The $1/q^2$ dependence means that the Fröhlich interaction is greatly enhanced when the phonon momentum is small. It is also important to note that at low temperatures, when electrons occupy states close to the bottom of the subbands, LO phonon scattering can only occur for subband energy separation equal to or greater than the LO phonon energy $\hbar\omega_{LO}$.

For the phonon emission process, we only need the term containing the phonon creation operator in the interaction Hamiltonian. The interaction Hamiltonian matrix

element connecting states (E_i, k_i, n_{ph}) and $(E_f, k_f, n_{ph}+1)$ is then calculated to be

$$H_{if} = \alpha(\mathbf{q}) A_{if}(q_z) \sqrt{n_{ph}+1}\, \delta_{\mathbf{k_i}-\mathbf{k_f},\mathbf{q}_{||}}, \tag{2.20}$$

where $A_{if}(q_z)$ is a form factor

$$A_{if}(q_z) = \int_{-\infty}^{+\infty} dz \psi_f^*(z) e^{-iq_z z} \psi_i(z). \tag{2.21}$$

As in the calculation of the dipole interaction matrix element, integration over r in the plane of the quantum well gives a vanishing result for H_{if} unless conservation of momentum $k_i = k_f + q_{||}$ is preserved. Since phonons can carry comparable momentum to electrons, we cannot ignore $q_{||}$. In contrast to radiative transitions, phonon induced transitions need not be vertical in k space. The form factor $A_{if}(q_z)$ has the appearance of a Fourier transform of $\psi_f^*(z)\psi_i(z)$. Thus, since the electron wavefunctions are localized in the quantum well, we expect $A_{if}(q_z)$ to be sharply peaked at $q_z \sim \frac{1}{L}$. Physically this means that only those phonons with wavelength comparable to the quantum well width interact strongly with the bound electrons.

Fermi's Golden Rule is used to calculate the phonon scattering rate of electrons from state (E_i, k_i, n_{ph}) to $(E_f, k_f, n_{ph}+1)$. Summing over all possible final electron states k_f, we get

$$\frac{1}{\tau_{if}} = \frac{2\pi}{\hbar} \sum_{\mathbf{k}_f} \sum_{\mathbf{q}_{||}} \sum_{q_z} |\alpha(\mathbf{q})|^2 |A_{if}(q_z)|^2 (n_{ph}+1) \delta_{\mathbf{k_i}-\mathbf{k_f},\mathbf{q}_{||}} \delta(E_i - E_f + \frac{\hbar^2}{2m^*}(k_i^2 - k_f^2) - \hbar\omega). \tag{2.22}$$

The summation is converted to an integral in reciprocal lattice space in the usual manner. Figure 2-4 shows the geometrical relationship between the wavevectors required for conservation of momentum. Thus, we get for LA phonon scattering

$$\frac{1}{\tau_{if}^{LA}} = \frac{D^2}{8\pi^2 \rho c_s^2} \int_{-\infty}^{+\infty} dq_z |A_{if}(q_z)|^2 \int_0^{2\pi} d\theta \int_0^{+\infty} dk_f k_f \omega (n_{ph}+1) \delta(E_i - E_f + \frac{\hbar^2}{2m^*}(k_i^2 - k_f^2) - \hbar\omega), \tag{2.23}$$

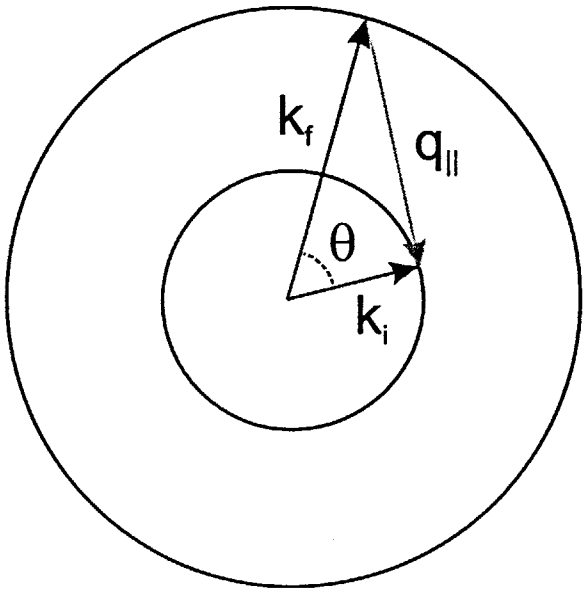

Figure 2-4: The geometrical relationship in reciprocal lattice space required for conservation of momentum. The total phonon scattering rate from state (E_i, k_i) is obtained by summing the scattering rate to all final electron states (E_f, k_f). This involves an integration over θ.

where

$$\omega = c_s\sqrt{q_z^2 + q_{||}^2} = c_s\sqrt{q_z^2 + k_i^2 + k_f^2 - 2k_i k_f cos\theta}, \tag{2.24}$$

and n_{ph} is the Bose-Einstein phonon occupation probability

$$n_{ph} = \frac{1}{e^{\frac{\hbar\omega}{kT}} - 1}. \tag{2.25}$$

We indicated above that only phonons with $\lambda \sim \frac{1}{L}$ or $\hbar\omega \sim \hbar\frac{c_s}{L} \sim 1$ meV interact strongly with electrons. Thus, LA phonon modes begin to fill up at a relatively low temperature $kT \sim 1$ meV. LA phonon scattering increases quickly with temperature even in cryogenic conditions. This temperature effect is absent in LO phonon scattering, where $\hbar\omega = \hbar\omega_{LO} > kT$ up to room temperature. However, LO phonon scattering suffers from a high temperature threshold phenomenon as intersubband transition energies approach the LO phonon energy. We will study high temperature effects on LO phonon scattering in Chapter 4.

The simple dispersion relation of LO phonons allows us to take advantage of the energy conserving delta function to simplify the integration. Using the dispersion relation $\hbar\omega = \hbar\omega_{LO}$ and transforming integration over k_f to an integration over energy, we get for LO phonon scattering

$$\frac{1}{\tau_{if}^{LO}} = \frac{m^* e^2 \omega_{LO}(\epsilon_s - \epsilon_\infty)}{2\hbar^2 \epsilon_s \epsilon_\infty \epsilon_0}(n_{ph}+1)\int_0^{2\pi} d\theta \int_{-\infty}^{+\infty} dz \int_{-\infty}^{+\infty} dz' \psi_f^*(z)\psi_i(z)\frac{e^{-q_{||}|z-z'|}}{q_{||}}\psi_i^*(z')\psi_f(z'), \tag{2.26}$$

where

$$q_{||} = \sqrt{k_i^2 + k_f^2 - 2k_i k_f cos\theta} \tag{2.27}$$

is the phonon momentum in the plane of the quantum well. LO phonon scattering has a $\frac{1}{q_{||}}$ dependence on phonon momentum. Thus, LO phonon scattering is especially strong for transitions near the Γ point when the subband separations are close to the LO phonon energy $E_i - E_f \sim \hbar\omega_{LO}$. In this case the transitions are almost vertical requiring phonons with small momenta.

It is interesting to consider the dependence of LO phonon scattering on effective mass. On the surface equation 2.26 seems to imply a direct $\propto m^*$ dependence on effective mass. However, we must also take into account the effective mass dependence of exchange momentum in the $\frac{1}{q_{||}}$ term. The exchanged momentum is smaller for reduced effective mass, leading to an additional $\frac{1}{\sqrt{m^*}}$ dependence in the LO phonon scattering rate. We still win by going to a material with smaller effective mass. The LO phonon scattering rate is reduced when going from GaAs to InGaAs by the factor $\sim \sqrt{\frac{m^*_{InGaAs}}{m^*_{GaAs}}}$. This is an important consideration in choosing materials since weaker nonradiative scattering leads to a higher population inversion and emission efficiency. The dependence of population inversion and emission efficiency on nonradiative scattering is derived in the next section.

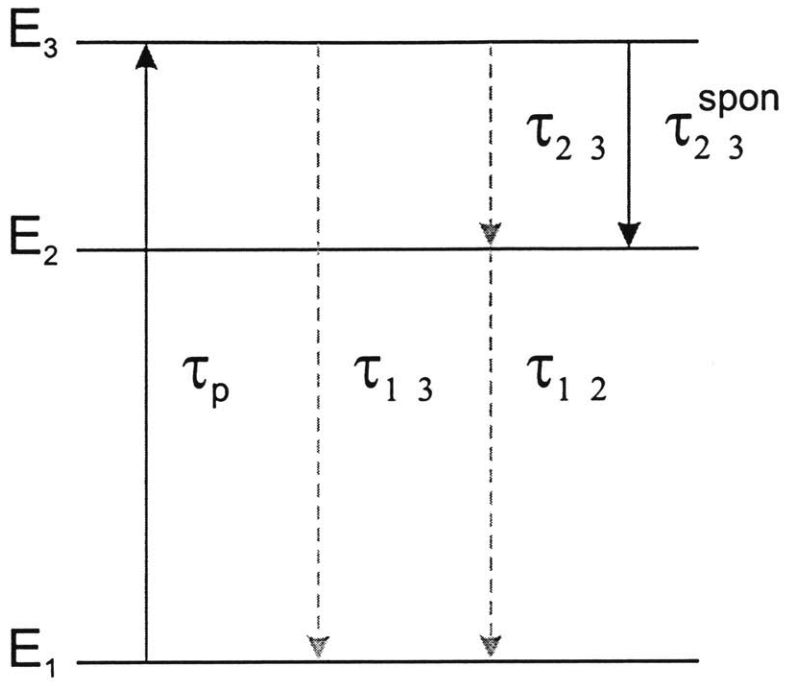

Figure 2-5: The three level system. Electrons are pumped from the ground state E_1 to E_3. Population inversion is created between subbands E_3 and E_2 by engineering a faster phonon scattering rate $\frac{1}{\tau_{12}}$ than $\frac{1}{\tau_{23}}$. The phonon scattering rate $\frac{1}{\tau_{13}}$ also plays an important role in determining the magnitude of gain and emission efficiency.

2.4 Rate Equation Analysis

2.4.1 Three Level System

The phonon scattering rates determine how fast excited electrons decay down to the ground state. This population relaxation is balanced by the optical excitation or pumping rate. A steady state population inversion can result for certain favorable ratios of phonon scattering rates. We first analyze the simple three level system shown in Figure 2-5. In the three level scheme, electrons are optically pumped from the ground state E_1 to E_3. Population inversion is ensured by designing a faster depopulation rate of the lower laser level $\frac{1}{\tau_{12}}$ than the scattering rate from the upper laser level $\frac{1}{\tau_{23}}$.

The steady state subband population densities are calculated using a rate equation

analysis. The rate equations for the three level laser below threshold are given by

$$\frac{d\rho_3}{dt} = \frac{1}{\tau_p}\rho_1 - (\frac{1}{\tau_{13}} + \frac{1}{\tau_{23}})\rho_3, \tag{2.28}$$

$$\frac{d\rho_2}{dt} = \frac{1}{\tau_{23}}\rho_3 - \frac{1}{\tau_{12}}\rho_2, \tag{2.29}$$

$$\frac{d\rho_1}{dt} = -\frac{1}{\tau_p}\rho_1 + \frac{1}{\tau_{12}}\rho_2 + \frac{1}{\tau_{13}}\rho_3, \tag{2.30}$$

where

$$\frac{1}{\tau_p} = \frac{I_p\sigma_{13}}{\hbar\omega_p} \tag{2.31}$$

is the optical pumping rate from E_1 to E_3. The pump absorption cross section σ_{13} is defined similarly to the emission cross section and I_p is the pump laser intensity. Note that we have ignored the stimulated emission rate for the laser transition since below threshold it is much smaller than the nonradiative phonon scattering rates.

The population inversion is obtained in steady state by setting $\frac{d}{dt} = 0$, resulting in

$$\rho_3 - \rho_2 = (1 - \frac{\tau_{12}}{\tau_{23}})\frac{\tau_3^{tot}}{\tau_p}\rho_1, \tag{2.32}$$

where

$$\frac{1}{\tau_3^{tot}} = \frac{1}{\tau_{13}} + \frac{1}{\tau_{23}} \tag{2.33}$$

is the total scattering rate from level E_3. The steady state subband population ρ_1 is obtained from the additional constraint $\rho_1 + \rho_2 + \rho_3 = \rho_e$, where ρ_e is the total electron density in the quantum well when the pump laser is turned off. Thus, the complete expression for population inversion is

$$\rho_3 - \rho_2 = (1 - \frac{\tau_{12}}{\tau_{23}})\frac{\tau_3^{tot}}{\tau_p}\frac{\rho_e}{1 + \frac{\tau_3^{tot}}{\tau_p} + \frac{\tau_3^{tot}\tau_{12}}{\tau_{23}\tau_p}}. \tag{2.34}$$

We see that population inversion is only possible when the scattering rate $\frac{1}{\tau_{12}}$ is faster than the scattering rate $\frac{1}{\tau_{23}}$. This means that the depopulation of the lower

laser level must be faster than the relaxation from the upper level. Note also that the magnitude of population inversion is directly proportional to a ratio of optical pumping rate to the the total phonon scattering rate from the upper laser level $\frac{1}{\tau_3^{tot}}$. This ratio also determines the maximum pump intensity for saturation of the pump transition. Equation 2.34 implies that the population inversion at saturation can never exceed $\frac{\rho_e}{2}$.

The emission efficiency also depends critically on the phonon scattering rates. The total spontaneous emission power for intersubband transitions from $E_3 \rightarrow E_2$ is given by

$$I_{em} = \frac{\hbar\omega_{23}\rho_3}{\tau_{23}^{spon}} = \hbar\omega_{23}\frac{\tau_3^{tot}}{\tau_{23}^{spon}}\frac{\rho_1}{\tau_p}. \tag{2.35}$$

Using the expression for $\frac{1}{\tau_p}$ in terms of I_p and taking a ratio of spontaneous emission power to pump power, we get the spontaneous emission efficiency

$$\eta_{3L} = \frac{I_{em}}{I_p} = \sigma_{13}\rho_1\frac{\hbar\omega_{23}}{\hbar\omega_{13}}\frac{\tau_3^{tot}}{\tau_{23}^{spon}}. \tag{2.36}$$

The emission efficiency depends most importantly on a ratio of spontaneous emission rate to the fastest nonradiative (LO phonon) scattering rate from the upper laser level $\frac{1}{\tau_3^{tot}}$. This scattering rate plays an important role in limiting the maximum emission efficiency and gain. The pump absorption cross section σ_{13} is also an important factor in both emission efficiency and gain. A major deficiency of three level systems is the necessity to use the same transition for the pump laser $E_1 \rightarrow E_3$ that also governs the dominant parasitic LO phonon scattering path.

2.4.2 Four Level System

Although the three level system is the simplest to design, we will see in Chapter 3 that it is by far not the ideal system for achieving a laser. The higher complexity of the four level system, shown in Figure 2-6, can be used to our advantage in optimizing the laser gain and emission efficiency. In the four level design, electrons are pumped from the

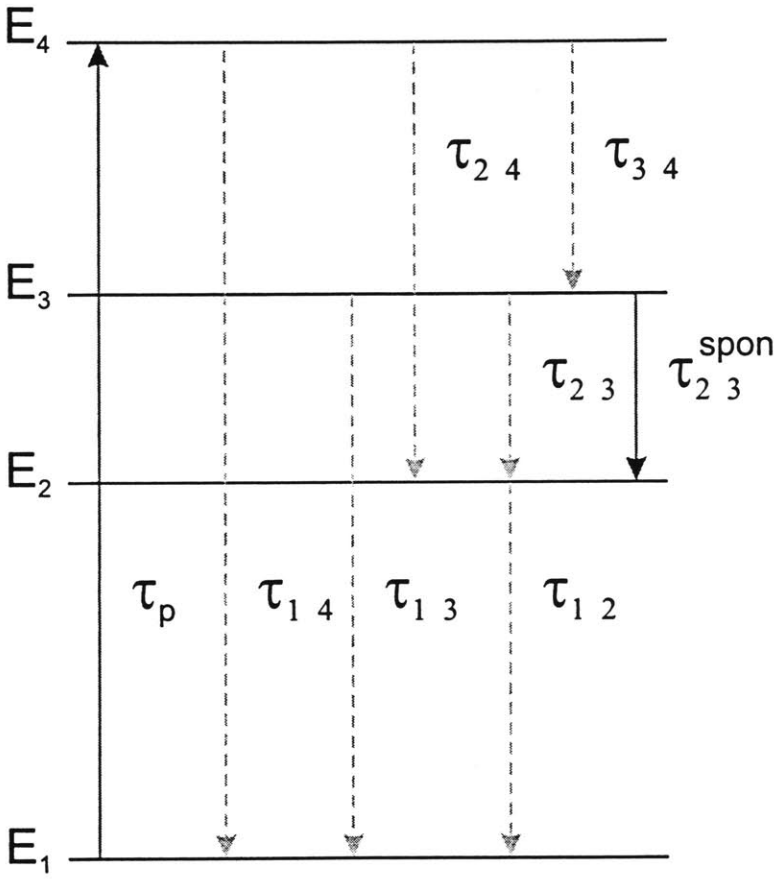

Figure 2-6: The four level system. Electrons are pumped from the ground state E_1 to E_4, followed by a fast relaxation to subband E_3. Population inversion is created between subbands E_3 and E_2 by engineering a faster phonon scattering rate $\frac{1}{\tau_{12}}$ than $\frac{1}{\tau_{23}}$ and $\frac{1}{\tau_{24}}$. The phonon scattering rate $\frac{1}{\tau_{13}}$ also plays an important role in determining the magnitude of gain and emission efficiency.

ground state E_1 to subband E_4, followed by a fast LO phonon scattering to subband E_3. A population inversion is created between subbands E_3 and E_2 by engineering a faster phonon scattering rate $\frac{1}{\tau_{12}}$ than $\frac{1}{\tau_{23}}$ and $\frac{1}{\tau_{24}}$. The phonon scattering rate $\frac{1}{\tau_{13}}$ also plays an important role in limiting the magnitude of gain and emission efficiency. However, in the four level design, the pump transition can be decoupled from the dominant parasitic LO phonon scattering channel.

The rate equations for the four level design are given by

$$\frac{d\rho_4}{dt} = \frac{1}{\tau_p}\rho_1 - (\frac{1}{\tau_{14}} + \frac{1}{\tau_{24}} + \frac{1}{\tau_{34}})\rho_4, \tag{2.37}$$

$$\frac{d\rho_3}{dt} = \frac{1}{\tau_{34}}\rho_4 - (\frac{1}{\tau_{13}} + \frac{1}{\tau_{23}})\rho_3, \tag{2.38}$$

$$\frac{d\rho_2}{dt} = \frac{1}{\tau_{24}}\rho_4 + \frac{1}{\tau_{23}}\rho_3 - \frac{1}{\tau_{12}}\rho_2, \tag{2.39}$$

$$\frac{d\rho_1}{dt} = -\frac{1}{\tau_p}\rho_1 + \frac{1}{\tau_{12}}\rho_2 + \frac{1}{\tau_{13}}\rho_3 + \frac{1}{\tau_{14}}\rho_4. \tag{2.40}$$

The population inversion between levels E_3 and E_2 in the four level system is obtained in steady state by setting $\frac{d}{dt} = 0$, resulting in

$$\rho_3 - \rho_2 = \left(\frac{\tau_3^{tot}}{\tau_{34}}(1 - \frac{\tau_{12}}{\tau_{23}}) - \frac{\tau_{12}}{\tau_{24}}\right)\frac{\tau_4^{tot}}{\tau_p}\rho_1, \tag{2.41}$$

where

$$\rho_1 = \frac{\rho_e}{\left(1 + \frac{\tau_4^{tot}}{\tau_p}(1 + \frac{\tau_3^{tot}}{\tau_{34}} + \frac{\tau_{12}}{\tau_{24}} + \frac{\tau_3^{tot}\tau_{12}}{\tau_{34}\tau_{23}})\right)}. \tag{2.42}$$

The spontaneous emission efficiency of the four level system is calculated similarly to the three level case,

$$\eta_{4L} = \sigma_{14}\rho_1\frac{\hbar\omega_{23}}{\hbar\omega_{14}}\frac{\tau_4^{tot}}{\tau_{34}}\frac{\tau_3^{tot}}{\tau_{23}^{spon}}. \tag{2.43}$$

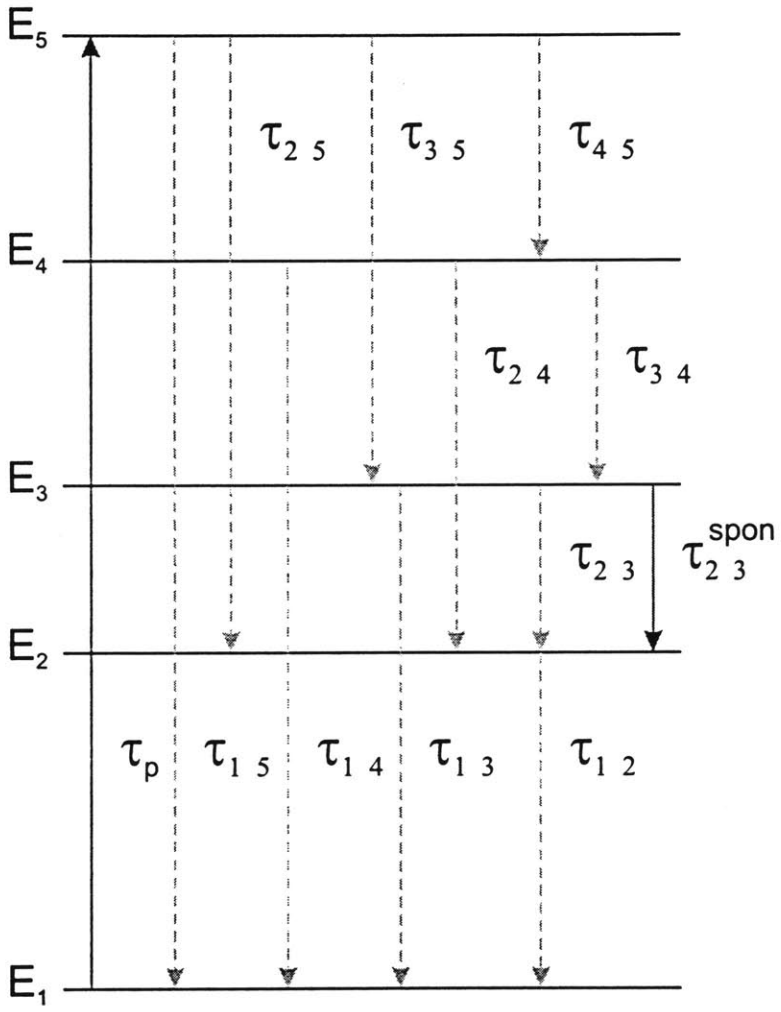

Figure 2-7: The five level system. Electrons are pumped from the ground state E_1 to E_5, followed by a fast relaxation to subband E_4 and E_3. Population inversion is created between subbands E_3 and E_2 by engineering a faster phonon scattering rate $\frac{1}{\tau_{12}}$ than $\frac{1}{\tau_{23}}$, $\frac{1}{\tau_{24}}$ and $\frac{1}{\tau_{25}}$. The phonon scattering rate $\frac{1}{\tau_{13}}$ also plays an important role in determining the magnitude of gain and emission efficiency.

2.4.3 Five Level System

Five level systems will be studied in Chapter 4 with the view of optimizing high temperature performance. Of particular interest will be the five level system shown in Figure 2-7. In the five level design electrons are pumped from the ground state E_1 to E_5, followed by a fast relaxation to subband E_4 and E_3. Population inversion is created between subbands E_3 and E_2 by engineering a faster phonon scattering rate $\frac{1}{\tau_{12}}$ than $\frac{1}{\tau_{23}}, \frac{1}{\tau_{24}}$ and $\frac{1}{\tau_{25}}$.

The rate equations for the five level design are given by

$$\frac{d\rho_5}{dt} = \frac{1}{\tau_p}\rho_1 - (\frac{1}{\tau_{15}} + \frac{1}{\tau_{25}} + \frac{1}{\tau_{35}} + \frac{1}{\tau_{45}})\rho_5, \tag{2.44}$$

$$\frac{d\rho_4}{dt} = \frac{1}{\tau_{45}}\rho_5 - (\frac{1}{\tau_{14}} + \frac{1}{\tau_{24}} + \frac{1}{\tau_{34}})\rho_4, \tag{2.45}$$

$$\frac{d\rho_3}{dt} = \frac{1}{\tau_{35}}\rho_5 + \frac{1}{\tau_{34}}\rho_4 - (\frac{1}{\tau_{13}} + \frac{1}{\tau_{23}})\rho_3, \tag{2.46}$$

$$\frac{d\rho_2}{dt} = \frac{1}{\tau_{25}}\rho_5 + \frac{1}{\tau_{24}}\rho_4 + \frac{1}{\tau_{23}}\rho_3 - \frac{1}{\tau_{12}}\rho_2, \tag{2.47}$$

$$\frac{d\rho_1}{dt} = -\frac{1}{\tau_p}\rho_1 + \frac{1}{\tau_{12}}\rho_2 + \frac{1}{\tau_{13}}\rho_3 + \frac{1}{\tau_{14}}\rho_4 + \frac{1}{\tau_{15}}\rho_5. \tag{2.48}$$

The population inversion between levels E_3 and E_2 in the five level system is obtained in steady state by setting $\frac{d}{dt} = 0$, resulting in

$$\rho_3 - \rho_2 = \left((\frac{\tau_3^{tot}}{\tau_{35}} + \frac{\tau_3^{tot}\tau_4^{tot}}{\tau_{34}\tau_{45}})(1 - \frac{\tau_{12}}{\tau_{23}}) - \frac{\tau_{12}}{\tau_{25}} - \frac{\tau_{12}\tau_4^{tot}}{\tau_{24}\tau_{45}}\right)\frac{\tau_5^{tot}}{\tau_p}\rho_1, \tag{2.49}$$

where

$$\rho_1 = \frac{\rho_e}{\left(1 + \frac{\tau_5^{tot}}{\tau_p}(1 + \frac{\tau_4^{tot}}{\tau_{45}} + \frac{\tau_3^{tot}}{\tau_{35}} + \frac{\tau_{12}}{\tau_{25}} + \frac{\tau_4^{tot}\tau_3^{tot}}{\tau_{45}\tau_{34}} + \frac{\tau_4^{tot}\tau_{12}}{\tau_{45}\tau_{24}} + \frac{\tau_3^{tot}\tau_{12}}{\tau_{35}\tau_{23}} + \frac{\tau_4^{tot}\tau_3^{tot}\tau_{12}}{\tau_{45}\tau_{34}\tau_{23}})\right)}. \tag{2.50}$$

The spontaneous emission efficiency of the five level system is calculated to be,

$$\eta_{5L} = \sigma_{15}\rho_1 \frac{\hbar\omega_{23}}{\hbar\omega_{15}}\left(\frac{\tau_5^{tot}}{\tau_{35}} + \frac{\tau_5^{tot}\tau_4^{tot}}{\tau_{34}\tau_{45}}\right)\frac{\tau_3^{tot}}{\tau_{23}^{spon}}. \tag{2.51}$$

Even though the formulas get much more complicated as we go to higher energy level schemes, there are several important factors that remain constant. The population inversion always contains the factor $1 - \frac{\tau_{12}}{\tau_{23}}$. This factor plays a crucial role in the temperature dependence of the laser as we shall see in Chapter 4. Saturation is always obtained when the pump rate becomes comparable to the total decay rate of the pump transitions, i.e. $\tau_p \sim \tau_j^{tot}$, where j= 3, 4, or 5 depending on the energy level scheme that is used. This saturation condition determines the maximum population inversion possible in our system. Note that the maximum population inversion can never exceed $\frac{\rho_e}{2}$. The emission efficiency is proportional to the spontaneous emission rate divided by the total nonradiative decay from the upper laser level $\frac{\tau_3^{tot}}{\tau_{23}^{spon}}$.

Although our discussion was aimed at elucidating the basic features of energy level schemes for optically pumped quantum well lasers, it is quite general. In particular, we showed how the nonradiative scattering rates limit the performance of any laser system. We conclude with the axiom that material systems with slower nonradiative scattering rates are generally more efficient and require lower pump power to achieve inversion.

Chapter 3

Quantum Well Laser Design

3.1 Introduction

Intersubband transitions in quantum wells hold excellent qualities for realizing a far infrared laser [29, 21]. Since quantum wells are artificially grown structures, the intersubband transition energies can be designed for far infrared frequencies. The wavefunctions, dipole moments and phonon scattering rates can be tailored by band gap engineering of multiple coupled or step quantum wells. The LO phonon resonance in GaAs at $\hbar\omega_{LO} = 36\,meV$ is particularly suitable for phonon engineering population inversion at far infrared frequencies $< 36\,meV$, where LO phonon scattering is suppressed [14, 51, 52]. In this chapter, we analyze the physics of far infrared quantum well lasers and spontaneous emitters. Our goal is to arrive at the best possible design to maximize population inversion, gain and spontaneous emission efficiency.

One may envision designing an optically pumped far infrared quantum well laser by "scaling" the successful mid infrared laser designs to longer wavelengths. The mid infrared quantum well laser designs employ simple three level energy schemes which are easily scaled to the far infrared. Following this logical approach, several researchers carried out optically pumped far infrared spontaneous emission experiments [53, 54]. Such measurements are crucial first steps in the development of a

laser because the strength of the emission or emission efficiency gives an indication of design performance. The emission spectrum also provides verification of the design emission frequency and linewidth. Unfortunately, a decisive measurement of far infrared spontaneous emission has proven to be problematic.

There are several experimental difficulties, like inherently low far infrared emission efficiency, low collection efficiency and sample heating, that may have contributed to the poor results. Another reason may be that previous designs have focused only on optimizing the gain [55, 56]. Although both gain and emission efficiency are proportional to the product of pump and emission transition cross sections, their dependence on the phonon scattering rates is very different. In this chapter, we propose and analyze a new four level quantum well design scheme. It is shown that the new design can be optimized using phonon engineering to enhance both the gain and emission efficiency by an order of magnitude over previous designs. Special emphasis is given to the discussion of emission efficiency because this concept is crucial for understanding the experimental results we present in Chapter 5.

3.2 Three Level Scheme

We first analyze the simple three level design to understand why previous researchers had difficulty in measuring optically pumped far infrared intersubband emission. Figure 3-1 shows a prototype $Al_{0.33}Ga_{0.67}As-GaAs$ coupled double quantum well structure in analogy with the mid infrared laser design [57]. The energy levels and wavefuntions are calculated numerically by solving Schrödinger and Poisson equations self consistently [39]. The wavefunction solutions are then used to calculate the integrals in the phonon scattering rate formulas. We assume low temperature ($\sim 4.2\,K$) operation to isolate the most important physics and to simplify calculations.

When a pump laser is tuned to the $E_1 \rightarrow E_3$ transition, electrons are excited from the ground state E_1 to level E_3. The steady state populations of levels E_1, E_2 and

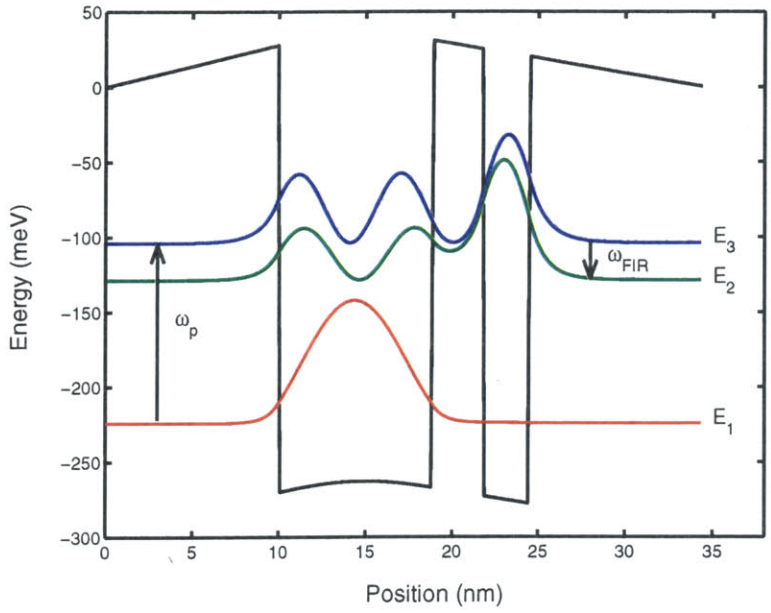

Figure 3-1: Double coupled quantum well structure for the three level design with a sheet electron density of $3 \times 10^{11}\, cm^{-2}$. The calculated transition energies are $\Delta E_{13} = 120.3\, meV$, $\Delta E_{12} = 95.5\, meV$ and $\Delta E_{23} = 24.8\, meV$. The calculated dipole matrix elements are $Z_{12} = 20.4\,$Å, $Z_{23} = 45.9\,$Å and $Z_{13} = 9.6\,$Å.

E_3 are determined by the fastest decay rates in the system. At low temperatures, LO phonon scattering leads to the fastest decay rate ($\sim 1\, ps$) for energy separations $> 36\, meV$ [15, 58]. Longitudinal acoustic (LA) phonon scattering gives the fastest decay rate ($\sim 100\, ps$) for far infrared transitions $< 36\, meV$ [59, 60]. The lasing transition $E_3 \rightarrow E_2$ is designed such that $E_3 - E_2 < 36\, meV$ to ensure a population inversion $\Delta\rho_{23} = (1 - \frac{\tau_{12}}{\tau_{23}})\rho_3$. The far infrared spontaneous emission efficiency of the three level design was derived in Chapter 2. The formula is repeated here for convenience

$$\eta_{3L} = \sigma_{13}\rho_1 \frac{\omega_{23}}{\omega_{13}} \frac{\tau_3^{tot}}{\tau_{23}^{spon}}\,, \tag{3.1}$$

where σ_{13} is the cross section for absorption of a pump photon by an electron making transitions from $E_1 \rightarrow E_3$, ρ_1 is the ground state sheet electron density, $\frac{1}{\tau_3^{tot}}$ is the total nonradiative decay rate from level E_3 and $\frac{1}{\tau_{23}^{spon}}$ is the spontaneous emission rate for the $E_3 \rightarrow E_2$ transition. We showed in Chapter 2 that spontaneous emission has

an ω_{23}^3 dependence. Thus, including the Manley-Rowe factor, the emission efficiency η_{3L} has an ω_{23}^4 dependence. Because of this unfavorable scaling factor, the far infrared emission efficiency is many orders of magnitude lower than in the mid infrared. For example, in the three level quantum well design of Figure 3-1, $\sigma_{13} = 1.0 \times 10^{-14}\, cm^2$, $\rho_1 = 3.0 \times 10^{11}\, cm^{-2}$, $\omega_{23}/\omega_{13} = 0.20$, $\tau_3^{tot} = 1.4\, ps$ and $\tau_{23}^{rad} = 2.4\, \mu s$, yielding a single well emission efficiency of 3.7×10^{-10}. In practice, the total efficiency is much lower because of poor far infrared collection efficiency [4].

It is difficult to see how one can improve η_{3L} by modifying the design of the three level system. Increasing the doping density to increase ρ_1 is not a good option because of free carrier absorption [57, 61]. Increasing the dipole matrix element Z_{13} to increase the pump absorption cross section σ_{13} means designing a stronger overlap between wavefunctions in levels E_1 and E_3. However, this also leads to a faster LO phonon scattering rate $\frac{1}{\tau_{13}}$. It is also problematic to improve the Manley-Rowe factor ω_{23}/ω_{13} since the CO_2 pump laser is only tunable in a narrow frequency range $\sim$ 110-135 meV.

3.3 Four Level Scheme

Here is where the power of the quantum well as an "artificial atom" comes to our rescue. With quantum wells we have the ability to design wavefunctions and phonon scattering rates. However, the simple three level scheme does not give us enough flexibility to take advantage of this power. We will now show that increasing the complexity of our design by going to a four level scheme will greatly improve our flexibility to design a larger emission efficiency [36, 62].

The prototype four level design is shown in Figure 3-2. This design employs three coupled quantum wells. The well widths basically determine the energy levels while the barrier widths determine the strength of the coupling between wavefunctions. Electrons are optically pumped from the ground state E_1 to E_4. $E_4 - E_3$ is separated

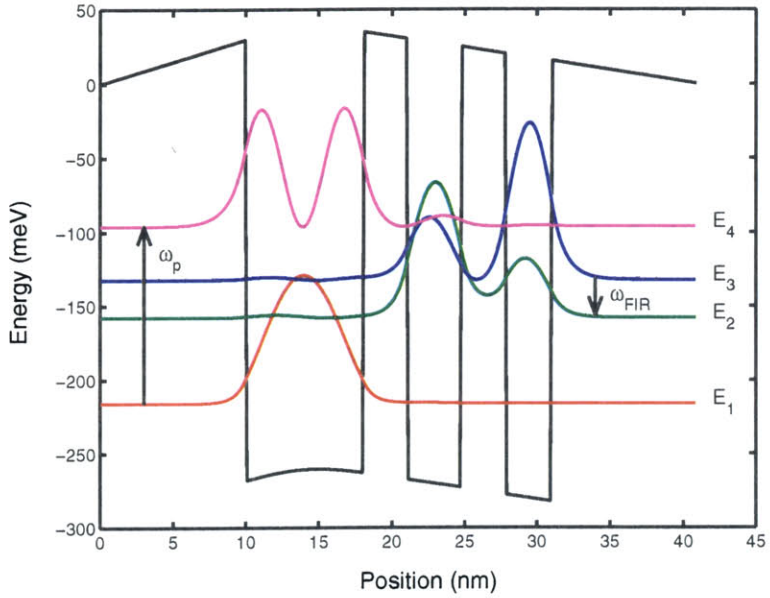

Figure 3-2: Triple coupled quantum well structure for the four level design with a sheet electron density of $3 \times 10^{11}\, cm^{-2}$. The calculated transition energies are $\Delta E_{14} = 119.8\, meV$, $\Delta E_{13} = 83.8\, meV$, $\Delta E_{12} = 58.2\, meV$ and $\Delta E_{23} = 25.6\, meV$. The calculated dipole matrix elements are $Z_{12} = 9.5\,$Å, $Z_{23} = 34.4\,$Å, $Z_{13} = 6.6\,$Å, $Z_{14} = 18.9\,$Å, $Z_{34} = 22.9\,$Å and $Z_{24} = 10.6\,$Å.

by approximately one LO phonon energy so that electrons quickly decay from E_4 to E_3. The laser emission occurs between levels E_3 and E_2 at $\hbar\omega_{32} \sim 25\,meV$. Electrons quickly decay from E_2 to the ground state because $E_2 - E_1 > 36\,meV$. The spontaneous emission efficiency for the four level design is given by

$$\eta_{4L} = \sigma_{14}\rho_1 \frac{\omega_{23}}{\omega_{14}} \frac{\tau_4^{tot}}{\tau_{34}} \frac{\tau_3^{tot}}{\tau_{23}^{rad}} \,. \tag{3.2}$$

At first sight it looks like this result is worse than the three level case because of the extra ratio $\frac{\tau_4^{tot}}{\tau_{34}}$. Actually it is this extra ratio that allows us to bypass a major deficiency of the three level design. We have designed the scattering rates such that $\frac{1}{\tau_{34}}$ is the dominant contribution to $\frac{1}{\tau_4^{tot}}$ so that $\frac{\tau_4^{tot}}{\tau_{34}} \sim 1$. Thus, the absorption of the pump $\sigma_{14}\rho_1$ is effectively decoupled from the LO phonon scattering rate $\frac{1}{\tau_3^{tot}}$. We can increase the dipole matrix element Z_{14} to increase $\sigma_{14} \propto Z_{14}^2$ without effecting $\frac{1}{\tau_3^{tot}}$. This gives us the extra flexibility to increase the emission efficiency over previous designs.

Figure 3-3 shows a calculation of emission efficiency as a function of electron density for the four level design in Figure 3-2. For comparison, we have also included the results for the three level design of Figure 3-1. The pump absorption cross section was calculated on resonance with a linewidth of $\Gamma = 6\,meV$. The four level scheme gives an order of magnitude improvement at the optimum electron density of $\rho_1 \sim 3.0 \times 10^{11}\,cm^{-2}$. We also observe a resonance effect as the electron density is varied and $E_4 - E_3$ gets close to the LO phonon energy. This shift in energy levels can be understood in the tight binding approximation since electrons in subband E_4 are localized in the same well as the ground state E_1 while electrons in E_3 are mostly localized in the rightmost well. Thus, increasing the ground state electron density will tend to lower E_3 with respect to E_1 much more than E_4. The emission efficiency of the three level scheme increases almost linearly with ρ_1 and starts to catch up with η_{4L} at higher electron densities. One can always design the optimum alignment

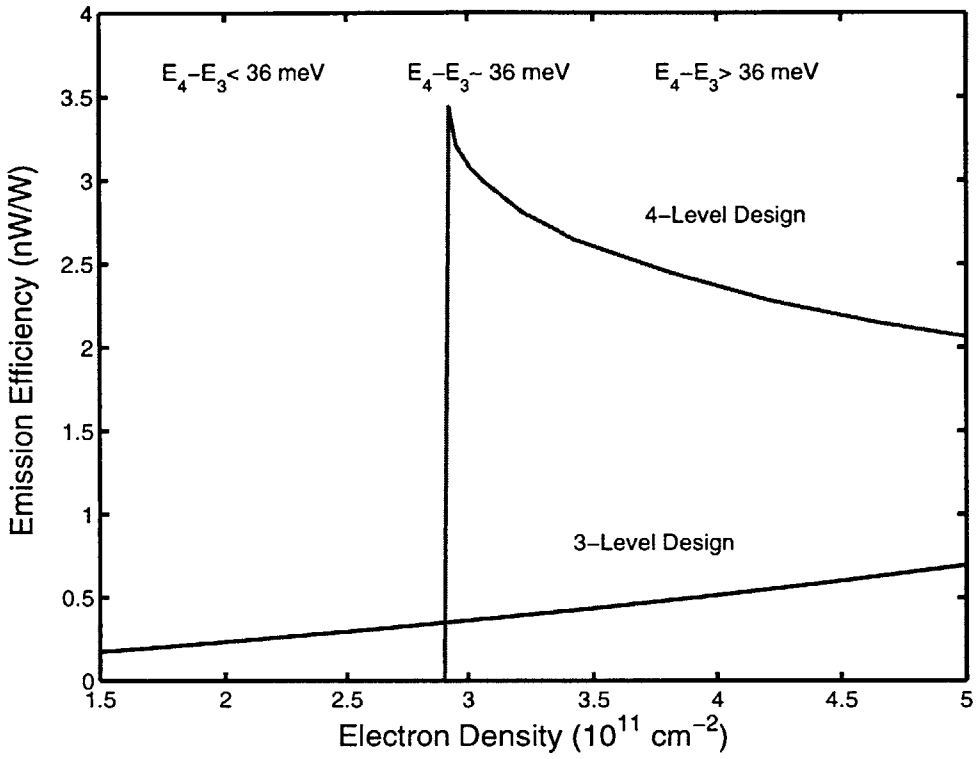

Figure 3-3: Comparison of emission efficiency for the three level and four level designs as a function of electron density in the ground state of the quantum wells. The peak in emission efficiency of the four level design is due to the optimal alignment of $E_4 - E_3 \sim 36\,meV$ at $\rho_1 \sim 3 \times 10^{11}\,cm^{-2}$.

of the four level system $E_4 - E_3 \sim 36\,meV$ to occur at higher electron densities to increase the peak population inversion. However, there is a trade off since free carrier absorption loss also increased with electron density $\propto \rho_e$ [57, 61].

The same physics that allows us to improve spontaneous emission also leads to larger population inversion and gain. The population inversion for the four level design is given by

$$\Delta\rho_{23} = \left(\frac{\tau_3^{tot}}{\tau_{34}}(1 - \frac{\tau_{12}}{\tau_{23}}) - \frac{\tau_{12}}{\tau_{24}}\right)\frac{\tau_4^{tot}}{\tau_p}\rho_1 \ , \tag{3.3}$$

where $\frac{1}{\tau_p} = \frac{\sigma_{14} I_p}{\hbar\omega_p}$ is the pump rate of electrons from $E_1 \rightarrow E_4$,

$$\rho_1 = \frac{\rho_e}{\left(1 + \frac{\tau_4^{tot}}{\tau_p}(1 + \frac{\tau_3^{tot}}{\tau_{34}} + \frac{\tau_{12}}{\tau_{24}} + \frac{\tau_3^{tot}\tau_{12}}{\tau_{34}\tau_{23}})\right)}. \tag{3.4}$$

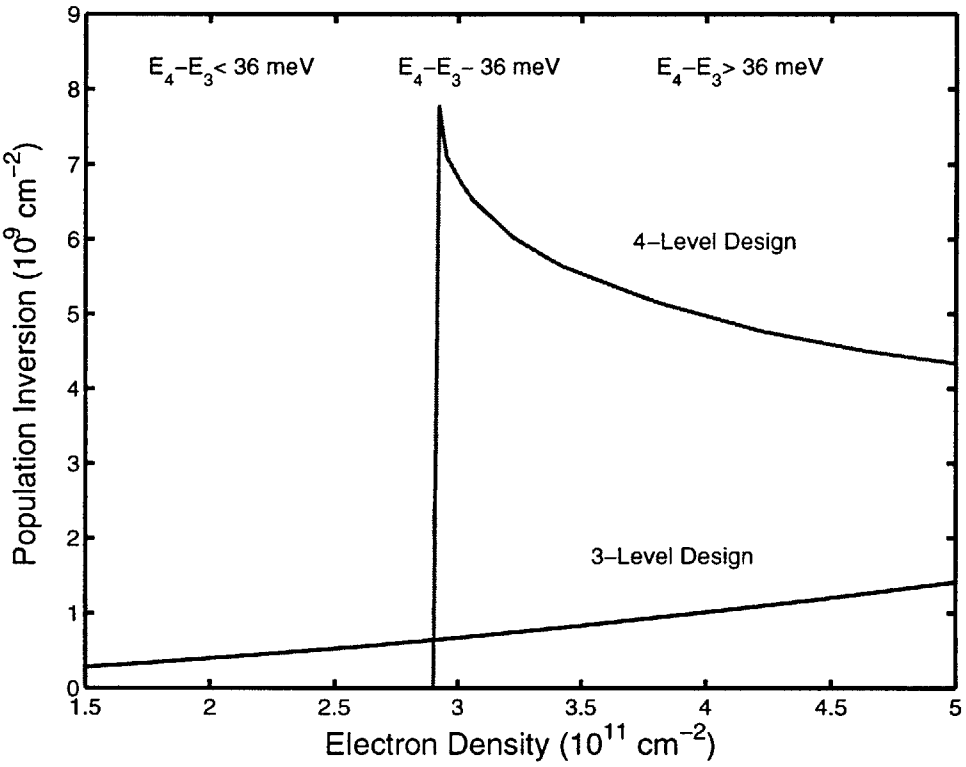

Figure 3-4: Comparison of population inversion for the three level and four level designs as a function of electron density in the ground state of the quantum wells. A pump intensity of $3.2\,kW\,cm^{-2}$ is assumed, corresponding to 1 Watt of pump power focused to a $200\,\mu m$ diameter spot. The peak in population inversion of the four level design is due to the optimal alignment of $E_4 - E_3 \sim 36\,meV$ at $\rho_1 \sim 3 \times 10^{11}\,cm^{-2}$.

and $\rho_e \sim 3 \times 10^{11}\, cm^{-2}$ is the total electron density in the quantum well. We designed the phonon scattering rates such that $\frac{\tau_3^{tot}}{\tau_{34}} \gg \frac{\tau_{12}}{\tau_{24}}$, $\frac{\tau_3^{tot}\tau_{12}}{\tau_{34}\tau_{23}}$ and $\frac{\tau_4^{tot}}{\tau_{34}} \sim 1$, so that $\Delta\rho_{23} \simeq \rho_1 \frac{\tau_3^{tot}}{\tau_p}$. Thus, as in the design of emission efficiency, τ_3^{tot} can be optimized independently from the pump absorption cross section. Figure 3-4 shows the calculated population inversion. A pump intensity of $I_p = 3.2\, kW\, cm^{-2}$ is assumed, corresponding to 1 Watt of pump power focused to a $200\, \mu m$ diameter spot. The population inversion of the four level design is an order of magnitude larger at the optimum electron density of $\rho_1 \sim 3.0 \times 10^{11}\, cm^{-2}$. The larger population inversion transfers directly to a larger gain.

3.4 Gain and Loss

Laser mode confinement is as critical as population inversion for achieving high gain. Confinement of long wavelength $\lambda \sim 30 - 300\, \mu m$ far infrared radiation is difficult using standard semiconductor diode laser waveguide technology. The confinement factor reflects the overlap of the laser mode with the active region

$$\gamma_{conf} = \frac{\int_{active} |E_z|^2 dz}{\int_{\infty}^{\infty} |E|^2 dz}. \tag{3.5}$$

In the shorter wavelength quantum cascade lasers, the index of refraction difference between the InGaAs active region and the InP substrate provides confinement for the laser mode. This method does not work in AlGaAs-GaAs material systems because the GaAs substrate has a higher index of refraction than AlGaAs. However, even in InGaAs-InP based material systems the index of refraction difference is too small to provide sufficient confinement in the far infrared. Growing multiple layer cladding regions to achieve confinement using Bragg reflectors is not practicable in the far infrared because of prohibitively long MBE growth.

Metallic confinement is probably the only feasible way to confine far infrared radiation [31]. Figure 3-5 shows the laser waveguide structure based on metallic

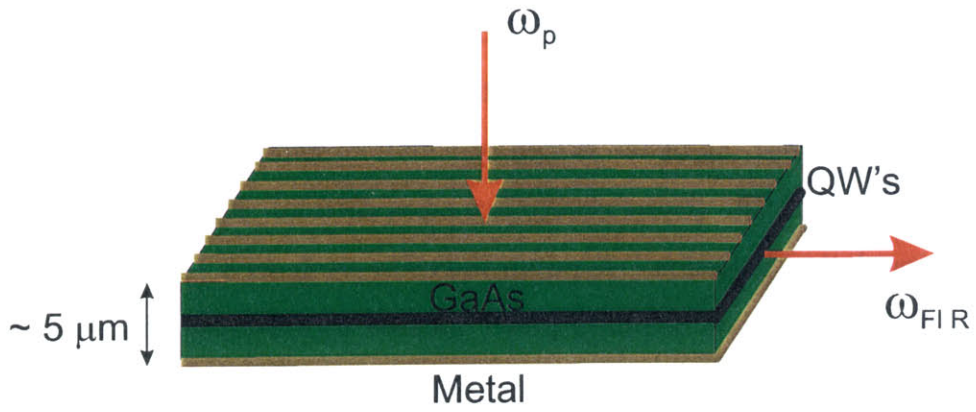

Figure 3-5: Optically pumped far infrared quantum well laser waveguide structure. The rectangular slab waveguide is covered by metal on the bottom surface and a grating on the top surface. The grating is used to couple the CO_2 pump laser to intersubband transitions in the quantum wells.

confinement. The rectangular slab waveguide is covered by metal on the bottom surface and a grating on the top surface. A slab waveguide is formed by selectively etching the substrate material, leaving only a thin $\sim 5\,\mu m$ active region. Metal is deposited on the bottom surface and a grating is fabricated on the top surface using conventional photo lithography and lift off process. The period of the grating is designed to couple the pump laser into the first order Bragg mode, i.e. $\Lambda = \frac{\lambda_p}{2n}$ [63]. This grating acts like a mirror for longer wavelength far infrared radiation. The active region is assumed to be composed of 100 quantum well periods separated by 200 Å barriers. Two buffer layers of 5000 Å separate the active region from the surface. The confinement factors for the three level and four level designs are calculated to be 0.326 and 0.412 respectively. The difference being due to a larger total well width in the four level design relative to barrier width.

The gain is proportional to the product of emission cross section, population inversion and confinement factor

$$g = \sigma_{23} \frac{\Delta \rho_{23}}{L} \gamma_{conf}, \tag{3.6}$$

Figure 3-6 shows the calculated gain corresponding to the population inversion of

Figure 3-4. The gain was calculated at the maximum of the Lorentzian lineshape assuming a 6 meV linewidth. The gain of the four level design is an order of magnitude larger than in the three level scheme at the optimum design point $E_4 - E_3 \sim 36\,meV$. Thus, four level designs are capable of achieving gains of $\sim 40\,cm^{-1}$ for pump powers of $\sim$ 1 Watt.

Much larger gains are possible in pulse mode by using a high peak power Q-switched CO_2 pump laser. We derived the condition for achieving maximum population inversion in Chapter 2. It is obtained when the pump power approaches saturation of the pump transition, i.e. $\tau_p \sim \tau_{14}$. Inserting this value of τ_p into equation 3.4, we get $\Delta\rho_{23} \sim \frac{n_e}{2}$ at saturation. The maximum population inversion can never exceed half of the total electron density in the quantum wells. The gain corresponding to the maximum population inversion available in our four level design is approximately $\sigma_{23}\gamma_{conf}\frac{n_e}{2L} \sim 740\,cm^{-1}$.

It is interesting to compare the projected gain with the total loss in the system. Since optically pumped lasers do not require highly doped ohmic contact regions, free carrier absorption losses are minimized. For the low electron densities we considered above, the free carrier absorption loss is given by [41]

$$\alpha_{fc} = (\frac{\hbar\omega_p}{\hbar\omega_{23}})^2 \frac{n}{c\tau}, \tag{3.7}$$

where $\hbar\omega_p \sim 10\,meV$ is the plasma frequency, $\hbar\omega_{23} \sim 25\,meV$ is the laser frequency, $\tau \sim 0.5\,ps$ is the fastest scattering time, and $\frac{c}{n}$ is the speed of light in GaAs. The plasma frequency is calculated using an average three dimensional electron density of $1.5 \times 10^{17}\,cm^{-3}$. Thus, free carrier absorption loss is estimated to be $\sim 40\,cm^{-1}$. Transverse optical (TO) phonon scattering loss is very small at low temperatures $\sim 1 - 5\,cm^{-1}$ [6]. The remaining loss is due to facet output coupling $\frac{ln(R)}{l}$, where R= 0.33 in GaAs. Assuming a waveguide length of 0.1 cm, we get an output coupling loss of $\sim 11\,cm^{-1}$. The total loss including free carrier absorption, TO phonon scattering,

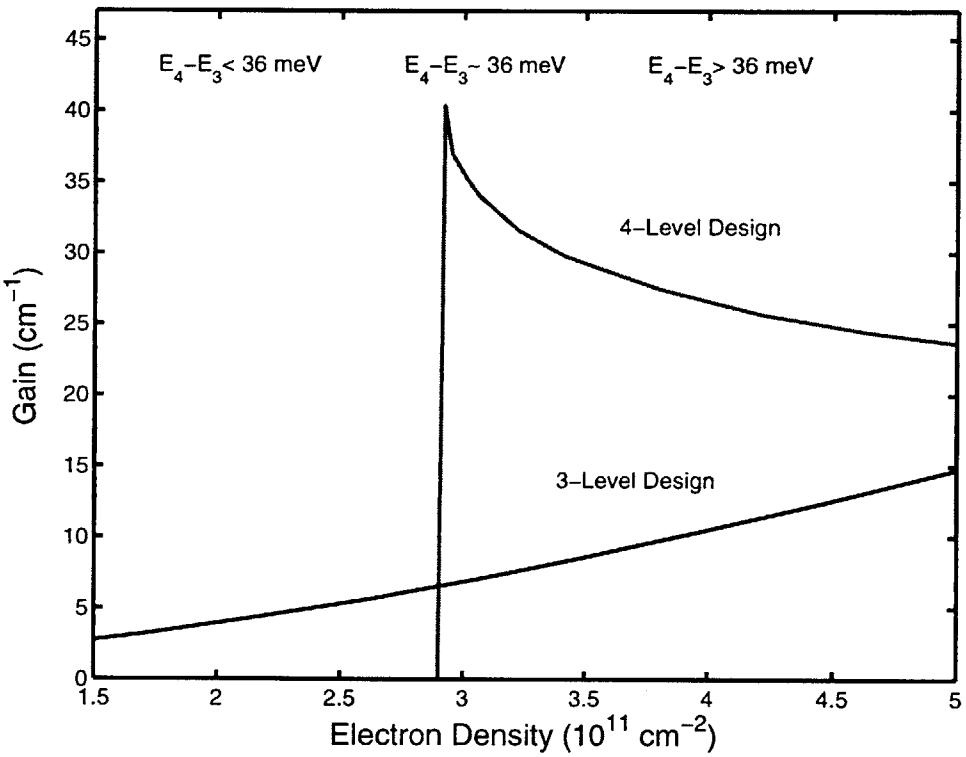

Figure 3-6: Comparison of gain for the three level and four level designs as a function of electron density in the ground state of the quantum wells. The gain is calculated using the population inversion of Figure 3-4. We assume a 6 meV linewidth for the $E_3 \rightarrow E_2$ transition.

and output coupling loss is thus estimated to be $\sim 50-60\,cm^{-1}$. It would be difficult to overcome this loss using a CO_2 pump laser in continuous wave mode because of heating effects [31]. However, a Q-switched CO_2 laser operates with very low average power (10-100 mW), while providing high peak power 300 nanosecond pulses. Thus, gains of $100\,cm^{-1}$ or more should be possible in pulse mode.

3.5 Concluding Remarks

We found that four level systems offer greater flexibility than three level systems to optimize the gain and emission efficiency of far infrared quantum well lasers. The power of quantum wells as "artificial atoms" is clearly evident in more complex design structures. One may wonder if there are additional advantages in going to an even more complex energy level scheme. In practice, the limited tunability of the CO_2 laser puts a constraint on the kind of energy level schemes we can employ. A five level scheme is as high as one can go assuming that all pairs of successive energy levels, except for the lasing transition, must be separated by at least one LO phonon energy.

Can a five level system offer any advantages over our four level design? Intuitively, the answer is no because extra energy levels will in general add extra phonon scattering paths which will lower the gain. However, it turns out that certain five level designs can be advantageous in improving the high temperature performance of far infrared quantum well lasers without lowering the peak gain too much. We will focus on the problem of temperature dependence in the next chapter.

Chapter 4

High Temperature Laser Design

4.1 Introduction

The performance of far infrared quantum well lasers is greatly influenced by temperature. Far infrared frequencies correspond roughly to the thermal energy kT at room temperature. At room temperature T= 300 K, the population inversion is blurred due to thermal filling of the upper laser level. But even before the temperature reaches 300 K, the gain and emission efficiency are greatly reduced because of increased phonon scattering.

Both LA and LO phonon scattering rates are proportional to $n_{ph} + 1$, where n_{ph} is the Bose-Einstein distribution function for phonons. The number of phonons n_{ph} gradually increases with temperature leading to an increase in the phonon scattering rate. This effect is especially noticeable in LA phonon scattering where the emitted phonons have very small energies $\hbar\omega \sim 1\,meV$. LO phonon scattering is not strongly effected by the temperature dependence of n_{ph} since $\hbar\omega_{LO} \sim 36\,meV$. However, LO phonon scattering suffers from a much worse temperature threshold phenomenon. This effect involves the opening of a parasitic LO phonon scattering window from the upper to lower laser levels.

Far infrared quantum well lasers are designed to take advantage of the LO phonon

resonance. The laser emission frequency is designed to be lower than the LO phonon energy to suppress LO phonon scattering. Meanwhile, the energy separation between the lower laser level and the ground state is designed to allow LO phonon scattering for efficient depopulation of the lower level. These ideal conditions for population inversion are violated when electrons in the upper laser level can gain enough thermal energy to scatter down to the lower level via fast LO phonon emission [64, 65]. The opening of this parasitic scattering channel has a devastating effect on the gain and emission efficiency. The design of far infrared quantum well lasers must take this parasitic LO phonon scattering channel into account since the local electron temperature can quite high even at cryogenic bath temperatures [31].

There are two ways to optimize the laser performance at high temperatures. One can either reduce the emission frequency to "shut" tighter the LO phonon window or try to enhance the scattering rate from the lower laser level to counteract the increased scattering from the upper level. Unfortunately, the limited tunability of the CO_2 pump laser puts a constraint on the quantum well design. For example in a three level design [55], the lasing transition is between $E_3 - E_2 \sim 25$ meV. Since the pump transition must be in the range $E_3 - E_1 \sim 120$ meV, the energy separation between the lower laser level E_2 and the ground state E_1 is much larger than the LO phonon energy of 36 meV. However, the fastest scattering rate between E_2 and E_1 occurs when this transition is exactly one LO phonon energy. In this case, the momentum of the emitted phonons is close to the Γ-point and the Frölich interaction Hamiltonian ($\propto 1/q$) is enhanced. A good idea for increasing the scattering rate from E_2 is to add an extra level exactly one LO phonon energy below E_2. Such a quasi three level design has been analyzed and shown to have improved high temperature performance [56]. However, we have demonstrated in the previous chapter that four level designs, where the pump transition occurs between $E_1 \rightarrow E_4$ and lasing between $E_3 \rightarrow E_2$, are superior by an order of magnitude in gain and emission efficiency over three level and quasi three level designs [36]. It would be advantageous to improve

the temperature dependence of the four level design without sacrificing its high peak gain.

In this chapter, we apply the two techniques mentioned above to improve the temperature performance of the four level design. First we consider the effect of lowering the emission frequency $E_3 - E_2$ so that the LO phonon window is opened at a higher temperature. This method works adequately for the gain because it scales only weakly with emission frequency ($\propto \omega_{23}$). The emission efficiency decreases much faster with frequency ($\propto \omega_{23}^4$). Therefore, scaling the emission frequency to lower energy does not improve the temperature dependence of emission efficiency. The best way to counteract the opening of the fast LO phonon channel at high temperatures is to enhance the scattering rate between the lower lasing level E_2 and the ground state E_1. To achieve this, we propose a five level design scheme where the energy separation $E_2 - E_1$ can be set at exactly one LO phonon resonance. The five level design maintains the high peak gain of the four level design while greatly improving its high temperature performance.

4.2 Phonon Scattering at High Temperatures

In the next two sections we analyze the temperature dependence of the four level design. It is particularly interesting to see how scaling the emission frequency effects the temperature dependence of gain and emission efficiency. Figure 4-1 shows the relevant phonon scattering paths at high temperatures. The electron Fermi-Dirac distributions are also shown schematically in red.

Optical pumping with the CO_2 laser establishes steady state electron populations in each subband. Assuming that Fermi-Dirac statistics are still valid, we can describe the subband populations by quasi Fermi levels. This assumption is similar to that used in conventional semiconductor diode lasers, where separate quasi Fermi levels for electrons and holes are assumed even in the active region [35]. The justification

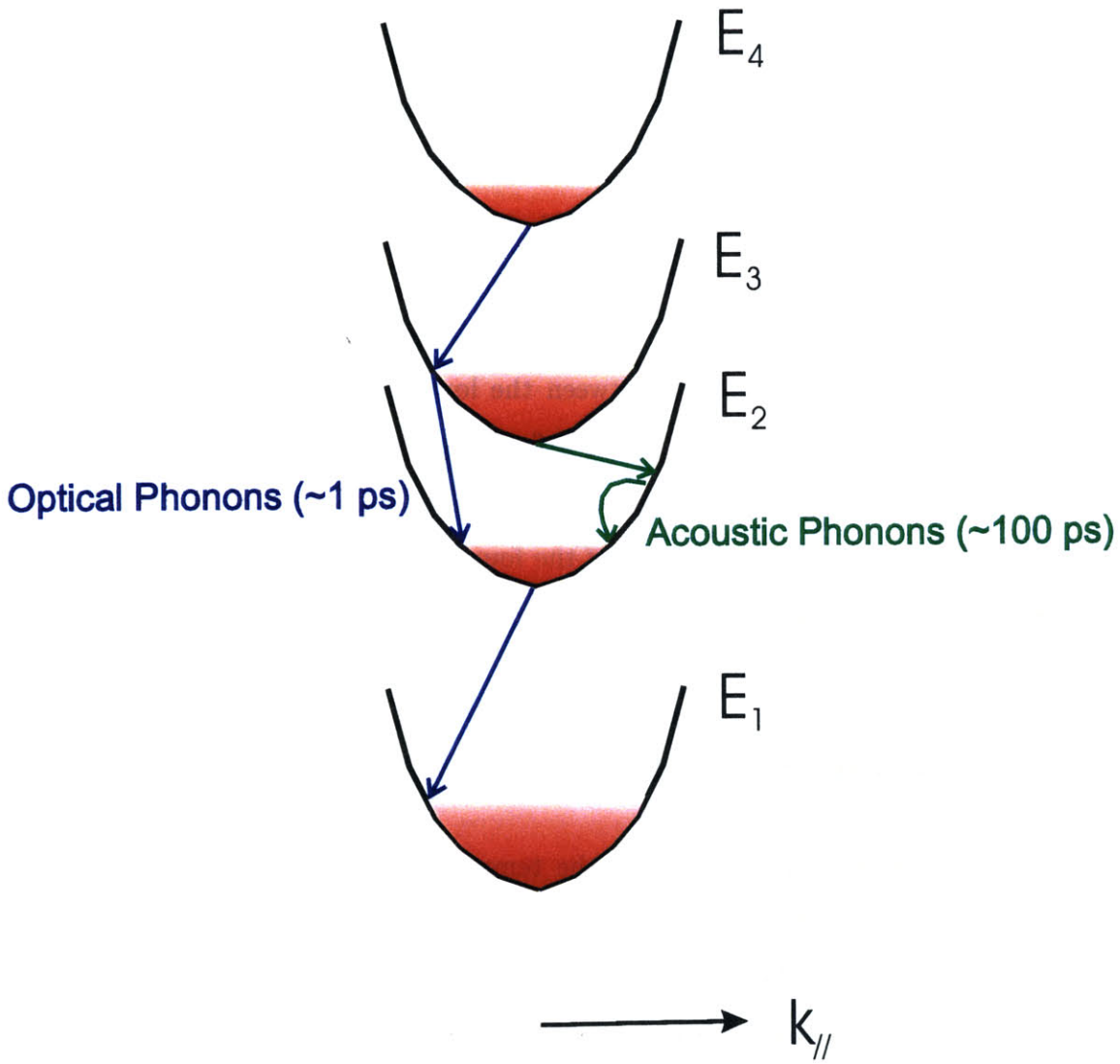

Figure 4-1: A schematic diagram showing the phonon scattering paths and electron distributions in the four level design at high temperatures.

in the case of diode lasers comes from the fact that electron-hole recombination times ($\sim$ 1 ns) are much longer than electron-electron scattering times in the conduction and valence bands. Energy exchange in a quantum well subband is also dominated by electron-electron scattering with $\sim$ 100 fs time scales [66]. Thus, since intersubband energy relaxation takes place via phonon scattering with $\sim$ 1 ps time scales, we can reasonably assume that electrons in each subband reach a quasi equilibrium state at some electron temperature T_e. The electron temperature may be higher than the lattice temperature since electron-phonon energy exchange occurs on a slower time scale.

At high electron temperatures, we can no longer make the simplification as was done in Chapters 2 and 3, that electrons only occupy states close to the bottom of the subbands. Some electrons will be "hot", meaning that they occupy states many meV above the subband bottom. In Chapter 2 we derived the formalism for calculating the single electron-phonon scattering rate $W_{i\to f}$ from some initial state (usually taken as $k_i = 0$) to all the possible final states in an empty subband E_f. Now we must take into account the thermal distribution of electron populations in the upper and lower subbands. This is done by averaging the scattering rate for all the electrons in the upper subband. The single electron scattering rates $W_{i\to f}$ are weighted by a Fermi-Dirac distribution and averaged over all initial states [65]

$$\frac{1}{\tau_{if}} = \frac{\int W_{i\to f}(E)F_i(E)(1 - F_f(E - \hbar\omega))dE}{\int F_i(E)dE}, \tag{4.1}$$

where the integration is from the bottom of subband E_i to the top of the quantum well. Equation 4.1 includes both hot electron and state blocking effects. However, state blocking effects are negligible for the small $\sim 10^{10}\, cm^{-2}$ excited subband populations we consider.

4.3 Scaling the Emission Frequency

The energy levels and wave functions for the four level design are shown in Figure 3-2. Note that it is easy to vary the emission frequency $E_3 - E_2$, without effecting the other parameters much, by adjusting the second barrier from the left. Figure 4-2 shows the calculation of emission efficiency as a function of temperature for different values of $E_3 - E_2$. The electron density was set at $3 \times 10^{11}\, cm^{-2}$ and the well widths adjusted slightly to ensure the optimum alignment $E_4 - E_3 \sim 36\, meV$ for each curve. The temperature dependence comes in through

$$\frac{1}{\tau_3^{tot}} = \frac{1}{\tau_{13}} + \frac{1}{\tau_{23}}. \tag{4.2}$$

At low temperatures $\frac{1}{\tau_{23}}$ is mainly due to slow acoustic phonon scattering. However, as the temperature increases, electrons in E_3 can get enough thermal energy to scatter down to E_2 via fast LO phonon emission. As soon as this parasitic scattering channel is opened, the emission efficiency drops rapidly. Note that scaling the emission frequency to lower energies does not improve the temperature dependence of emission efficiency because of its strong ($\propto \omega_{23}^4$) frequency dependence.

Figure 4-3 shows the calculated gain for the four level design as a function of temperature. We assume the same values of pump power, spot size, linewidth and confinement factor as in chapter 2. The temperature dependence of gain is dominated by the factor $(1 - \frac{\tau_{12}}{\tau_{23}})$. At low temperatures the ratio $\frac{\tau_{12}}{\tau_{23}}$ is negligible compared to 1 and it is not necessary to optimize the LO phonon scattering rate $\frac{1}{\tau_{12}}$. However, when the LO phonon scattering window is opened for $\frac{1}{\tau_{23}}$ at high temperatures, $\frac{1}{\tau_{23}}$ can become faster than $\frac{1}{\tau_{12}}$ giving rise to a negative gain. Figure 4-3 shows that scaling the emission frequency to lower energies does improve the high temperature dependence of gain. The peak gain is only decreased slightly by this scaling because of its weak ($\propto \omega_{23}$) frequency dependence. However, a better way to offset the increased scattering rate $\frac{1}{\tau_{23}}$ at high temperatures is by designing a faster $\frac{1}{\tau_{12}}$. We can

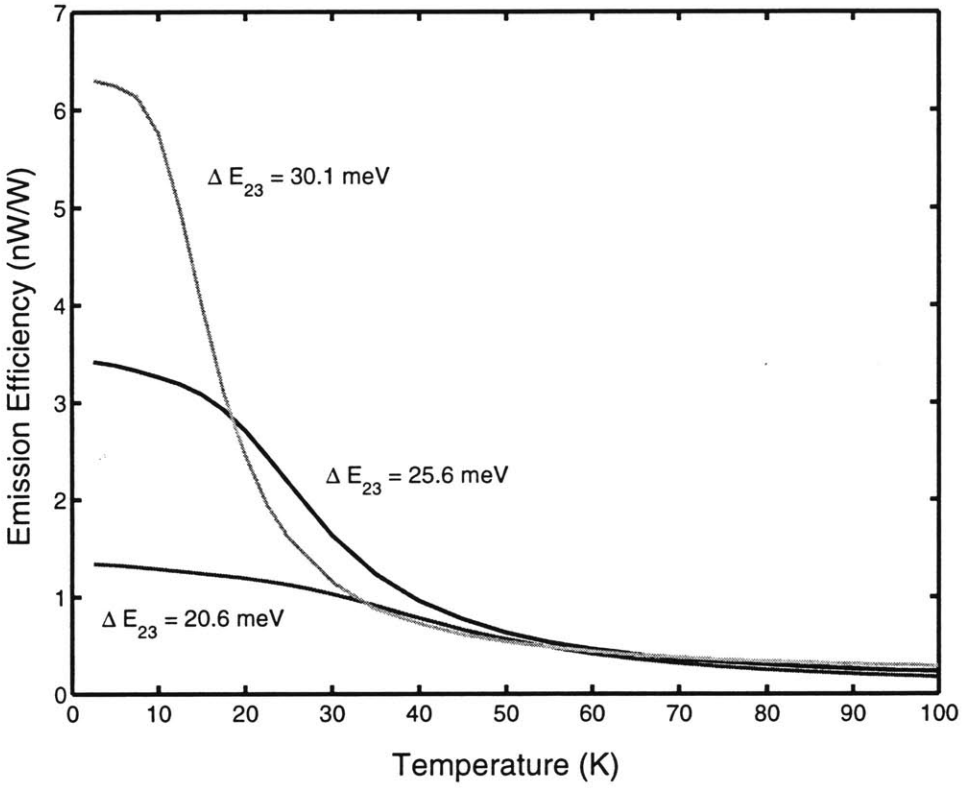

Figure 4-2: Calculation of emission efficiency for the four level design as a function of temperature and ΔE_{23}. Emission efficiency is not improved by scaling the emission frequency to lower energies. The reason lies in the unfavorable scaling of emission efficiency with frequency $\propto (\Delta E_{23})^4$.

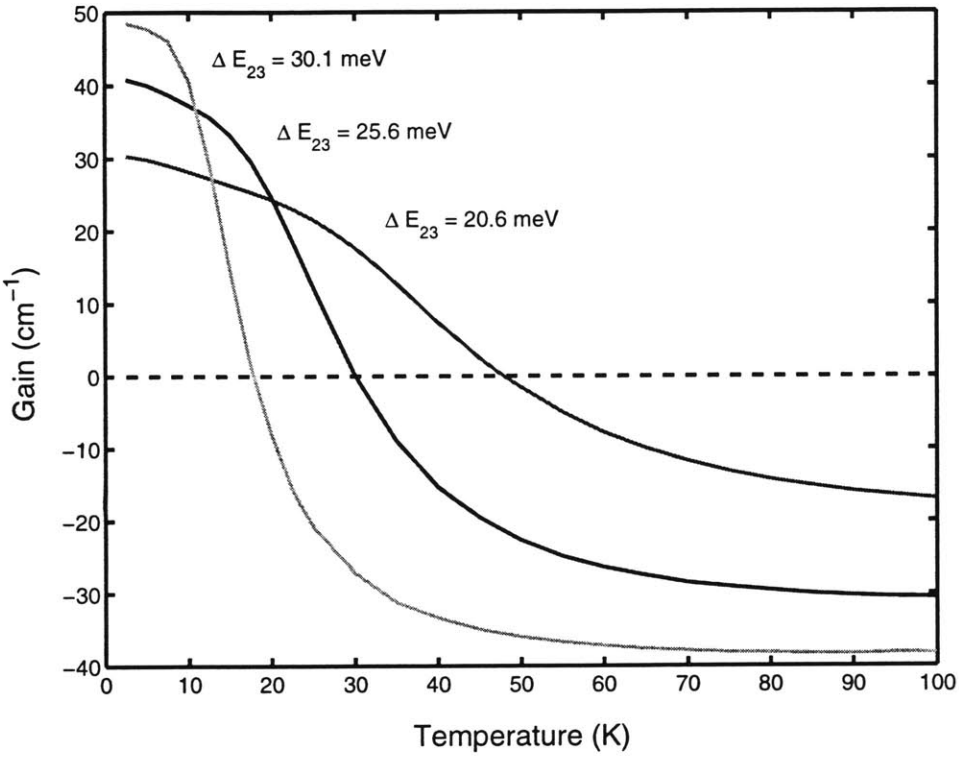

Figure 4-3: Calculation of gain for the four level design as a function of temperature and ΔE_{23}. The temperature dependence of gain is definitely improved by scaling to lower emission frequencies. The peak gain only drops as $\propto \Delta E_{23}$ in contrast to emission efficiency.

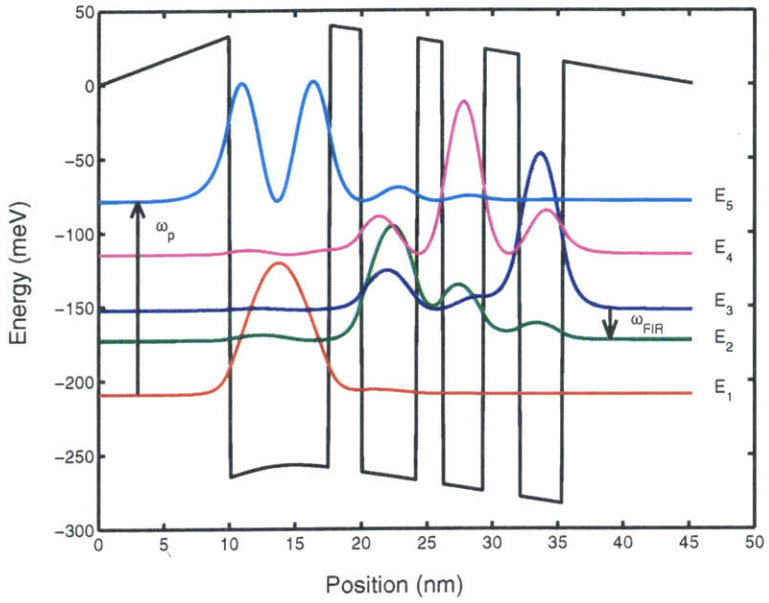

Figure 4-4: Quadruple coupled quantum well structure for the five level design. The electron density in the ground state is $\rho_1 = 3 \times 10^{11}\, cm^{-2}$. The calculated transition energies are $\Delta E_{15} = 130.4\, meV$, $\Delta E_{14} = 94.3\, meV$, $\Delta E_{13} = 57.0\, meV$, $\Delta E_{12} = 36.5\, meV$ and $\Delta E_{32} = 20.5\, meV$. The calculated dipole matrix elements are $Z_{12} = 15.6$ Å, $Z_{23} = 39.2$ Å, $Z_{13} = 5.8$ Å, $Z_{14} = 5.9$ Å, $Z_{34} = 37.6$ Å, $Z_{24} = 14.0$ Å, $Z_{15} = 17.0$ Å, $Z_{25} = 9.0$ Å, $Z_{35} = 6.1$ Å and $Z_{45} = 30.0$ Å.

accomplish this by using a five level quantum well design.

4.4 Five Level Design for Enhancing $\frac{1}{\tau_{12}}$

Figure 4-4 shows the energy levels and wavefunctions of our prototype five level design. Electrons are pumped from the ground state E_1 to E_5. From E_5 electrons quickly scatter down to E_3 via resonant two LO phonon emission. The laser emission occurs between E_3 and E_2. This design is similar to the four level case *except* for one crucial difference. The scattering rate from E_2 is a factor of 5 faster because the five level design makes it possible to set the optimum energy separation $E_2 - E_1 = 36$ meV.

The population inversion in the five level design is given by

$$\Delta n_{23} = \left((\frac{\tau_3^{tot}}{\tau_{35}} + \frac{\tau_3^{tot}\tau_4^{tot}}{\tau_{34}\tau_{45}})(1 - \frac{\tau_{12}}{\tau_{23}}) - \frac{\tau_{12}}{\tau_{25}} - \frac{\tau_{12}\tau_4^{tot}}{\tau_{24}\tau_{45}} \right) \frac{\tau_5^{tot}}{\tau_p} \rho_1 \ , \tag{4.3}$$

where the definitions of scattering rates are similar to the previous chapter. As in the four level case, the temperature dependence is dominated by the factor $(1 - \frac{\tau_{12}}{\tau_{23}})$ Figure 4-5 shows the temperature dependence of the gain in comparison to the four level design. The five level design has positive gain beyond 100 K while the four level design cuts off at about 50 K. Note also that the peak gain of the five level design is not diminished much by the extra scattering path from $E_4 \rightarrow E_2$.

The single well spontaneous emission efficiency of the five level design is given by

$$\eta_{5L} = \sigma_{15}\rho_1 \frac{\omega_{23}}{\omega_{15}} (\frac{\tau_5^{tot}}{\tau_{35}} + \frac{\tau_4^{tot}\tau_5^{tot}}{\tau_{34}\tau_{45}}) \frac{\tau_3^{tot}}{\tau_{23}^{rad}} \ . \tag{4.4}$$

As in the four level case, the temperature dependence of emission efficiency is dominated by $\frac{1}{\tau_3^{tot}}$. Figure 4-6 shows a calculation of emission efficiency as a function of temperature for the five level and four level designs. There is no advantage in this case for going to a five level design since $\frac{1}{\tau_3^{tot}}$ is not effected by enhancing $\frac{1}{\tau_{12}}$. Once the LO phonon window is opened for $\frac{1}{\tau_{23}}$, there is nothing one can do to prevent the rapid drop in spontaneous emission power. Therefore, the best strategy for designing spontaneous emission devices is to maximize the peak emission efficiency, which means using four level designs.

4.5 Concluding Remarks

We have analyzed the temperature dependence of optically pumped far infrared quantum well lasers. It was found that scaling the emission frequency to lower energies does benefit the high temperature performance, although at the expense of losing peak gain and design flexibility. The best way for improving high temperature performance

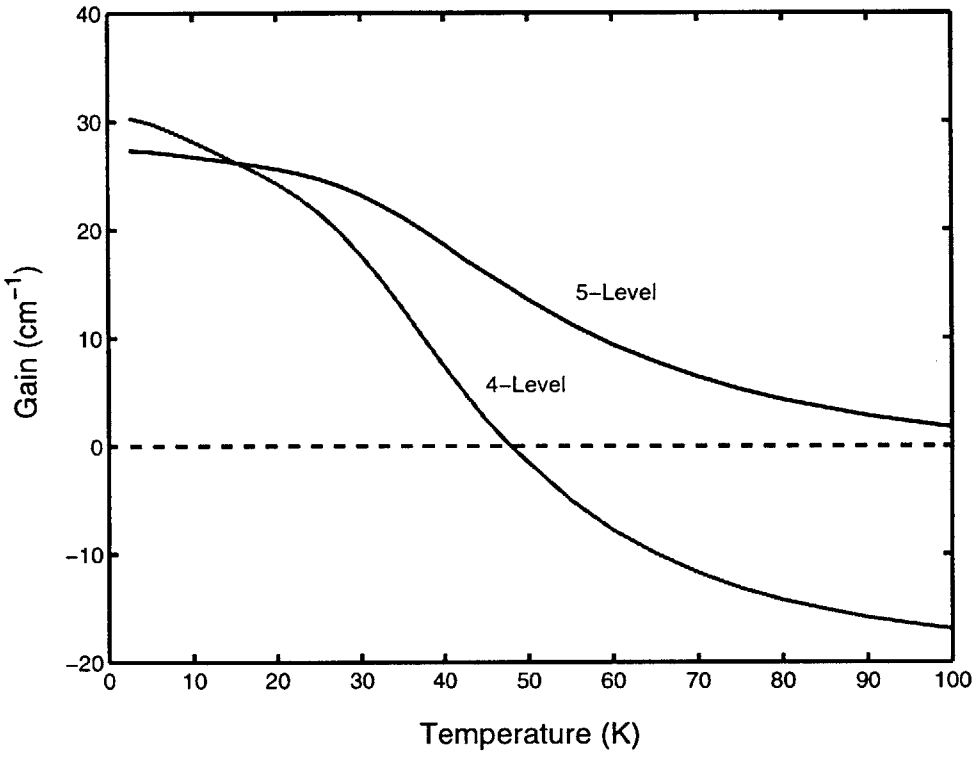

Figure 4-5: Comparison of gain for the four level and five level designs as a function of temperature. $\Delta E_{23} \sim 20\,meV$ and $\rho_1 = 3 \times 10^{11}\,cm^{-2}$ for both designs. The superior temperature dependence of the five level design comes from an enhanced LO phonon scattering rate for emptying the lower laser level.

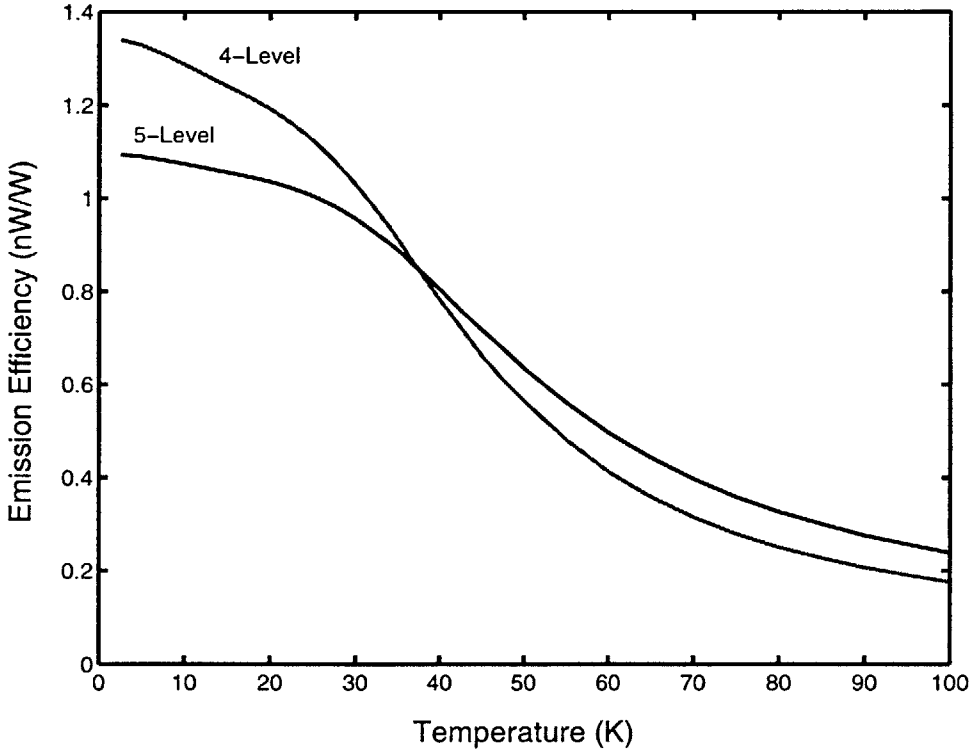

Figure 4-6: Comparison of emission efficiency for the four level and five level designs as a function of temperature. $\Delta E_{23} \sim 20\,meV$ and $\rho_1 = 3 \times 10^{11}\,cm^{-2}$ for both designs. The emission efficiency of the five level design is not affected by enhancing the LO phonon scattering rate from the lower laser level.

is to enhance the depopulation scattering rate of the lower laser level. We proposed a new five level design scheme that greatly improves the temperature performance without sacrificing peak gain. The emission efficiency is optimized by maximizing the peak emission efficiency at low temperatures. Therefore, four level designs are the best choice for spontaneous emission devices.

The five level design scheme we proposed may not be the last word on the "best" design. We chose to use coupled multiple quantum well structures as our design medium because such structures are easiest to grow by molecular beam epitaxy. However, there may exist more complicated design structures involving combinations of wells and steps that offer opportunities to improve on our work. In particular, further enhancement of the scattering rate $\frac{1}{\tau_{12}}$ may be possible by designing a structure similar to our five level design but with a stronger overlap between the wavefunctions in E_2 and E_1.

A more radical approach for improving the temperature performance would be to grow quantum well structures using the SiGe-Si material based system. The fact that Si is an indirect semiconductor is of no importance for intersubband transitions in quantum wells. The great advantage of Si over GaAs is the complete absence of polar LO phonon scattering in Si due to its nonpolar crystal structure. However, the technology for growing SiGe-Si heterostructures is still far behind GaAs based systems.

Chapter 5

Spontaneous Emission Experiments

5.1 Introduction

A measurement of spontaneous emission is always the most important first step in realizing a laser [67, 31]. The spontaneous emission data contains valuable information about the emission frequency, linewidth, and emission efficiency. The far infrared emission spectrum together with mid-infrared absorbance data provides an experimental verification of the energy levels in the quantum wells [29]. A measurement of absolute emission power versus pump power gives the emission efficiency. The emission efficiency depends on many of the same factors as the gain. Therefore a comparison of measured and calculated emission efficiencies gives a good indication of device performance. Finally, successful resolution of the far infrared emission linewidth allows an estimation of the highest gain available from the device.

The measurement of far infrared spontaneous emission from optically pumped quantum wells is challenging because of inherently weak emission efficiency. Several researchers have already tried without much success to measure optically pumped far infrared spontaneous emission from three level quantum well designs [53, 4, 54]. A major recent contribution to this effort was the development of four level quantum well designs with much higher emission efficiencies. The use of four level quantum well

designs gave us the advantage to produce superior experimental results over previous work.

In this chapter we describe our experiments to measure far infrared intersubband spontaneous emission and mid-infrared absorbance from three level and four level quantum well designs. These measurements confirm our quantum mechanical calculations of intersubband transition energies, dipole matrix elements, and the relative strength of the three level versus four level designs. The measurements on the four level design give the clearest demonstration to date of optically pumped far infrared spontaneous emission from quantum wells.

5.2 Absorbance Experiment Setup

Mid infrared absorbance measurements provide an indispensable tool to measure the energy levels and dipole moments of intersubband transitions in quantum wells. This data is especially important since the intersubband transition energy corresponding to the CO_2 pump laser is in the mid-infrared. Moreover, the measured values can be compared with the calculated values from our quantum mechanical computer simulation to verify the design. The absorbance experiments were carried out using a Nicolet Fourier Transform Infrared Spectrometer (FTIR). Figure 5-1 shows the optical layout of our FTIR modified for absorbance spectroscopy.

The heart of an FTIR is a Michelson interferometer. One of the mirrors in the interferometer is swept at a constant velocity in the linear scan mode or moved in discrete steps in the step scan mode. Linear scanning is convenient to use for absorbance measurements where a bright source is available. The light from a black body source passes through the interferometer where it is modulated by a moving mirror. After traversing the interferometer, the light passes through the sample compartment. The sample compartment was modified with additional optics to allow for coupling through 0.5 mm thick samples. The broad spectrum of the black body

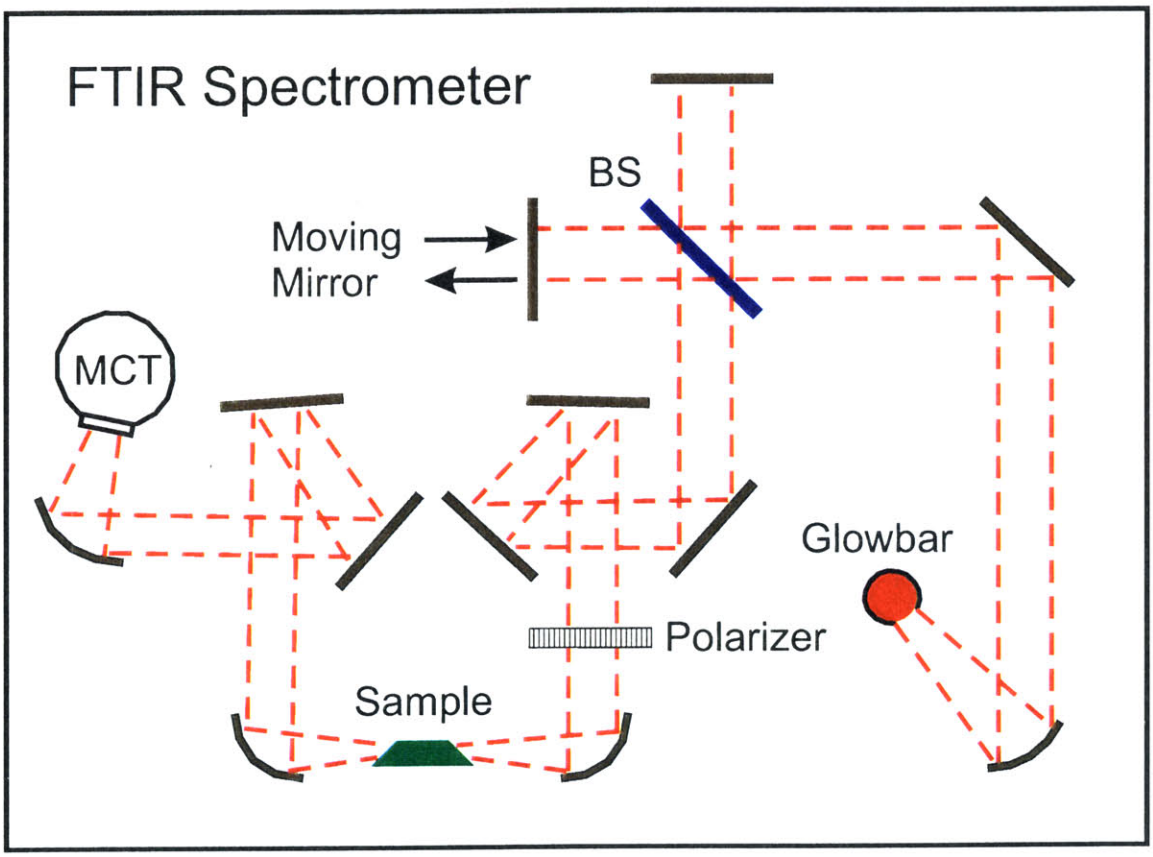

Figure 5-1: Experimental setup for mid-infrared absorbance measurements.

source is altered by the sample due to intersubband absorption. After going through the sample compartment optics, the light is focused onto a Mercury Cadmium Telluride (MCT) liquid Nitrogen cooled detector. The modulation of the source radiation due to the moving mirror in the interferometer produces an interferogram at the detector. A Fourier transform of the interferogram gives the spectrum of the light that has passed through the sample.

We used a polarizer to ratio the spectra for light in the growth direction of the quantum wells versus light in the plane of the layers. This ratio procedure removes most of the substrate free carrier absorption components from the spectrum. The logarithm of the transmission ratios $Log(T_{\|}/T_{\perp})$ gives the absorbance, which is proportional to the absorption loss [32]

$$\alpha = \frac{1}{L_{int}} ln(10) Log_{10}(\frac{T_{\|}}{T_{\perp}}). \tag{5.1}$$

L_{int} is the total interaction length in the quantum wells defined as

$$L_{int} = \frac{L_W N_W N_p}{cos\theta}, \tag{5.2}$$

where L_W is the total quantum well thickness, N_W the number of quantum well periods, N_p the number of passes, and θ the angle of incidence with respect to the normal to the plane of the layers.

Peaks in the absorbance correspond to intersubband transition energies $E_j - E_1$ in the quantum wells. The area under a particular peak j multiplied by ln(10) is called the absorption strength I_{1j}. The absorption strength can be calculated by integrating the theoretical (Lorentzian) absorption formula over energy

$$I_{1j} = \frac{2\pi^2 \rho_s N_W N_p \nu e}{\epsilon_o c n} Z_{1j}^2 \frac{sin^2\theta}{cos\theta}, \tag{5.3}$$

where ρ_s is the sheet electron density in the wells, n is the index of refraction, ν is

the peak frequency of the intersubband transition, and c is the velocity of light in vacuum. The calculated absorption strength depends on two unknown experimental parameters ρ_s and Z_{1j}. Thus from the measured absorption strength and knowledge of ρ_s we can deduce the dipole matrix element Z_{1j}. The samples were processed into a 3 bounce trapezoid waveguide (N_p= 6) by cleaving a bar and polishing two opposite ends at a 45 degree angle ($\theta = 57$). The same waveguide structure was used for both emission and transmission measurements.

5.3 Emission Experiment Setup

The emission measurements were done using the FTIR in step scan mode. Step scan mode is necessary when lock-in detection is used to measure very weak emission signals [68]. Lock-in detection involves external modulation or chopping to produce a reference signal. This additional modulation frequency can interfere with the internal modulation of the moving mirror in linear scanning. However, in step scanning the mirror moves in discrete steps. At each step the mirror comes to a complete stop. Once the mirror is stopped the source radiation is no longer modulated by the motion. The time delay at each stop can be adjusted to accommodate the integration time of lock-in detection to increase the signal to noise ratio.

The experimental setup for the emission measurements is shown in Figure 5-2. The sample is mounted in a Janus liquid Helium cryostat. A CO_2 pump laser is focused onto the 45 degree angle facet of the waveguide using an f=5 inch ZnSe lens. We estimate the diffraction limited spot size to be about 150-200 μm. ZnSe was also used for the pump input windows to the sample compartment of the cryostat. The pump laser is electrically chopped at 500 Hz for lock-in detection. The far infrared spontaneous emission is collected from a cleaved side of the sample so as not to contaminate it with the CO_2 laser radiation. A specially designed cone optic collects the far infrared radiation and directs it through the output windows. Single crystal

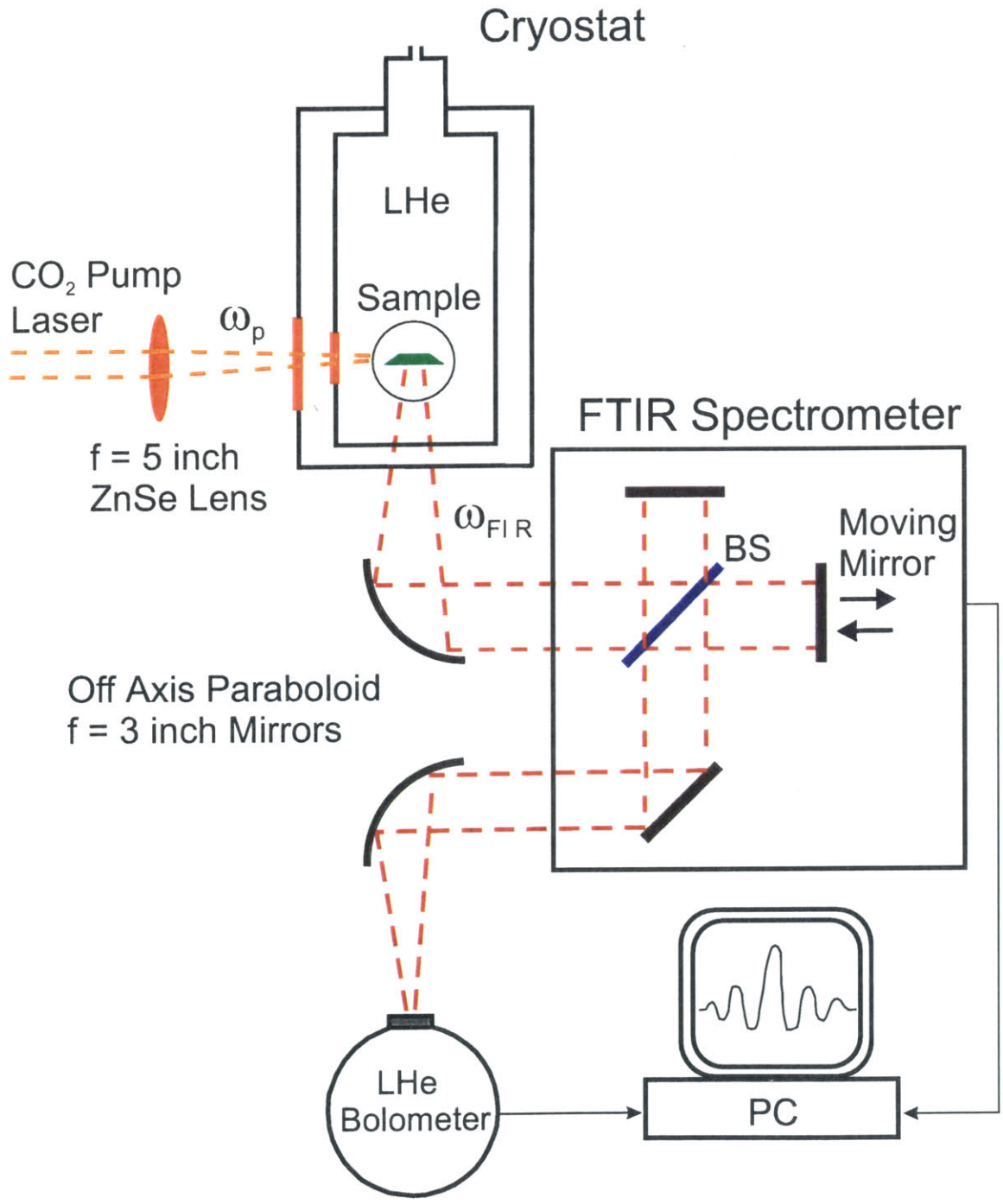

Figure 5-2: Experimental setup for far infrared emission measurements.

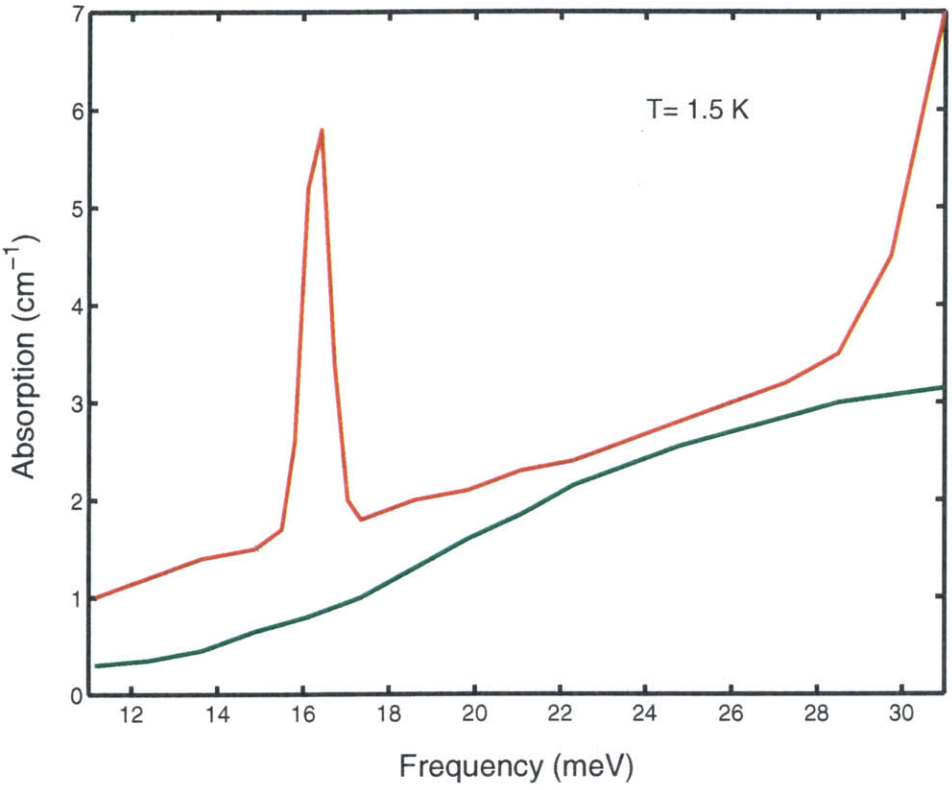

Figure 5-3: Far infrared absorption of quartz (in red) and sapphire (in green). The quartz data is for ordinary wave, applicable to Z-cut crystal. The sapphire data is an average of ordinary and extraordinary waves, applicable to random oriented crystal.

quartz was used for the cold inner window during experiments on the three level design. This window material was later changed to single crystal sapphire for improved far infrared absorption properties at liquid Helium temperatures. Polypropylene was used for the outer vacuum window. A gold coated off-axis paraboloid mirror with f=3 inches collects and redirects the far infrared radiation into the FTIR. After propagating through the interferometer, the output radiation is focused onto an Infrared Laboratories liquid Helium Si bolometer using a second similar off-axis paraboloid mirror. The output signal from the bolometer goes to a lock-in amplifier and then to a PC for processing.

The far infrared optical collection efficiency η_{opt} is an important figure of merit for our experimental setup. It is also essential to have an estimate for η_{opt} to extract

the far infrared emission efficiency from a measurement of absolute emission power. The collection efficiency can be estimated as follows

$$\eta_{opt} = \eta_d T_{GaAs} T_{cone} T_{win} T_{air} T_{BS} T_{bol}, \tag{5.4}$$

where $\eta_d \sim 0.25$ for collection of spontaneous emission from only one side of the sample, $T_{GaAs} \sim 0.69$ for the GaAs/Air interface, $T_{cone} \sim 0.5$ for the cone optic, $T_{air} \sim 0.3$ for absorption in the air, $T_{BS} \sim 0.5$ for the FTIR beamsplitter, and $T_{bol} \sim 0.5$ for the bolometer polyethylene input window and 20 μm cut on filter. A Z-cut single crystal quartz window (1.6 mm thick) was used as the inner output window of the cryostat during experiments on the three level design. The emission frequency of the three level design was $\sim 22 meV$ where quartz has very low absorption. Unfortunately, quartz has an absorption resonance at 33.5 meV making it unsuitable as window material for higher frequencies. Therefore we changed to single crystal sapphire (random orientation) for experiments on the four level design where the emission was designed for higher frequency $\sim 30 meV$. Figure 5-3 shows the absorption loss of quartz and sapphire as a function of frequency, taken from Loewenstein et. al. [69]. Polypropylene was used as the output vacuum window in both experiments. Room temperature measurements using our FTIR give a transmission of ~ 0.7 for the polypropylene window (0.2 mm thick). The combined transmission of both inner and outer windows, including reflection and absorption loss, is estimated to be $T_{win}^{3L} \sim 0.41$ and $T_{win}^{4L} \sim 0.3$ for the three level and four level designs. The total collection efficiency is therefore $\eta_{opt}^{3L} \sim 2.7 \times 10^{-3}$ and $\eta_{opt}^{4L} \sim 1.9 \times 10^{-3}$. It must be clear that this is only a rough estimate since many far infrared properties are difficult to measure.

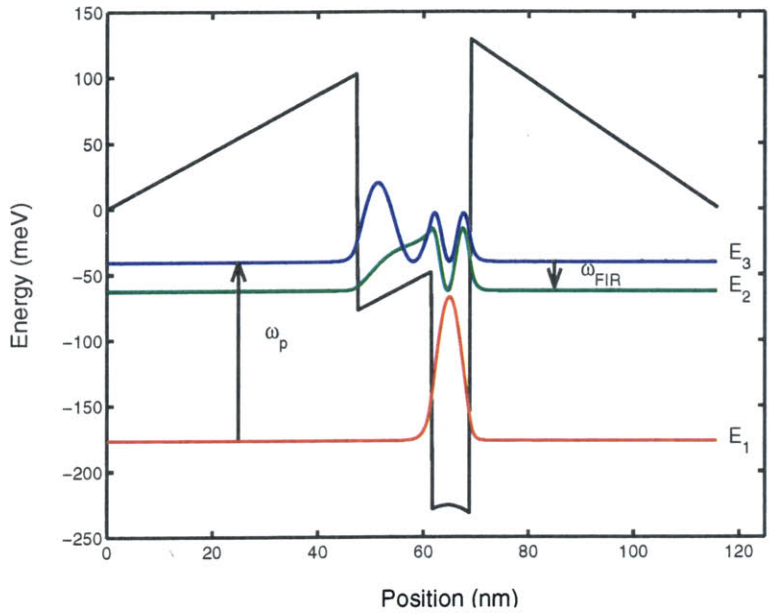

Figure 5-4: Step quantum well structure for the three level design. The structure is delta doped in the barriers to produce an electron density of $3 \times 10^{11} cm^{-2}$. The calculated transition energies are $\Delta E_{13} = 136.1\, meV$, $\Delta E_{12} = 114.0\, meV$ and $\Delta E_{23} = 22.1\, meV$. The calculated dipole matrix elements are $Z_{12} = 19.1$ Å, $Z_{23} = 45.3$ Å and $Z_{13} = 7.2$ Å.

5.4 Three Level Design

A step quantum well structure was used to implement the three level design. Intersubband transitions in step wells have inherently narrower linewidths compared to coupled double wells because the excited state wavefunctions in coupled double wells overlap more AlGaAs-GaAs interfaces leading to increased interface roughness scattering [70]. However, step wells are more difficult to grow by molecular beam epitaxy since steps require two different Al compositions. Figure 5-4 shows the calculated energy levels and square of the wavefunctions for the three level step quantum well design. Electrons are optically pumped from the ground state E_1 to E_3. The far infrared emission occurs between levels E_3 and E_2 at $\hbar\omega_{32} \sim 22$ meV.

The three level step well design was grown by Prof. Ben Streetman and Chad Hansing at the University of Texas at Austin. Molecular beam epitaxy was used to

grow 50 periods of $Al_{0.4}Ga_{0.6}As-Al_{0.2}Ga_{0.8}As-AsGaAs-Al_{0.4}Ga_{0.6}$ heterostructures on a semi-insulating GaAs substrate. Each quantum well period was separated by a 950 $\AA$ barrier. A Si delta doping layer was placed in the center of the barriers to provide approximately $3 \times 10^{11} cm^{-2}$ electrons in the ground state of the quantum wells.

Figure 5-5 shows the results of the mid infrared absorbance measurement at room temperature. Two absorption peaks are visible for the $E_1 \rightarrow E_3$ and $E_1 \rightarrow E_2$ transitions. The measured transition energies for the two peaks are $E_3 - E_1 = 130.2\, meV$ and $E_2 - E_1 = 108.0\, meV$ in good agreement with the calculated values (136 meV and 114 meV respectively). The agreement is actually better than it appears because we expect a small blue shift of 3-4 meV when the sample is cooled to LHe temperatures. Note also that the difference between the two peak positions almost exactly matches the calculated value for $E_3 - E_2 = 22\, meV$. A Lorentzian curve fit gives the broadening or full width at half-maximum (FWHM) of $2\Gamma_{12}$= 12.6 meV and $2\Gamma_{13}$= 8.4 meV. The measured absorption strengths are $I_{12} = 47\, meV$ and $I_{13} = 2.9\, meV$. From the measured absorption strengths and assuming an electron density of $3 \times 10^{11}\, cm^{-2}$, we estimate measured dipole matrix elements of $Z_{12} = 20.5\,$Å and $Z_{13} = 4.6\,$Å, also close to the calculated values (19.1 Å and 7.2 Å respectively).

The measured emission spectrum is shown in 5-6. A weak emission peak emerges at 22 meV as the device is cooled to super fluid temperatures. This peak corresponds closely to the design value for the $E_3 \rightarrow E_2$ transition and we interpret it as being due to intersubband spontaneous emission. The emission peak lies on top of a broad black body spectrum. The black body emission results since most of the pump photon energy is converted to LO phonons and eventually to acoustic phonons or heat. There is also a strong dip at ~33-35 meV. This dip is due to transverse optical (TO) phonon absorption resonances in the quartz window at 33.5 meV and in GaAs at 34 meV [69, 6]

The single well spontaneous emission efficiency for the three level design is given

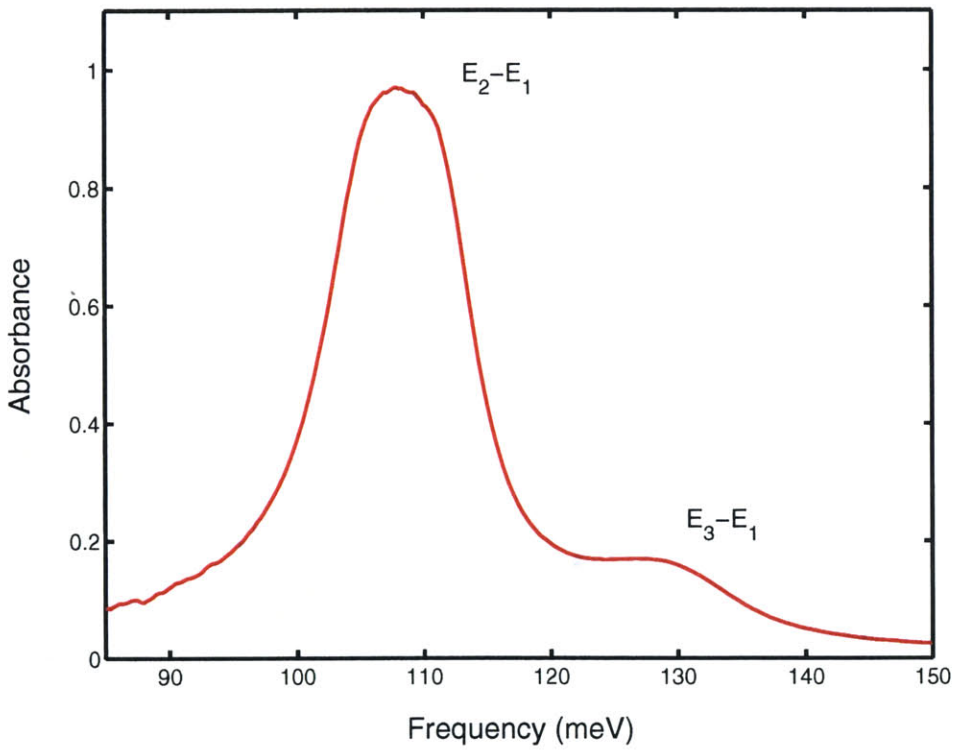

Figure 5-5: Absorption measurement for the three level design. The measured transition energies are $\Delta E_{13} = 130.2\,meV$, $\Delta E_{12} = 108.0\,meV$ and $\Delta E_{23} = 22.2\,meV$. The measured dipole matrix elements are $Z_{12} = 20.5$ Åand $Z_{13} = 4.6$ Å.

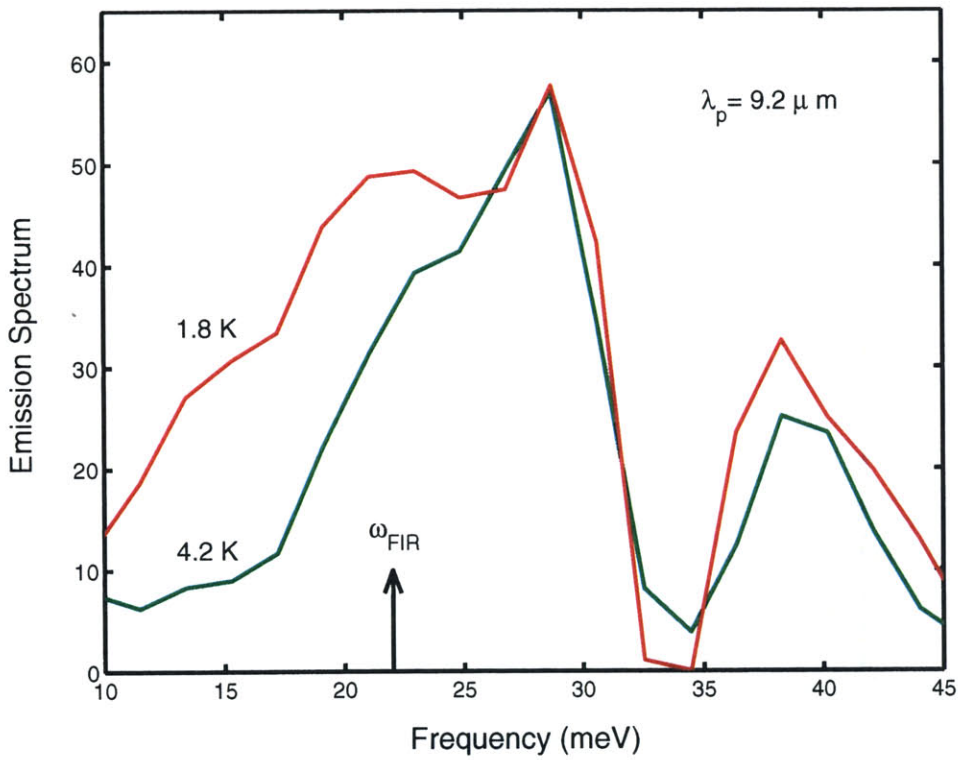

Figure 5-6: Far infrared emission measurement for the three level design. The peak at 22 meV is attributed to $E_3 \rightarrow E_2$ intersubband spontaneous emission. The absorption band at 33-35 meV is due to TO phonon absorption in the Quartz window at 33.5 meV and the GaAs substrate at 34 meV.

by

$$\eta_{3L} = \sigma_{13} n_1 \frac{\omega_{23}}{\omega_{13}} \frac{\tau_3^{tot}}{\tau_{23}^{rad}}. \tag{5.5}$$

The calculated values are $\sigma_{13} = 0.66 \times 10^{-14} cm^2$, $n_1 = 3 \times 10^{11} cm^{-2}$, $\omega_{23}/\omega_{13} = 0.16$, $\tau_3^{tot} = 2.4$ ps, and $\tau_{32}^{rad} = 3.4\ \mu s$, which gives a theoretical single well emission efficiency of 0.226 nW/W. Thus, the theoretical emission efficiency for 50 quantum wells is 11.3 nW/W.

The total measured emission power was approximately 1 pW for 500 mW of pump power. This corresponds to an overall efficiency of 2 pW/W. If we divide out the far infrared collection efficiency $\sim 2.7 \times 10^{-3}$, the measured emission efficiency is $\sim$ 0.74 nW/W. This value is about an order of magnitude lower than the calculated emission efficiency of 11.3 nW/W. Indeed, the far infrared intersubband emission was so weak that its spectrum was dominated by black body radiation. Although an emission peak was visible at 22 meV, it was impossible to obtain the linewidth. This poor experimental result along with inconclusive results by other researchers on similar three level structures motivated us to search for improved quantum well designs.

5.5 Four Level Design

The four level design employs the coupled triple quantum well structure of chapter 2. Figure 5-7 shows the calculated energy levels and square of the wavefunctions. Electrons are optically pumped from the ground state E_1 to E_4. $E_4 - E_3$ is separated by approximately one LO-phonon energy (36 meV) so that electrons quickly decay from E_4 to E_3. The far infrared emission occurs between levels E_3 and E_2 at $\hbar\omega_{32} \sim$ 30 meV. Electrons quickly vacate E_2 back to the ground state E_1 via LO-phonon emission.

The four level triple coupled quantum well design was grown by Prof. Michael Melloch at Purdue University. Molecular beam epitaxy was used to grow 80 periods of $Al_{0.3}Ga_{0.7}As - GaAs$ heterostructures on a semi-insulating GaAs substrate. Each

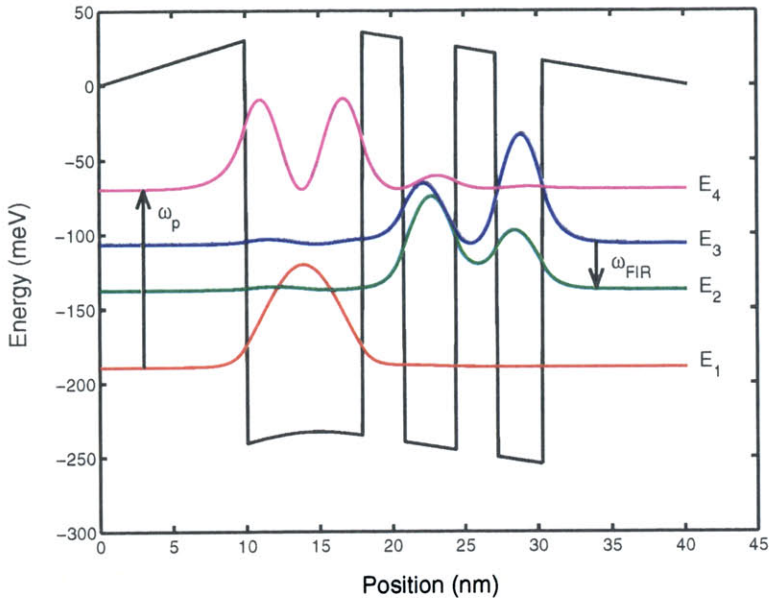

Figure 5-7: Triple coupled quantum well structure for the four level design. The calculated transition energies are $\Delta E_{14} = 119.5\,meV$, $\Delta E_{13} = 82.7\,meV$, $\Delta E_{12} = 51.9\,meV$ and $\Delta E_{23} = 30.8\,meV$. The calculated dipole matrix elements are $Z_{12} = 11.8\,\text{Å}$, $Z_{23} = 38.0\,\text{Å}$, $Z_{13} = 9.4\,\text{Å}$, $Z_{14} = 18.1\,\text{Å}$, $Z_{34} = 31.6\,\text{Å}$ and $Z_{24} = 9.6\,\text{Å}$.

quantum well period was separated by a 200 $\mathring{A}$ barrier. A Si delta doping layer was placed in the center of the barriers to provide approximately $3 \times 10^{11} cm^{-2}$ electrons in the ground state of the quantum wells.

Figure 5-8 shows the results of the mid infrared absorption measurement. The $E_1 \rightarrow E_4$ absorption peak is clearly evident with a center frequency of 119.8 meV, close to the design value of 119.5 meV. A Lorentzian curve fit gives a FWHM of $2\Gamma_{14}$= 13 meV. The measured absorption strength is $I_{14} = 48\,meV$ corresponding to a dipole matrix element of $Z_{14} = 15.6\,\text{Å}$. This value is close to the calculated dipole matrix element of 18.1 Å. The $E_1 \rightarrow E_2$ (51.9 meV) and $E_1 \rightarrow E_3$ (82.7 meV) absorption peaks were not observed because they fall below the frequency range of our mid infrared MCT detector. However, since the $E_1 \rightarrow E_4$ transition energy came out close to the design value, we also expect the far infrared emission to occur close to its design value of 30.8 meV.

The measured emission spectrum is shown in Figure 5-9. The solid curve corre-

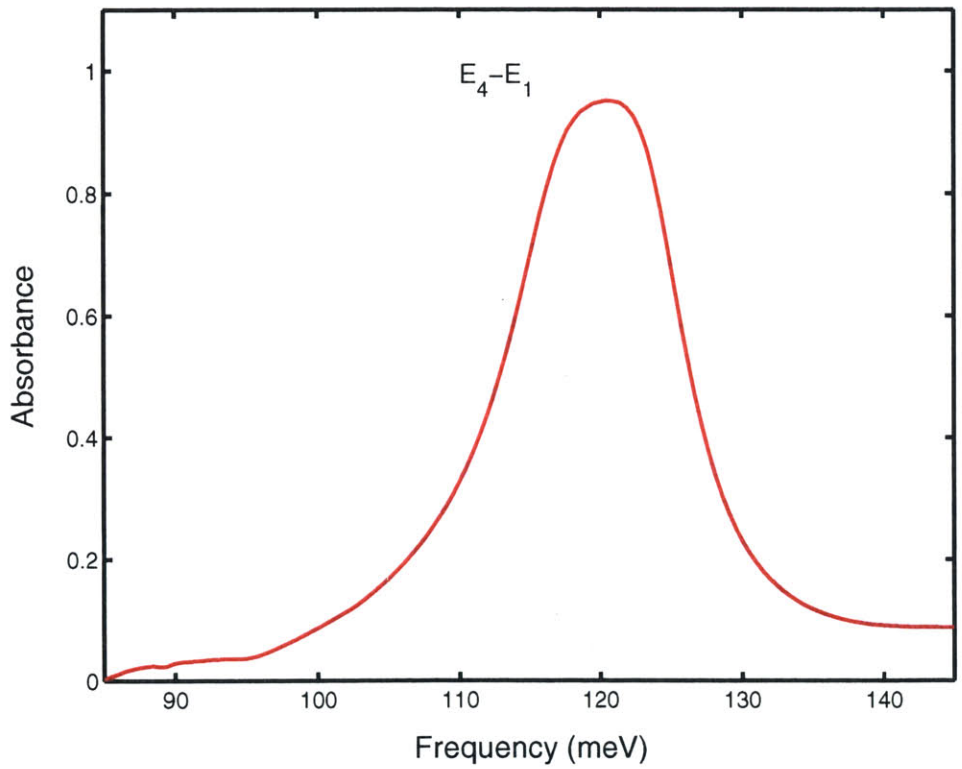

Figure 5-8: Absorption measurement for the four level design. Only the $E_1 \rightarrow E_4$ transition is in the mid infrared range of the MCT detector. The measured transition energy and dipole matrix element are $\Delta E_{14} = 119.8\,meV$ and $Z_{14} = 15.6$ Åsrespectively.

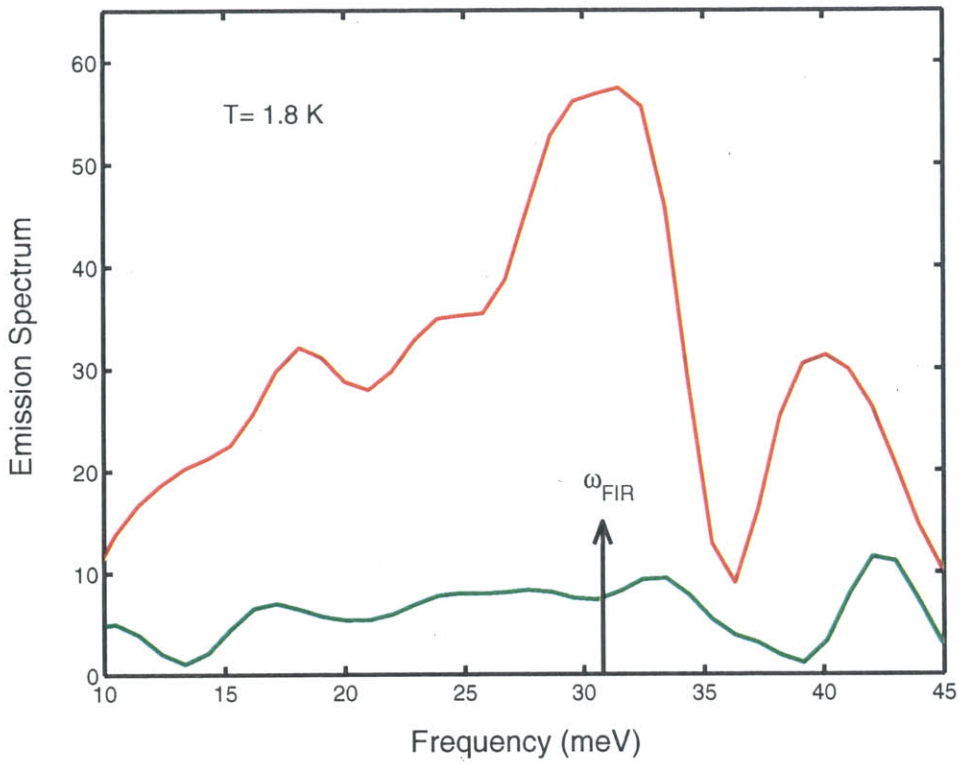

Figure 5-9: Far infrared emission measurement for the four level design. The red curve shows the emission spectrum when the CO_2 laser is tuned to resonance with the pump transition $E_4 - E_1$. The emission peak at 30.8 meV is due to $E_3 \rightarrow E_2$ intersubband spontaneous emission. The dip at 35 meV is due to TO phonon absorption in the GaAs substrate. The green curve shows what happens when the pump laser is tuned off resonance.

sponds to the pump being tuned to resonance. We see a prominent peak centered at 30.8 meV, exactly at the design value of the $E_3 \rightarrow E_2$ transition. A Lorentzian curve fit gives a FWHM of $\sim$ 7 meV. This is a relatively narrow linewidth in comparison with the room temperature linewidth of 13 meV for the $E_1 \rightarrow E_4$ transition. The emission peak lies on top of a broad black body spectrum. We also observe a dip at $\sim$ 35-36 meV due to TO phonon absorption. Note that we measure the TO phonon absorption resonance to be slightly above the value of 34 meV in GaAs [6]. The higher measured value of TO phonon energy may be due to the $Al_{0.3}Ga_{0.7}As$ barriers.

When the pump is tuned off resonance, only bulk absorption can take place and the emission should mainly result from blackbody radiation. The green curve shows

what happens to the spectrum when the pump frequency is tuned below the $E_1 \rightarrow E_4$ resonance. The measured signal drops significantly and the emission peak at 30.8 meV vanishes as expected. In a separate experiment we measured the emission spectrum from a rectangular shaped sample oriented so that the pump polarization is in the plane of the quantum wells. Since intersubband transitions are forbidden for this polarization of the pump, we expect to see only black body radiation due to free carrier absorption. Figure 5-10 shows the black body emission spectrum. Most features of this black body spectrum resemble the spectrum of Figure 5-9 *except* for the absence of an emission peak at 30.8 meV. This provides additional evidence that we measured a real emission peak due to far infrared intersubband transitions.

The single well spontaneous emission efficiency for the four level design is given by

$$\eta_{4L} = \sigma_{14} n_1 \frac{\omega_{23}}{\omega_{14}} \frac{\tau_4^{tot}}{\tau_{34}} \frac{\tau_3^{tot}}{\tau_{23}^{rad}}. \tag{5.6}$$

The calculated values are $\sigma_{14} = 0.36 \times 10^{-13} cm^2$, $n_1 = 3 \times 10^{11} cm^{-2}$, $\omega_{23}/\omega_{14} = 0.26$, $\tau_4^{tot} = 0.35$ ps, $\tau_{34} = 0.72$ ps, $\tau_3^{tot} = 6.2$ ps and $\tau_{23}^{rad} = 1.8\ \mu s$, which gives a theoretical single well emission efficiency of 4.6 nW/W. Thus, the theoretical emission efficiency for 80 quantum wells is 368 nW/W.

We measured $\sim$ 6 pW of far infrared emission power for 200 mW of pump power. This gives an overall efficiency of 30 pW/W. After dividing out the far infrared collection efficiency of 1.9×10^{-3}, we get a measured emission efficiency of 16 nW/W. As in the three level design, the measured value of emission efficiency is about one order of magnitude off from the calculated value.

5.6 Concluding Remarks

The order of magnitude discrepancy between measured and calculated emission efficiency in both three level and four level designs was most likely caused by heating effects [64, 65]. We showed in Chapter 3 how the opening of a parasitic LO phonon

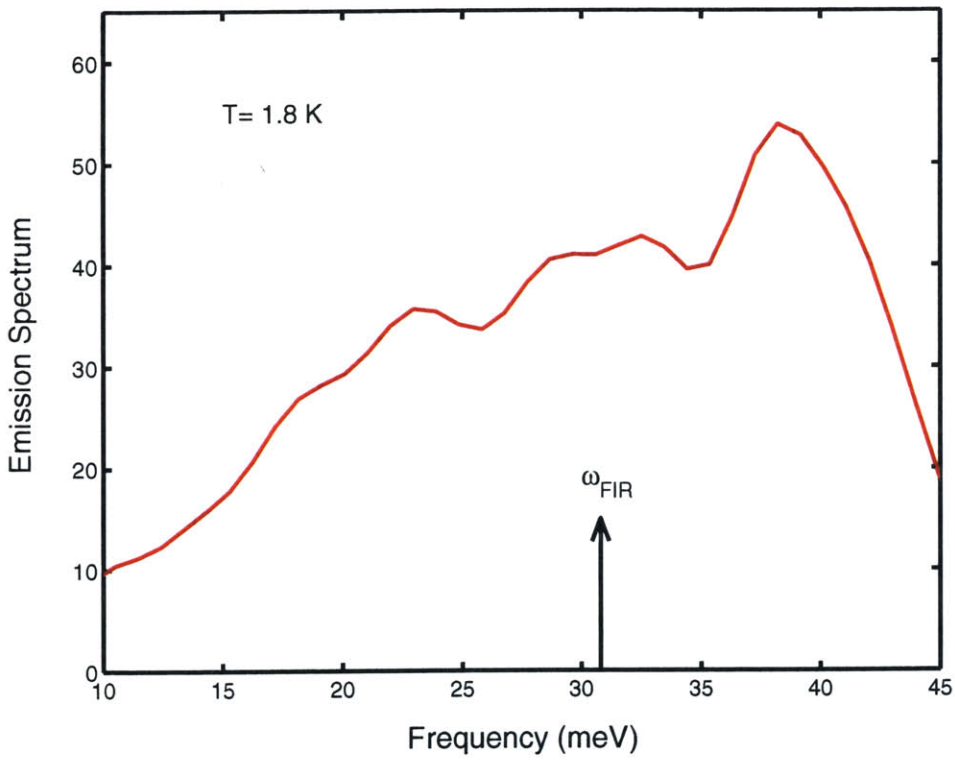

Figure 5-10: Black body emission for 200 mW of pump power polarized in the plane of the quantum well layers. Note the absence of a peak at 30.8 meV.

scattering channel between E_3 and E_2 at high temperatures can easily lower the emission efficiency by more than an order of magnitude. Broadening of the far infrared transition may also contribute to the opening of this parasitic LO phonon channel [71].

It is interesting to compare the relative strength of the four level and three level designs. To make a fair comparison, we must scale the measured emission efficiency of the three level design by the factor

$$\frac{\omega_{4L}^4}{\omega_{3L}^4} = 3.84 \tag{5.7}$$

since the two designs had different emission frequencies and $\eta \propto \omega^4$. Multiplying the measured emission efficiency of the three level design by the factor 3.84 we get 2.8 nW/W. This value is still a factor of 6 lower than the measured emission efficiency of 16 nW/W for the four level design. We can conclude that the superior emission spectrum of the four level design resulted from a much stronger emission efficiency. This provides a satisfying confirmation of the theory.

Chapter 6

Conclusions and Future Work

6.1 Conclusions

This thesis took the first difficult steps in the development of optically pumped far infrared quantum well lasers. Building on the work of previous research on mid infrared intersubband lasers, a three level system in a step quantum well was designed to measure optically pumped far infrared intersubband emission. Subsequent measurements revealed that the far infrared emission was too weak to clearly resolve the spectrum. Moreover, when we tried to improve the design to increase the far infrared emission power, it became clear that three level systems lack the flexibility to optimize the gain and emission efficiency. This lack of flexibility in three level designs comes from the necessity to couple the CO_2 pump laser to the same transition $E_1 \rightarrow E_3$ that couples the LO phonon scattering responsible for limiting the gain and emission efficiency.

We realized that the real power of quantum wells as artificial atoms lies in more complex designs involving higher energy level schemes [36]. A four level scheme using triple coupled quantum wells was proposed and analyzed. The four level design effectively decoupled the pumping rate from the LO phonon scattering rate appearing in the gain and emission efficiency. Thus, these two important rates could be optimized independently. This innovation improved the gain and emission efficiency by an order

Table 6.1: *Summary of experimental results.*

	$\Delta E_{1p}(meV)$	Z_{1p} (Å)	ΔE_{23} (meV)	η (nW/W)
3L Measured	130.2	4.6	22.0	0.7
3L Calculated	136.1	7.2	22.1	11
4L Measured	119.8	15.6	30.8	16
4L Calculated	119.5	18.1	30.8	368

of magnitude over previous three level designs. Optically pumped far infrared intersubband emission experiments verified the superior qualities of the four level system. The four level design exhibited an order of magnitude stronger emission power. The stronger emission made possible the first clear measurement of a far infrared spontaneous emission spectrum from optically pumped quantum wells [37]. Table 6.1 shows a summary of experimental results for the three and four level designs.

The emission measurements revealed a serious problem: much weaker emission power than expected for both three and four level designs. The order of magnitude weaker emission was attributed to heating effects. Heating of the electron gas can result in the opening of a parasitic LO phonon scattering channel. This parasitic scattering channel opens when electrons gain enough thermal energy to scatter from E_3 to E_2 by emitting an LO phonon. Once this LO phonon window is opened, both the gain and emission efficiency drop by a factor of ten.

After a thorough analysis of heating effects, we determined the best strategy to overcome increased scattering $\frac{1}{\tau_{23}}$ is to fight fire with fire by enhancing the scattering rate $\frac{1}{\tau_{12}}$ for faster depopulation of the lower laser level E_2. Unfortunately, the limited tunability of the CO_2 pump laser puts a constraint on enhancing the LO phonon scattering rate $\frac{1}{\tau_{12}}$ in four level systems. Thus, we proposed and analyzed a five level design scheme using quadruple coupled quantum wells. The five level design is very similar to the four level design except for the crucial difference that the energy alignment $E_2 - E_1$ can be made exactly equal to the LO phonon energy. This optimum energy alignment increased the LO phonon scattering rate $\frac{1}{\tau_{12}}$ by a factor of five, resulting in improved high temperature performance.

6.2 Future Work

6.2.1 Fabrication

The most natural next step after successful demonstration of far infrared intersubband emission is to fabricate and test a laser waveguide structure. The laser waveguide we propose is shown in Figure 3-5. A very thin $\sim 5\,\mu m$ rectangular waveguide is needed to confine the far infrared laser mode. Such a waveguide can be fabricated using polishing and selective etching [31].

The challenge would be to also fabricate an optical quality grating with $\sim 1\,\mu m$ features on the top surface of the waveguide for coupling the CO_2 pump laser. Unfortunately, the process of polishing and selective etching leaves plenty of particles on the sample that makes photolithography of a fine grating very challenging. One possibility to overcome this problem is to simply bypass the necessity of fabricating a grating altogether by using cross band pumping. The shorter wavelengths used in cross band pumping allow for coupling through the side of the waveguide. Alternative optical pumping schemes are discussed next.

6.2.2 Pumping Schemes

Optical pumping with a CO_2 laser has many disadvantages besides the necessity of fabricating a grating. The CO_2 laser is only tunable in a narrow frequency rage 110 - 135 meV, with gaps at 119, 124 and 132 meV. This limited tunability puts severe restrictions on the quantum well design. For example, the ideal design would be the four level system shown in Figure 6-1. This design combines all the advantages of four level systems described in Chapter 3 with the superior high temperature performance of the five level design presented in Chapter 4. In addition, the emission efficiency is increased because lower pump photon energy enhances the Manley-Rowe factor. Unfortunately, the frequency range of the CO_2 laser is above the energy of the pump transition in the ideal four level system 90 - 100 meV. The CO_2 laser is also very

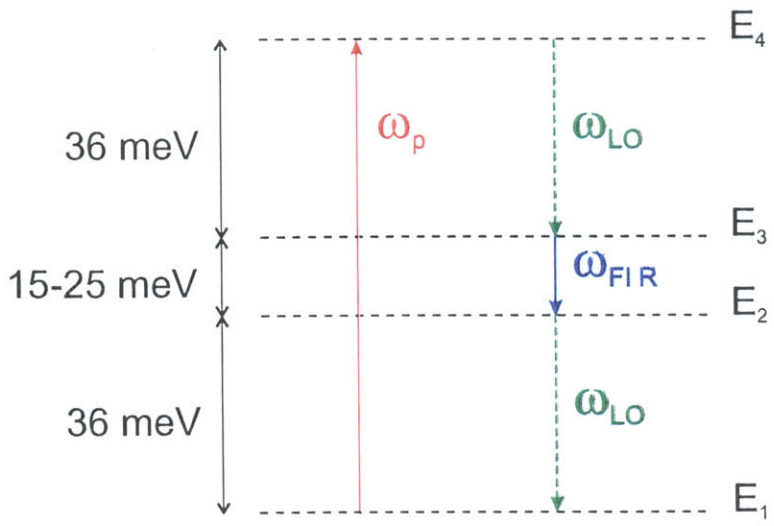

Figure 6-1: The ideal four level design. Both $E_4 - E_3$ and $E_2 - E_1$ transition energies are set to the LO phonon energy giving the optimum conditions for population inversion. A QCL laser operating at $\hbar\omega \sim 90 - 100\, meV$ is necessary to pump electrons from E_1 to E_4.

expensive, bulky and limited in pulse mode operation.

An interesting direction for future work would be to develop a mid infrared Quantum Cascade Laser (QCL) as a pump source for the far infrared quantum well laser. The QCL is tunable and can be designed to operate in the optimum pumping range of 90 - 100 meV. Moreover, a QCL can be put right next to the far infrared laser waveguide sample in the cryostat. Thus, optical alignment of the pump is done only once at room temperature. A QCL also has superior modulation capability through modulation of the current, providing additional flexibility for experiments. The major challenge in applying this idea is to improve the peak output power of QCLs beyond 1 Watt in pulse mode [72]. QCLs operating at $\lambda \sim 11\, \mu m$ have been demonstrated with 100 mW of peak output power [73]. Of course, even if it is not possible to further increase the output power, one can always combine several QCLs to increase the total pump power.

Another interesting optical pumping scheme is shown in Figure 6-2. This pumping scheme involves cross band pumping with a semiconductor diode laser. There

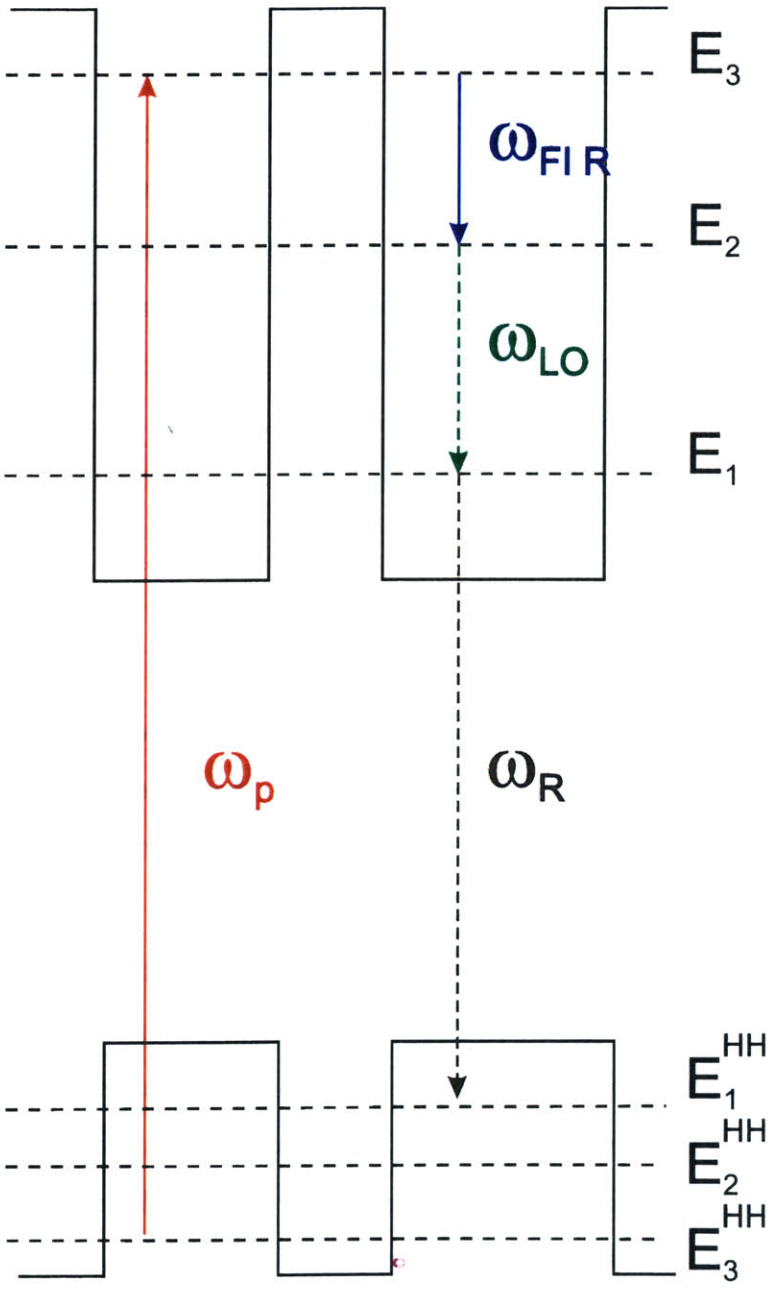

Figure 6-2: Cross band pumping scheme using a diode laser.

are many advantages in cross band pumping. Since electrons are pumped from the valence band, doping is not necessary. Thus, all of the deleterious effects associated with doping, like free carrier absorption and ion impurity scattering, are completely eliminated. Cross band pumping automatically decouples the pump transition from the LO phonon scattering transition $E_3 \rightarrow E_1$ that limits the emission efficiency and gain. In addition, it is not necessary to fabricate a grating to couple the pump laser. Since $\lambda_p \sim 1\,\mu m$ is smaller than the active region thickness, the pump laser can be coupled through the side of the laser waveguide. The smaller pump wavelength is a disadvantage in terms of emission efficiency. However, the lower cost and higher efficiency of semiconductor diode lasers compared to CO_2 lasers should nullify the disadvantage of lower far infrared emission efficiency.

6.2.3 Material Systems

We used the AlGaAs-GaAs material system because molecular beam epitaxy technology is more available in this system. However, there are big advantages in using different material systems. Table 6.2 compares the properties of several interesting materials, obtained from references [74, 75, 6].

The physics of photon and phonon induced intersubband transitions was discussed in Chapter 2. Quantum wells based on material systems with lower effective mass have larger dipole moments by a factor of $\sqrt{\frac{m_1^*}{m_2^*}}$. The LO phonon scattering rates decrease by the same factor in the smaller effective mass material. The dipole moments and LO phonon scattering rates are important measures of ultimate laser performance because both gain and emission efficiency are proportional to $Z_{1p}^2 Z_{23}^2 \tau_{13}$. Thus, changing from AlGaAs-GaAs to InAlAs-InGaAs based material system will improve the gain and emission efficiency by a factor of

$$\left(\frac{m^*_{GaAs}}{m^*_{In_{0.53}Ga_{0.47}As}}\right)^{\frac{5}{2}} \sim 3.5 \tag{6.1}$$

Table 6.2: *Material properties.*

	E_G (eV)	m^*/m_e	ω_{LO} (meV)	ω_{TO} (meV)
GaAs	1.42	0.067	36	34
$In_{0.53}Ga_{0.47}As$	0.75	0.041	33.5	28
InAs	0.354	0.023	29.6	26.4
Si	1.12	0.49 (HH)	63	63

The InAlAs-InGaAs material system is a particularly favorable choice because molecular beam epitaxy technology is already well developed for this system in the context of semiconductor diode quantum well lasers. However, we may be able to do even better. Table 6.2 shows that InAs has an even lower effective mass than $In_{0.53}Ga_{0.47}As$. Using InAs as the well material will give a factor of 15 improvement in gain and emission efficiency! The only drawback with using InAs is that it is not lattice matched to the InP substrate (3 % mismatch). This may not pose a problem if strained InAs quantum wells can be grown successfully. In any event, midgap states introduced by lattice mismatch dislocations should not affect optically pumped unipolar lasers except for possible linewidth broadening. If the linewidth broadening is a weaker effect on gain than the improvement due to reduced effective mass, then we still win by using InAs.

High temperature performance depends critically on the LO phonon energy $\hbar\omega_{LO}$. Materials with larger $\hbar\omega_{LO}$ experience the opening of the parasitic LO phonon scattering channel $\frac{1}{\tau_{23}}$ at a higher temperature. Table 6.2 shows that the best material system for improving high temperature performance is the SiGe-Si system where $\hbar\omega_{LO} \sim 63\,meV$. Si is also advantageous because it is a nonpolar material. Thus, polar optical phonon scattering is completely absent in Si, resulting in much weaker nonradiative scattering rates [76]. A major disadvantage of using SiGe-Si based quantum wells is the fact that most of the band offset is in the valence band. Quantum well lasers based on intersubband transitions between holes have the disadvantage of considerably higher effective mass.

In this author's opinion, the most promising direction for future research on opti-

cally pumped far infrared quantum well lasers lies in using quantum well structures based on the InAlAs-InGaAs material system, combined with cross band pumping. The use of InAlAs-InGaAs material will give a factor of 3.5 improvement in gain, while cross band pumping will eliminate the largest contribution to loss coming from free carrier absorption.

Appendix A

Far Infrared Nonlinear Optics in Quantum Wells

Since the early days of nonlinear optics, there have been efforts to develop nonlinear optical techniques for the generation of far infrared radiation [6]. Earlier efforts in the development of far infrared difference frequency mixers and OPO's suffered from the relatively weak nonlinear susceptibility ($\chi^{(2)} \sim 10^{-10} m/V$) of bulk materials. Recent studies of the nonlinear optical properties of asymmetric double quantum wells using AlGaAs-GaAs heterostructures have shown that these structures posses enormous nonlinear susceptibility $\chi^{(2)} \sim 10^{-6} m/V$, which is four orders of magnitude greater than in bulk GaAs [42]. Quantum wells act like giant artificial atoms, whose nonlinear optical properties can be optimized by proper design [77]. These advances motivated us to consider the feasibility of parametric oscillation at far infrared frequencies [33]. A rigorous theoretical analysis showed that far infrared OPO's would require much higher threshold pump power compared to quantum well lasers [34]. However, it is still interesting to study the nonlinear optical properties of quantum wells in the far infrared.

A large value of $\chi^{(2)}$ is achieved by designing an asymmetric double quantum well structure that is doubly resonant at both the pump ω_p and signal ω_s frequencies.

Figure 2-1 of Chapter 2 shows the energy levels and wavefunctions for such a structure. If only the ground state E_1 is occupied, and when ω_p and ω_s are close to resonance,

$$\chi^{(2)}(\omega_s = \omega_p - \omega_i) = \frac{e^3 N}{\epsilon_0} \frac{Z_{12} Z_{23} Z_{13}}{(\Delta E_{12} - \hbar\omega_s + i\frac{\Gamma_{12}}{2})(\Delta E_{13} - \hbar\omega_p + i\frac{\Gamma_{13}}{2})}, \qquad \text{(A.1)}$$

where N is the three dimensional electron density in the quantum wells, Z_{ij}'s are the dipole matrix elements, and Γ_{ij}'s are the linewidth broadenings. Note that Z_{13} vanishes in symmetric quantum well structures. This reflects the general principle that crystals with inversion symmetry have vanishing second order nonlinear susceptibility.

Quantum wells posses much stronger nonlinear effects compared to natural atoms because of larger dipole matrix elements and the ability to design quantum wells for resonance enhancement. A direct comparison of $\chi^{(2)}$ in quantum wells versus atoms in natural crystals gives,

$$\frac{\chi^{(2)}_{qw}}{\chi^{(2)}_{atom}} \sim \frac{N_{qw}}{N_{atom}} (\frac{L}{a})^3 \frac{\hbar\omega_s}{\Gamma}, \qquad \text{(A.2)}$$

where $N_{qw} \sim 10^{18}\, cm^{-3}$ is the electron density in a typical quantum well, $N_{atom} \sim 10^{21}\, cm^{-3}$ is solid density, $\frac{L}{a}$ is a ratio of quantum well thickness ~ 100 Å to lattice constant ~ 1 Å, and $\frac{\hbar\omega_s}{\Gamma} \sim 10$ is due to resonance enhancement. Thus, we see how the nonlinear susceptibility of quantum wells can be a factor of 10^4 larger than in natural crystals.

It is interesting to compare far infrared difference frequency generation with the optically pumped far infrared emission results of Chapter 5. We performed far infrared difference frequency mixing experiments using a quantum well sample provided by Dr. Carlo Sirtori of Bell Labs. The energy levels and wavefunctions for Sirtori's quantum well structure are shown in figure 2-1. Figure A-1 shows the room temperature absorption measurement for Sirtori's sample. The measured transition energies are in very good agreement with the numerical calculations described in Chapter 2.

The experimental setup for far infrared difference frequency mixing is similar to that used for the optically pumped far infrared emission measurements. The outputs

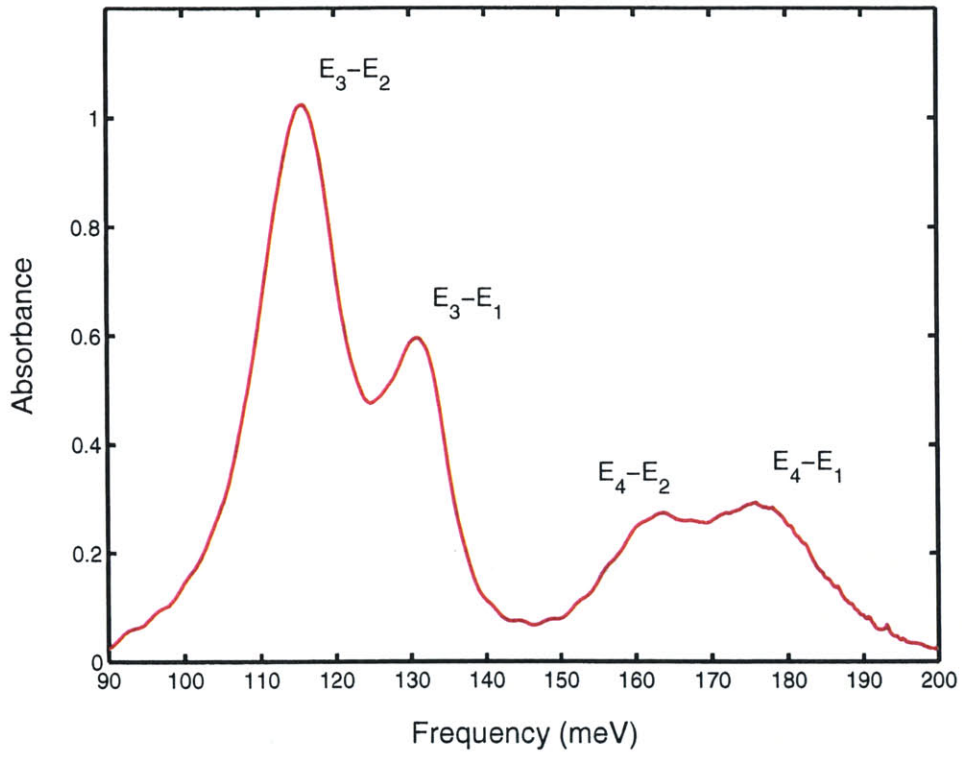

Figure A-1: Absorption measurement for Sirtori's asymmetric double quantum well sample.

of two CO_2 lasers, tuned to different frequencies ω_p and ω_i, are combined in a beam splitter. The pump frequency ω_p is tuned to the $E_3 - E_1$ transition while the idler frequency ω_i is tuned to the $E_3 - E_2$ transition. Careful attention must be paid to ensure good overlap of the pump and idler beams. The sample is processed into a trapezoid one bounce geometry and mounted in a LHe cryostat. The sample geometry is designed for a single bounce on the epilayer side of the sample to ensure that the interaction length is much shorter than the coherence length $l_c \sim 100\,\mu m$. Thus, phase matching is not an issue in this experiment. The CO_2 laser beams are focused onto the polished end of the sample using an f = 5 inch ZnSe lens. ZnSe is also used for the mid infrared input windows to the cryostat. Quartz is used as the far infrared output window material and as a mid infrared filter for the CO_2 laser radiation. The output far infrared radiation is collected by two off axis paraboloid mirrors with f = 3 inch and focused onto a LHe Si bolometer. The CO_2 lasers are chopped at 500 Hz for lock-in detection.

Figures A-2 and A-3 show the results of our far infrared difference frequency measurements. The interpretation of the data is simple of we remember that the far infrared difference frequency signal must be proportional to the product of pump and idler laser power $\propto I_p I_i$. Thus, we expect a linear dependence on pump power when the idler power is kept constant and a quadratic dependence when $I_i = I_p$. Figure A-2 demonstrates this relationship. The polarization dependence is explained by the selection rule for intersubband transitions. As the polarization angle is varied the pump and idler wave amplitudes in the growth direction of the quantum wells obtain a $Sin\phi$ dependence. Thus, the product of the pump and idler power obtains a $Sin^4\phi$ dependence. This polarization selection rule is clearly evidenced in the data of figure A-3. It is also interesting to note that the total power generated in far infrared difference frequency mixing is comparable in magnitude to the far infrared intersubband emission power from optically excited quantum wells for similar pump power levels.

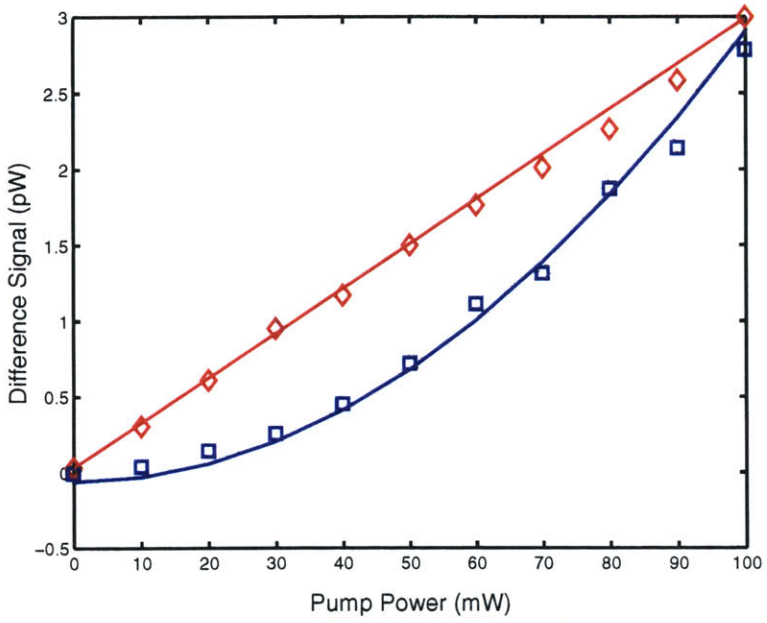

Figure A-2: Measured far infrared difference frequency signal versus pump power. The sample is cooled to 4.2 K. The red diamonds show the far infrared difference frequency generated as a function of pump power when the signal power is kept constants at 100 mW. The red curve is a linear fit to this data. The blue squares show what happens to the trend when the signal power is kept equal to the pump power. The blue curve is a quadratic fit to this data.

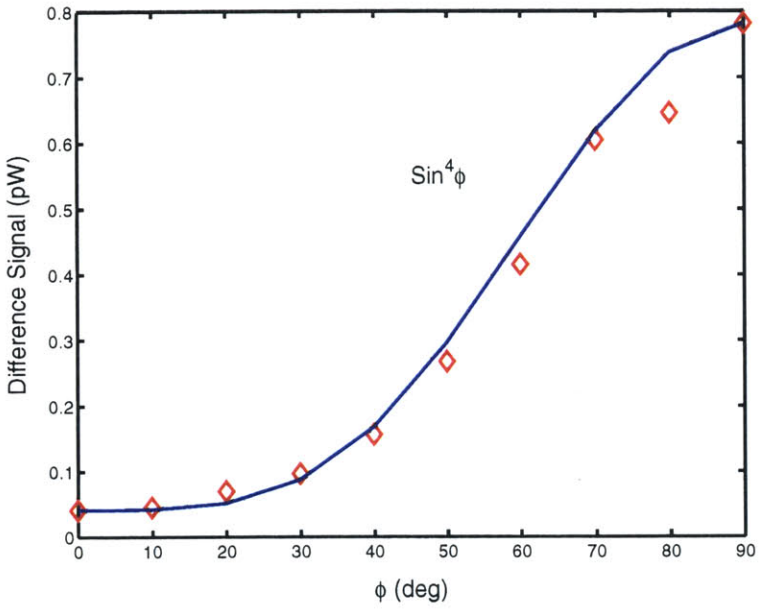

Figure A-3: Measured far infrared difference frequency signal versus pump and signal polarization angle. The pump and idler laser power is set at 50 mW. The sample is cooled to 4.2 K. The solid curve is a $Sin^4\phi$ fit to the data.

Bibliography

[1] M. Tacke. "New developments and applications of tunable IR lead salt lasers". *Infrared Phys. Technol*, 36:447–463, 1995.

[2] S. E. Rosenbaum, B. K. Kormanyos, L. M. Jelloin, M. Matloubian, A. S. Brown, E. Larson, L. D. Nguyen, M. A. Thompson, L. P. B. Katehi, and G. M. Rebeiz. "155- and 213-Ghz AlInAs/GaInAs/InP HEMT MMIC oscillators". *IEEE Trans. Microwave Theory Tech.*, 43:927–932, 1995.

[3] M. Inguscio, G. Moruzzi, K. M. Evenson, and D. A. Jennings. "A review of frequency measurements of optically pumped lasers from 0.1 to 8 THz". *J. Appl. Phys.*, 60:R161–R192, 1986.

[4] J. W. Bales. *Intersubband Transitions in Quantum Wells.* PhD Thesis, Massachusetts Institute of Technology, Department of Physics, 1991.

[5] D. A. G. Deacon, L. R. Elias, J. M. Madey, G. J. Ramian, H. A. Schwettman, and T. I. Smith. "First operation of a free-electron laser". *Phys. Rev. Lett.*, 38:892–894, 1977.

[6] R. L. Aggarwal and B. Lax. "Optical mixing of CO_2 lasers in the far-infrared". In Y. R. Shen, editor, *Nonlinear Infrared Generation*, pages 40–43. Springer-Verlag, Berlin, 1977.

[7] E. Gornik and A. A. Andronov. Special issue on "Far-infrared semiconductor lasers". *Opt. Quant. Electron.*, 23, 1991.

[8] K. Namjou, S. Cau, E. A. Whittaker, J. Faist, G. Gmachl, F. Capasso, D. L. Sivco, and A. Y. Cho. "Sensitive absorption spectroscopy with a room temperature distributed-feedback quantum-cascade laser". *Opt. Lett.*, 23:219–221, 1998.

[9] N. Katzenellenbogen and D. Grischkowsky. "Electrical characterization to 4 THz of n- and p-type GaAs using THz time-domain spectroscopy". *Appl. Phys. Lett.*, 61:840–842, 1992.

[10] L. Esaki and R. Tsu. "Superlattice and negative differential conductivity in semiconductors". *IBM J. Res. Dev.*, 14:61, 1970.

[11] A. Y. Cho. "Advances in molecular beam epitaxy (mbe)". *J. Chryst. Growth*, 111:1, 1991.

[12] D. Ahn and S. L. Chuang. "Intersubband optical absorption in a quantum well with an applied electric field". *Phys. Rev. B*, 35:4149–4151, 1987.

[13] G. Almogy, M. Segev, and A. Yariv. "Intersubband-transition-induced phase matching". *Opt. Lett.*, 19:1192–1194, 1994.

[14] S. I. Borenstain and J. Katz. "Evaluation of the feasibility of a far-infrared laser based on intersubband transitions in GaAs quantum wells". *Appl. Phys. Lett.*, 55:654–656, 1989.

[15] R. Ferreira and G. Bastard. "Evaluation of some scattering times for electrons in unbiased and biased single- and multiple-quantum-well structures". *Phys. Rev. B*, 40:1074–1086, 1989.

[16] L. C. West and S. J. Eglash. "First observation of an extremely large-dipole infrared transition within the conduction band of GaAs quantum well". *Appl. Phys. Lett.*, 46:1156–1158, 1985.

[17] Y. J. Mii, K. L. Wang, R. P. G. Karunasiri, and P. F. Yuh. "Observation of large oscillator strengths for both $1 \rightarrow 2$ and $1 \rightarrow 3$ intersubband transitions of step quantum wells". *Appl. Phys. Lett.*, 56:1046–1048, 1990.

[18] J. R. Meyer, C. A. Hoffman, and F. J. Bartoli. "Intersubband second-harmonic generation with voltage-controlled phase matching". *Appl. Phys. Lett.*, 67:608–610, 1995.

[19] J. Faist, F. Capasso, C. Sirtori, D. L. Sivco, A. L. Hutchinson, and A. Cho. "Laser action by tuning the oscillator strength". *Nature*, 387:777–782, 1997.

[20] F. Capasso. "Band-gap engineering: from physics and materials to new semiconductor devices". *Science*, 235:172–176, 1987.

[21] I. Lyubomirsky, B. Xu, and Q. Hu. "Developing quantum well sources of terahertz radiation". *LEOS Newsletter*, 11:13–14, 1997.

[22] R. F. Kazarinov and R. A. Suris. "Possibility of the amplification of electromagnetic waves in a semiconductor with a superlattice". *Soviet Physics: semiconductors*, 5:707–709, 1971.

[23] J. Faist, F. Capasso, D. L. Sivco, C. Sirtori, A. L. Hutchingson, and A. Y. Cho. "Quantum cascade laser". *Science*, 264:553–556, 1994.

[24] J. Faist, F. Capasso, C. Sirtori, D. Sivco, A. L. Hutchingson, and A. Y. Cho. "Continuous-wave operation of a vetical transition quantum cascade laser above T=80 K". *Appl. Phys. Lett.*, 67:3057–3059, 1995.

[25] J. Faist, F. Capasso, C. Sirtori, D. Sivco, J. N. Baillargeon, A. L. Hutchingson, and A. Y. Cho. "High power mid-infrared ($\lambda \sim 5$ μm) quantum cascade lasers operating above room temperature". *Appl. Phys. Lett.*, 68:3680–3682, 1996.

[26] C. Sirtori, J. Faist, F. Capasso, D. L. Sivco, A. L. Hutchinson, and A. Y. Cho. "Mid-Infrared (8.5 μm) semiconductor lasers operating at room temperature". *Photon. Technol. Lett.*, 9:294–296, 1997.

[27] J. Faist, C. Sirtori, F. Capasso, D. L. Sivco, J. N. Baillargeon, A. L. Hutchinson, and A. Y. Cho. "High-Power Long-Wavelength ($\lambda \sim 11.5\,\mu m$) quantum cascade lasers operating above room temperature". *Photon. Technol. Lett.*, 10:1100–1102, 1998.

[28] O. Gauthier-Lafaye, S. Sauvage, P. Boucaud, F. H. Julien, F. Glotin, R. Prazeres, J. M. Ortega, V. Thierry-Mieg, and R. Planel. "Investigation of mid-infrared intersubband stimulated gain under optical pumping in GaAs/AlGaAs quantum wells". *J. Appl. Phys.*, 83:2920–2926, 1998.

[29] M. Helm. "Far-infrared emission and absorption spectroscopy of quantum wells and superlattices". In E. Ronsencher et.al., editor, *Intersubband Transitions in Quantum Wells*, pages 151–161. Plenum Press, New York, 1992.

[30] J. H. Smet. *Interwell and Intrawell Intersubband Transitions in Single and Multiple Quantum Well Heterostructures.* PhD Thesis, Massachusetts Institute of Technology, Department of Electrical Engineering and Computer Science, 1995.

[31] B. Xu. *Development of Intersubband Terahertz Lasers Using Multiple Quantum Well Structures.* PhD Thesis, Massachusetts Institute of Technology, Department of Electrical Engineering and Computer Science, 1998.

[32] F. Capasso, C. Sirtori, and A. Cho. "Coupled quantum well semiconductors with giant electric field tunable nonlinear optical properties in the infrared". *IEEE J. Quan. Electron.*, 30:1313–1326, 1993.

[33] I. Lyubomirsky, B. Xu, and Q. Hu. "THz parametric oscillators using coupled double quantum wells". In *Proceeding of the 1995 International Semiconduc-*

tor Device Research Symposium, number 26, page 623. University of Virginia, Charlottesville, Virginia, 1995.

[34] I. Lyubomirsky and Q. Hu. "Optical parametric oscillators without phase matching". *J. Opt. Soc. Am. B*, 14:984–988, 1997.

[35] L. A. Coldren and S. W. Corzine. *Diode Lasers and Photonic Integrated Circuits.* John Wiley & Sons, New York, third edition, 1995.

[36] I. Lyubomirsky and Q. Hu. "Energy level schemes for far-infrared quantum well lasers". *Appl. Phys. Lett.*, 73:300–302, 1998.

[37] I. Lyubomirsky, Q. Hu, and M. R. Melloch. "Measurement of far-infrared intersubband spontaneous emission from optically pumped quantum wells". *Appl. Phys. Lett.*, 73:3043–3045, 1998.

[38] J. M. Ziman. *Theory of Solids.* Cambridge University Press, Cambridge, second edition, 1972.

[39] M. McLennan and S. Datta. *SEQUAL Users Manual.* Purdue University, Layfayette, 1989.

[40] D. F. Nelson, R. C. Miller, and D. A. Kleinman. Band nonparabolicity effects in semiconductor quantum wells. *Phys. Rev. B*, 35:7770, 1987.

[41] B. S. Williams. *GaAs/AlGaAs Mid-Infrared Quantum Cascade Lasers.* MS Thesis, Massachusetts Institute of Technology, Department of Electrical Engineering and Computer Science, 1998.

[42] C. Sirtori, F. Capasso, J. Faist, L. N. Pfeiffer, and K. W. West. "Far-infrared generation by doubly resonant difference frequency mixing in a coupled quantum well two-dimentional electron gas system". *Appl. Phys. Lett.*, 65:445–447, 1994.

[43] R. Loudon. *The Quantum Theory of Light.* Oxford University Press, Oxford, second edition, 1983.

[44] H. C. Liu, M. Buchanan, and Z. R. Wasilewski. "How good is polarization selection rule for intersubband transitions?". *Appl. Phys. Lett.*, 72:1682–1684, 1998.

[45] J. J. Sakurai. *Modern Quantum Mechanics.* Addison-Wesley, New York, revised edition, 1994.

[46] A. Yariv. *Quantum Electronics.* John Wiley & Sons, New York, third edition, 1989.

[47] A. E. Siegman. *Lasers.* University Science Books, Mill Valley, California, first edition, 1986.

[48] B. Gelmont, V. Gorfinkel, and S. Luryi. "Theory of the spectral line shape and gain in quantum wells with intersubband transitions". *Appl. Phys. Lett.*, 68:2171–2173, 1996.

[49] I. Lyubomirsky. *Quantum Reality and Squeezed States of Light.* MS Thesis, Massachusetts Institute of Technology, Department of Electrical Engineering and Computer Science, 1994.

[50] S. D. Brorson, H. Yokoyama, and E. P. Ippen. "Spontaneous emission rate alteration in optical waveguide structures". *IEEE J. Quan. Electron.*, 26:1492–1499, 1990.

[51] Q. Hu and S. Feng. "Feasibility of far-infrared lasers using multiple semiconductor quantum wells". *Appl. Phys. Lett.*, 59:2923–2925, 1991.

[52] J. H. Smet, C. G. Fonstad, and Q. Hu. "Intrawell and interwell intersubband transitions in multiple quantum wells for far-infrared sources". *J. Appl. Phys.*, 79:2272–2275, 1996.

[53] J. W. Bales, K. A. McIntosh, T. C. L. G. Sollner, W. D. Goodhue, and E. R. Brown. "Observation of optically pumped intersubband emission from quantum wells". *SPIE Quantum-Well and Superlattice Physics III*, 1283:74–81, 1990.

[54] J. Faist. Private communication.

[55] V. Berger. "Three-level laser based on intersubband transitions in asymmetric quantum wells: a theoretical study". *Semicond. Sci. Technol.*, 9:1493–1499, 1994.

[56] P. Harrison and R. W. Kelsall. "Population inversion in optically pumped asymmetric quantum well terahertz lasers". *J. Appl. Phys.*, 81:7135–7140, 1997.

[57] O. Gauthier-Lafaye, P. Boucaud, F. H. Julien, S. Sauvage, S. Cabaret, J. M. Lourtioz, , V. Thierry-Mieg, and R. Planel. "Long-wavelength ($\approx$ 15.5 μm) unipolar semiconductor laser in GaAs quantum wells". *Appl. Phys. Lett.*, 71:3619–3621, 1997.

[58] A. Seilmeier, H.-J. Hübner, G. Abstreiter, G. Weimann, and W. Schlapp. "Intersubband relaxation in GaAs-AlGaAs quantum well structures observed directly by an infrared bleaching technique. *Phys. Rev. Lett.*, 59:1345–1348, 1987.

[59] J. Faist, C. Sirtori, F. Capasso, L. Pfeiffer, and K. West. "Phonon limited intersubband lifetimes and linewidths in a two-dimensional electron gas". *Appl. Phys. Lett.*, 64:872–874, 1994.

[60] D. Y. Oberli, D. R. Wake, M. V. Klein, J. Klem, T. Henderson, and H. Morkoc. "Time-resolved Raman scattering in GaAs quantum wells". *Phys. Rev. Lett.*, 59:696–699, 1987.

[61] H. Spector. "Free-carrier absorption in quasi-dimentional semiconductor structures". *Phys. Rev. B*, 28:971–976, 1983.

[62] G. Sun and B. Khurgin. "Optically pumped 4-level infrared laser based on intersubband transitions in multiple quantum wells-feasibility study". *IEEE J. Quan. Electron.*, 29:1104–1111, 1993.

[63] W. J. Li and B. D. McCombe. "Coupling efficiency of metallic gratings for excitation of intersubband transitions in quantum-well structures". *J. Appl. Phys.*, 71:1038–1040, 1992.

[64] J. A. Levenson, G. Dolique, J. L. Oudar, and I. Abram. "Intersubband carrier relaxation in highly excited GaAs/$Ga_{1-x}Al_xAs$ multiple quantum wells". *Phys. Rev. B*, 41:3688–3694, 1990.

[65] S.-C. Lee, I. Galbraith, and C. R. Pidgeon. "Influence of electron temperature and carrier concentration on electron-LO-phonon intersubband scattering in wide GaAs/$Al_xGa_{1-x}As$ quantum wells". *Phys. Rev. B*, 52:1874–1881, 1995.

[66] T. Elsaesser, J. Shah, L. Rota, and P. Lugli. "Initial thermalization of photoexcited carriers in GaAs studied by femtosecond luminescence spectroscopy. *Phys. Rev. Lett.*, 66:1757–1760, 1991.

[67] M. Helm, P. England, E. Colas, F. DeRosa, and Jr. S. J. Allen. "Intersubband emission from semiconductor superlattices excited by sequential resonant tunneling". *Phys. Rev. Lett.*, 63:74–77, 1989.

[68] R. Hapanowicz. "FT-IR spectrometers profile optoelectronic emitters". *Laser Focus World*, pages 65–74, 1996.

[69] E. V. Loewenstein, D. R. Smith, and R. L. Morgan. "Optical constants of far infrared materials. 2: crystalline solids". *Appl. Opt.*, 12:398–405, 1973.

[70] K. L. Campman, H. Schmidt, A. Imamoglu, and A. C. Gossard. "Interface roughness and alloy-disorder scattering contributions to intersubband transition linewidths". *Appl. Phys. Lett.*, 69:2554–2556, 1996.

[71] K. Luo, H. Zheng, Z. Lu, J. Xu, Z. Xu, T. Zhang, C. Li, X. Yang, and J. Tian. "Subband separation energy depedence of intersubband relaxation time in wide quantum wells". *Appl. Phys. Lett.*, 47:490–492, 1985.

[72] C. Sirtori, J. Faist, F. Capasso, D. Sivco, A. L. Hutchingson, and A. Y. Cho. "Pulsed and continuous-wave operation of long wavelength infrared ($\lambda = 9.3$ μm) quantum cascade lasers". *IEEE J. Quan. Electron.*, 33:89–93, 1997.

[73] C. Sirtori, J. Faist, F. Capasso, D. Sivco, A. L. Hutchingson, and A. Y. Cho. "Long wavelength infrared ($\lambda \sim 11$ μm) quantum cascade lasers". *Appl. Phys. Lett.*, 69:2810–2812, 1996.

[74] S. M. Sze. *Physics of Semiconductor Devices.* John Wiley & Sons, New York, first edition, 1981.

[75] "Semiconductors: Group IV elements & III-V compounds". Data in Science and Technology. Springer-Verlag, Berlin, 1991.

[76] P. Boucaud, F. H. Julien, R. Prazeres, J. M. Ortega, I. Sagnes, and Y. Campidelli. "Intersubband relaxation time in the valence band of $si/si_{1-x}ge_x$ quantum wells". *Appl. Phys. Lett.*, 69:3069–3071, 1996.

[77] E. Rosencher and Ph. Bois. "Model system for optical nonlinearities: asymmetric quantum wells". *Phys. Rev. B*, 44:11315, 1991.